

Experimental Investigation and Analysis of a New Light-Based Hydrogen Production System

By

SAYANTAN GHOSH

A Thesis Submitted in Partial Fulfillment

of the Requirements for the Degree of Master of Applied Science

in

Mechanical Engineering

Faculty of Engineering and Applied Science

University of Ontario Institute of Technology

Oshawa, Ontario, Canada

© Sayantan Ghosh, December 2014

Abstract

Due to the world's increasing population and the rising standard of living, global energy demand is expected to keep increasing. The limited nature of fossil fuels and their non-homogenous global distribution along with the emissions related to their utilization have caused renewable energies to be considered as a key to sustainability. However, renewable energy sources such as solar energy are intermittent, due to which it has to be stored in an alternate form, such as electricity or hydrogen. Hydrogen is a highly versatile fuel that may become one of the key pillars to support the future energy infrastructure.

The photoelectrochemical water splitting cycle is one of the supreme attractive alternative photoelectrochemical cycles for clean hydrogen production due to its lower temperature requirement and better overall efficiency. The key objective of this master's research is to develop, theoretically analyse and experimentally investigate a continuous type hybrid hydrogen production system that photoelectrochemically splits water and electrolyses chloralkali to convert the by-products of H₂ production into useful industrial commodities. This hybrid system maximizes the utilized solar spectrum by combining photochemical and electrochemical hydrogen production in a photoelectrochemical system. In addition, CFD simulations are performed for various models to determine optimum design parameters for the present PEC reactor. Furthermore, by using electrodes as electron donors to drive photochemical hydrogen production, the hybrid system minimises the potential pollutants.

The proposed system has the advantage to eliminate generating waste by converting the by-products into commercially viable products. In addition to hydrogen, the system generates Cl₂ and NaOH which are desired by various industries. The proposed system has an annual production capacity of 2.8 kg hydrogen per square meter of heliostat with a production cost of 1\$/kg hydrogen produced. In addition to converting by-products into usable commodities, the system does not emit GHG during operation.

Acknowledgements

It would not have been possible to write this thesis without the help and support of the kind people around me, to only some of whom it is possible to give particular mention here. First of all, I would like to convey my warmest gratitude to my supervisor Professor Dr. Ibrahim Dincer, who has given me a unique opportunity to conduct my study in his research group, for his guidance, generous contribution of knowledge and experience, valuable comments and encouragement from the start until the end of my study.

Secondly, my warmest thanks go to Dr. Calin Zamfirescu for his help with the various obstacles and issues that I encountered during the project, particularly with the experimental setup and the thermodynamic analyses.

My colleagues at UOIT made an enjoyable working environment for me. I would like to acknowledge everyone in research room ACE3030B for their assistance in many aspects that I cannot list because of the limited space here. I would also like to express my very great appreciation to the people for their help and support during the preparation of this thesis, especially Canan Acar, Farrukh Khalid, Fahad Suleman, Janette Hogerwaard, and Camilo Casallas. I wish to thank all my colleagues and friends at for sharing with me numerous coffees, lunches, and laugh at all times.

Last but not least, I would like to express my eternal gratitude to my parents for their endless consistent support, patience, and encouragement throughout my life. Besides these, I would also like to express my great debt of gratitude to my family for believing in me. This thesis is dedicated to my mother and father. If there is any honor in this degree, it belongs to them.

Furthermore, the financial support provided the Natural Sciences and Engineering Research Council of Canada (NSERC) is gratefully acknowledged.

Table of Contents

Chapter 1: Introduction	1
1.1 Energy and Environment Challenges	1
1.2 Hydrogen as a Fuel	3
1.3 Solar Hydrogen Production	5
1.4 Motivation and Objectives	6
1.4.1 Motivation	7
1.4.2 Objectives	7
Chapter 2: Literature Review	9
2.1 Introduction	9
2.2 Hydrogen Production through Electrolysis	11
2.3 Hydrogen Production from Electrochemical Methods	12
2.4 Chloralkali Modelling	13
2.5 Heliostat Modelling	14
Chapter 3: Background	16
3.1 Water Splitting	16
3.2 Photocatalytic Water Splitting	17
3.3 Chloralkali Process	19
3.3.1 Membrane Cell Chloralkali Process	19
3.3.2 Thermodynamics of Electrochemical Reactions	21
3.3.3 Charge Transport in Aqueous Electrolytes	21
3.3.4 Charge Transport through Ion Exchange Membranes	23
3.3.5 Mass Transport of Reactants	24
Chapter 4: Experimental Apparatus and Methodology	25
4.1 System Description	25

4.2	Reactor Design	29
4.2.1	Modelling Approach	29
4.3	Electrical Contacts Installation.....	33
4.4	Membrane Installation.....	35
4.5	Instruments and Devices	38
4.5.1	Potentiostat.....	38
4.5.2	Peristaltic Pump	38
4.5.3	Hot Plates, Reservoirs, and Magnetic Bars.....	40
4.6	Large Scale Conceptual Design	40
Chapter 5: Analyses		44
5.1	Thermodynamic Concepts.....	45
5.1.1	Mass Balance Equation (MBE)	46
5.1.2	Energy Balance Equation (EBE)	46
5.1.3	Entropy Balance Equation (EnBE)	47
5.1.4	Exergy Balance Equation (ExBE)	47
5.2	Light Processing Subsystem.....	50
5.3	Volumetric Receiver	55
5.4	Desalination Subsystem	55
5.5	Photovoltaic Subsystem	57
5.6	Photoelectrochemical Subsystem.....	58
5.6.1	Mass Balance Equation.....	60
5.6.2	Energy Balance Equation.....	63
5.6.3	Voltage Balance Equation.....	63
5.6.4	Entropy Balance Equation	69
5.6.5	Exergy Balance Equation.....	69

5.6.6	Reynolds Number	70
5.6.7	Transport Equations	70
5.6.8	Meshing Details	71
5.7	Energy and Exergy Efficiencies.....	73
5.8	Optimisation Study.....	75
Chapter 6: Results and Discussion.....		78
6.1	System Efficiencies and Exergy Destructions	78
6.2	PEC Chloralkali Electrolysis.....	81
6.2.1	Case Study 1	82
6.2.2	Case Study 2	85
6.2.3	Case Study 3	87
6.2.4	Case Study 4	90
6.2.5	Case Study 5	93
6.2.6	Case Study 6	96
6.3	Electrolysis Model.....	98
6.4	Comparison of Model Results with Experimental Data.....	103
6.5	Scale-up Studies and Results.....	105
6.6	CFD Simulation Results.....	107
6.7	Cost Assessment Results	110
6.8	Optimisation Results	112
6.8.1	Maximisation of Energy Efficiency	112
6.8.2	Maximisation of Exergy Efficiency.....	115
Chapter 7: Conclusions and Recommendations		118
7.1	Conclusions	118
7.2	Recommendations	119

References.....	120
Appendix A: Detailed CAD Drawings	127

List of Figures

Figure 1.1: (a) Total primary energy supply of the world (13113 MToe); (b) Total world electricity generated by fuel (22126 TWh); (c) World total consumption by fuel (8918 MToe); (d) World total CO ₂ emissions by fuel (31342 Mt of CO ₂) (Data from IEA, 2014).	2
Figure 2.1: Schematic diagram of solar photoelectrolysis (Joshi et al., 2010).	11
Figure 3.1: Selected hydrogen production methods along with their primary energy source (Adapted from Acar and Dincer, 2014).	16
Figure 3.2: Conceptual design of the photochemical water splitting reactor (Adapted from Zamfirescu et al., 2011).	18
Figure 3.3: Schematic representation of the chloralkali membrane cell process (Adapted from Dias, 2005).	20
Figure 3.4: Illustration of the Donnan exclusion effect (Adapted from Mulder, 1996).	23
Figure 4.1: Process flow diagram of the novel photoelectrochemical hydrogen production system.	26
Figure 4.2: Overall PEC system setup.	27
Figure 4.3: Cathode and anode sides of the reactor during operation.	27
Figure 4.4: PEC system exposed to solar simulator.	28
Figure 4.5: Anode side oxidation due to damage in stainless steel washers.....	28
Figure 4.6: (Left) initial design (1 inlet 1 outlet), (right) modified design (2 inlets, 2 outlets).....	30
Figure 4.7: Cross section view to model the liquid flow over the membrane.	31
Figure 4.8: (a) Front/top view after rapid prototyping, (b) back view after rapid prototyping.....	31
Figure 4.9: Extended view of photoelectrochemical reactor.	32
Figure 4.10: Reactor assembly model sketched in SolidWorks.	32

Figure 4.11: Anode bending process (a) mounting on bench vice, (b) adjusting height, (c) bending using hammer, (d) after installation in the reactor using gaskets.....	34
Figure 4.12: (a) Cathode contact, (b) back contact, (c) side contact, (d) back view of the reactor after contacts installation.	35
Figure 4.13: (a) Glove box, (b) inside the glove box before installation, (c) punching holes through the membrane using puncher, (d) applying silicon paste.....	36
Figure 4.14: (a) Teflon covering the screws, (b) silicon glue applied to gaskets, (c) after installation of MPEA in an inert environment (glove box).	37
Figure 4.15: (a) Reference 3000 high performance potentiostat, (b) reference 30k booster.	38
Figure 4.16: (a) Multichannel BT100-2J Peristaltic pump, (b) pump during system operation.	39
Figure 4.17: Peristaltic pump software for external control of flow rates.....	39
Figure 4.18: (a) Electrolyte feed/dump tank, (b) magnetic stirrer bar, (c) hot plate/electric heater.....	40
Figure 4.19: Conceptual block diagram of the integrated system for solar hydrogen production.	41
Figure 4.20: Experimental procedure overview.....	42
Figure 5.1: Process flow schematic for the desalination subsystem.....	56
Figure 5.2: Schematic of the light-based hybrid photoelectrochemical reactor.	60
Figure 5.3: Case 1 and 2 mesh using ICEM CFD.....	72
Figure 5.4: Case 3 mesh using ICEM CFD.	73
Figure 5.5: Multi-objective optimisation of systems (Dincer and Zamfirescu, 2014).....	76
Figure 5.6: Genetic algorithm optimisation technique flowchart (Adapted from Tarique, 2011).	77
Figure 6.1: Spectral irradiance within the light processing subsystem.....	78
Figure 6.2: Exergy destructions within light processing subsystems.	80

Figure 6.3: Exergy destruction per kg of brine input for the desalination subsystem.	81
Figure 6.4: Effect of operating temperature on hydrogen production rate and required work input.	82
Figure 6.5: Effect of operating temperature on input current and voltage.....	83
Figure 6.6: Effect of operating temperature on energy and exergy efficiencies.....	83
Figure 6.7: Effect of operating temperature on production yield for chlorine and hydrogen gases.....	84
Figure 6.8: Effect of operating temperature on exergy destruction rate and NaOH exit concentration.....	84
Figure 6.9: Effect of ambient temperature on energy and exergy efficiencies.	85
Figure 6.10: Effect of ambient temperature on production yield for hydrogen and chlorine gases.....	86
Figure 6.11: Effect of ambient temperature on work input and exergy destruction rates.	86
Figure 6.12: Effect of operating and ambient temperatures on hydrogen production and work input.	87
Figure 6.13: Effect of operating and ambient temperatures on input current and voltage.	88
Figure 6.14: Effect of operating and ambient temperatures on energy and exergy efficiencies.....	88
Figure 6.15: Effect of operating and ambient temperatures on production yield for chlorine and hydrogen gases.....	89
Figure 6.16: Effect of inlet brine mass flow rate on energy and exergy efficiencies.	90
Figure 6.17: Effect of inlet brine mass flow rate on hydrogen production rate and work input.	91
Figure 6.18: Effect of inlet brine mass flow rate on input current and voltage.	91
Figure 6.19: Effect of inlet brine mass flow rate on production yield for chlorine and hydrogen gases.....	92

Figure 6.20: Effect of inlet brine mass flow rate on exergy destruction rate and NaOH exit concentration.....	92
Figure 6.21: Effect of output brine concentration on energy and exergy efficiencies.....	93
Figure 6.22: Effect of output brine concentration on hydrogen production rate and work input.	94
Figure 6.23: Effect of output brine concentration on input current and voltage.....	94
Figure 6.24: Effect of output brine concentration on production yield for chlorine and hydrogen gases.....	95
Figure 6.25: Effect of output brine concentration on exergy destruction rate and NaOH exit concentration.....	95
Figure 6.26: Effect of electrode membrane distance on energy and exergy efficiencies.	96
Figure 6.27: Effect of electrode membrane distance on hydrogen production rate and work input.	97
Figure 6.28: Effect of electrode distance on input current and voltage.....	97
Figure 6.29: Effect of electrode membrane distance on production yield for chlorine and hydrogen gases.....	98
Figure 6.30: Effect of electrode membrane distance on exergy destruction rate and NaOH exit concentration.....	98
Figure 6.31: Effect of reaction temperature on energy and exergy efficiencies of water electrolyser.....	99
Figure 6.32: Effect of reaction temperature on activation and ohmic potentials.....	99
Figure 6.33: Effect on reaction temperature on cell voltage and current density.	100
Figure 6.34: Effect of ambient temperature on energy and exergy efficiencies.	100
Figure 6.35: Effect of reaction temperature on input work and exergy destruction rates.	101
Figure 6.36: Effect of cell current on production yield rate of oxygen and hydrogen gases in water electrolysis.	101

Figure 6.37: Effect of input current on input work rate and exergy destruction for the electrolyser.....	102
Figure 6.38: Effect of input current on energy and exergy efficiencies for the electrolyser. .	102
Figure 6.39: Comparison of hydrogen gas production rate.	103
Figure 6.40: Comparison of IV curve for water electrolysis.	104
Figure 6.41: Exergy destructions of the integrated system in solar hydrogen production system.	105
Figure 6.42: Energy and exergy efficiencies of all subsystems in solar hydrogen production system.	106
Figure 6.43: Exergy destruction ratios for all subsystems.....	106
Figure 6.44: Velocity vectors coloured by velocity magnitude (m/s).	108
Figure 6.45: Velocity contours for (a) 10 g/s, (b) 25 g/s, (c) 50 g/s, (d) 100 g/s inlet mass flow rate	109
Figure 6.46: (a) One inlet and one outlet laminar flow, (b) one inlet and one outlet turbulent flow.....	109
Figure 6.47: Capital productivity factor in function of the specific invested capital ($\$/\text{m}^2$ of heliostat field).....	111
Figure 6.48: Maximisation of energy efficiency: genetic algorithm optimisation method (16692 iterations).....	113
Figure 6.49: Maximisation of exergy efficiency: genetic algorithm optimisation method (4212 iterations).....	115
Figure 6.50: Pareto frontiers of two-objective optimisation for the PEC system when cost minimisation for building the reactor and revenue generated form the outputs are functions to be maximised.	117

List of Tables

Table 1.1: Global hydrogen consumption categories (Data extracted from Abbasi and Abbasi, 2011).....	4
Table 1.2: An overview of solar hydrogen production methods (Adapted from Joshi et al., 2011).	6
Table 3.1: Equilibrium electrode potentials for the half electrochemical reactions in a typical chloralkali membrane cell process (Data taken from Schmittinger, 2008).....	21
Table 3.2: Transport processes for charge transport in electrolytes (Adapted from O'Hayre et al., 2006).	22
Table 4.1: Properties of reactor core components.	33
Table 5.1: Meshing details.....	72
Table 6.1: Energy, exergy, entropy, and temperature within light processing subsystem.	79
Table 6.2: Salinity, specific exergy, enthalpy, and entropy of the desalination subsystem.....	80
Table 6.3: Mass flow rate, molar and mass concentrations, specific enthalpy, entropy, and chemical and physical exergies of the PEC system.	81
Table 6.4: Energy and exergy efficiencies of all subsystems in solar hydrogen production system.	105
Table 6.5: Energy losses and exergy destruction values for all subsystems in solar hydrogen production system.	106
Table 6.6: Cost analysis equations.....	111
Table 6.7: Assumed parameters for cost calculations.....	112
Table 6.8: Best values for the independent variables selected for genetic algorithm optimisation ($\eta_{en} = 11.96\%$).	113
Table 6.9: State point parameters for maximum energy efficiency.....	114
Table 6.10: Performance parameters of the energy efficiency optimised system.	114

Table 6.11: Best values for the independent variables selected for genetic algorithm optimisation ($\eta_{ex} = 49.01\%$).116

Table 6.12: State point parameters for maximum exergy efficiency.....116

Table 6.13: Performance parameters of the exergy efficiency optimised system.116

Nomenclature

A	Area (m^2)
c	Photonic constant (mK); speed of light (3×10^8 m/s); concentration (kg/m^3)
d	Distance (m)
D	Diffusivity (m^2/s)
e	Charge of an electron ($1.60217657 \times 10^{-19}$ C)
\dot{E}	Energy rate (W, kW)
E°	Open circuit voltage (V)
eV	Electron Volt
ex	Specific exergy (J/g or kJ/kg)
$\dot{E}x$	Exergy rate (W or kW)
F	Field loss factor; Faraday's constant (96480 C/mol)
F_{field}	Field factor
h	Specific enthalpy (J/g or kJ/kg)
\hbar	Planck's constant ($6.62606957 \times 10^{-34}$ m ² kg/s)
i	Inflation rate
I	Irradiance (W/m^2)
J	Current density (A/m^2)
k	Boltzmann constant ($1.3806488 \times 10^{-23}$ J/K); refraction index
l	Length (m)
\dot{m}	Mass flow rate (g/s or kg/s)
M	Molar concentration (mol solute/L solution)
\dot{n}	Molar flow rate (mol/s)
N_A	Avogadro's Number (6.0221413×10^{23} mol ⁻¹)
P	Pressure (kPa)
\dot{Q}	Heat transfer rate (W or kW)
r	Discount rate (% on product cost)
R	Reflectance; gas constant (8.314 kJ/kmol)
R_s	Internal resistance of PV cell (Ω/m^2)
s	Specific entropy (J/gK or kJ/kgK)

\dot{S}	Entropy rate (W/K or kW/K)
t	Tax (% on revenue)
T	Temperature (°C or K)
V	Voltage (V)
w	Salinity (g salt/kg solution)
\dot{W}	Work rate (W)
x	Salt concentration used in EES calculations (kg salt/kg solution)

Greek Symbols

γ	Intercept factor; optical aberration; activity coefficient
Δ	Change
η	Efficiency
θ	Incident angle
λ	Wavelength; metal extinction coefficient
μ	Chemical potential
ν	Dimensionless voltage
ρ	Density (kg/m ³)
Φ	Spectral quantum efficiency

Subscripts and Superscripts

a	Interception
act	Actual
aq	Aqueous
at	Atmospheric attenuation
b	Blocking
c	Credit due to promotion of renewable energy; convection
ch	Chemical
con	Consumption
conc	Concentration unit
cv	Control volume
d	Diffusion
dest	Destruction

des	Desalination unit
dni	Direct normal irradiance
en	Energy
ex	Exergy
f	Flow; field
fs	Filter splitter
g	Glass; gas
gen	Generation
h	Heliostat
hm	Spectral splitter
i	Income
in	Inlet stream
ke	Kinetic energy
l	Losses; liquid
m	Market; conduction
max	Maximum
min	Minimum
mix	Mixture
oc	Open circuit
out	Outlet stream
p	Property
pe	Potential energy
ph	Photonic current; physical
r	Real
rad	Radiation
rec	Receiver
s	Salvage; shading of surfaces; salt (NaCl or NaOH)
sc	Short circuit
sol	Solution
w	Work
°	Standard state

0 Reference state

Acronyms

ABS	Acrylonitrile Butadiene Styrene
CERL	Clean Energy Research Laboratory
CFD	Computational Fluid Dynamics
CPF	Capital Productivity Factor
CRF	Capital Recovery Factor
EBE	Energy Balance Equation
EDE	Electrode Diaphragm Electrode
EIS	Electrochemical Impedance Spectroscopy
ExBE	Exergy Balance Equation
EES	Engineering Equation Solver
FF	Filling Factor
GC	Generated Capital
GHG	Greenhouse Gas
GWP	Global Warming Potential
HHV	Higher Heating Value
IC	Invested Capital
IEA	International Energy Agency
LHV	Lower Heating Value
LPC	Levelized Product Cost
MPEA	Membrane Photo Electrode Assembly
MToe	Million Ton of Oil Equivalent
NI	Net Income
OC	Open Circuit
OMCF	Operation and Maintenance Cost Factor
PC	Photocathode
PE	Photoelectrode
PEC	Photoelectrochemical Cells
PEM	Proton Exchange Membrane

PFSA	Perfluorosulfonic Acid
PTFE	Polytetrafluoroethylene
PV	Photovoltaic
PVF	Present Value Factor
PWF	Present Worth Factor
PWI	Present Worth Income
SC	Short Circuit
SCR	Steam-to-Carbon Ratio
SI	Sustainability Index
SIC	Specific Invested Capital
SMR	Steam Methane Reforming
SOFC	Solid Oxide Fuel Cell
SV	Salvage Value
TCD	Tax Credit Deduction
TI	Taxable Income
TOI	Tax on Income
TOP	Tax on Property
TPES	Total Primary Energy Supply
UOIT	University of Ontario Institute of Technology
ZRA	Zero Resistance Ammeter

Chapter 1: Introduction

1.1 Energy and Environment Challenges

The world around us has changed ominously over the past two decades. Technology has become one of the main drivers of economic and social development. The swift advancement of Information Technology (IT) all over the world has transformed not only the way we think, but also the way we act. All aspects of human life have been affected by IT and the Internet, in particular. Needless to say that practically all technologies run on electricity and therefore the share of electricity is increasing rapidly, faster than Total Primary Energy Supply (TPES) (WEC, 2013).

Population growth has always been and will remain one of the key drivers of energy demand, along with economic and social development. While global population has increased by over 1.5 billion over the past two decades, the overall rate of population growth has been slowing down. The number of people without access to commercial energy has reduced slightly, and the latest estimate from the World Bank indicates that it is 1.2 billion people (WEC, 2013). Keeping up with this mounting global energy demand due to the increasing population and rising standards of living is one of the principal challenges of the twenty-first century.

Figure 1a demonstrates the world's fuel shares of total primary energy supply (TPES) and Figure 1b shows the electricity generated by fuel. From this figure it is clear that more than 80% of the world's energy supply is met by fossil fuels.

The increase in the average temperatures over the globe since the mid-20th century is mainly related to the recorded increase in the greenhouse gas concentration. Carbon dioxide (CO₂), water vapor and methane known as greenhouse gases absorb solar radiation and create a natural greenhouse cover effect around the earth. It is predicted that the earth average temperatures could be 30°C lower without this effect (Goldemberg, 2006). The main pollutants due to combustion of fossil fuels are the carbon dioxide (CO₂), carbon monoxide (CO), sulphur dioxide (SO_x), nitrogen oxides (NO_x), ozone (O₃), lead (Pb), soot and ash. These negative effects extend from humans to water resources, farm produce, plants, forests, animals and other components of human habitat like buildings (e.g. degradation of buildings envelope due to

pollution), damaging of coasts and beaches (e.g. through oil spills), effects on climate (e.g. processes associated with temperature rise, ice melting and ocean waters rise) (Dincer, 2012). Figure 1d shows the total global CO₂ emissions which signifies that utilization of fossil fuels is the cause of 99% of the world's CO₂ emissions. Hence, it is needless to say that switching to a non-fossil fuel energy source would greatly reduce the CO₂ emissions and their adverse-effect of global warming.

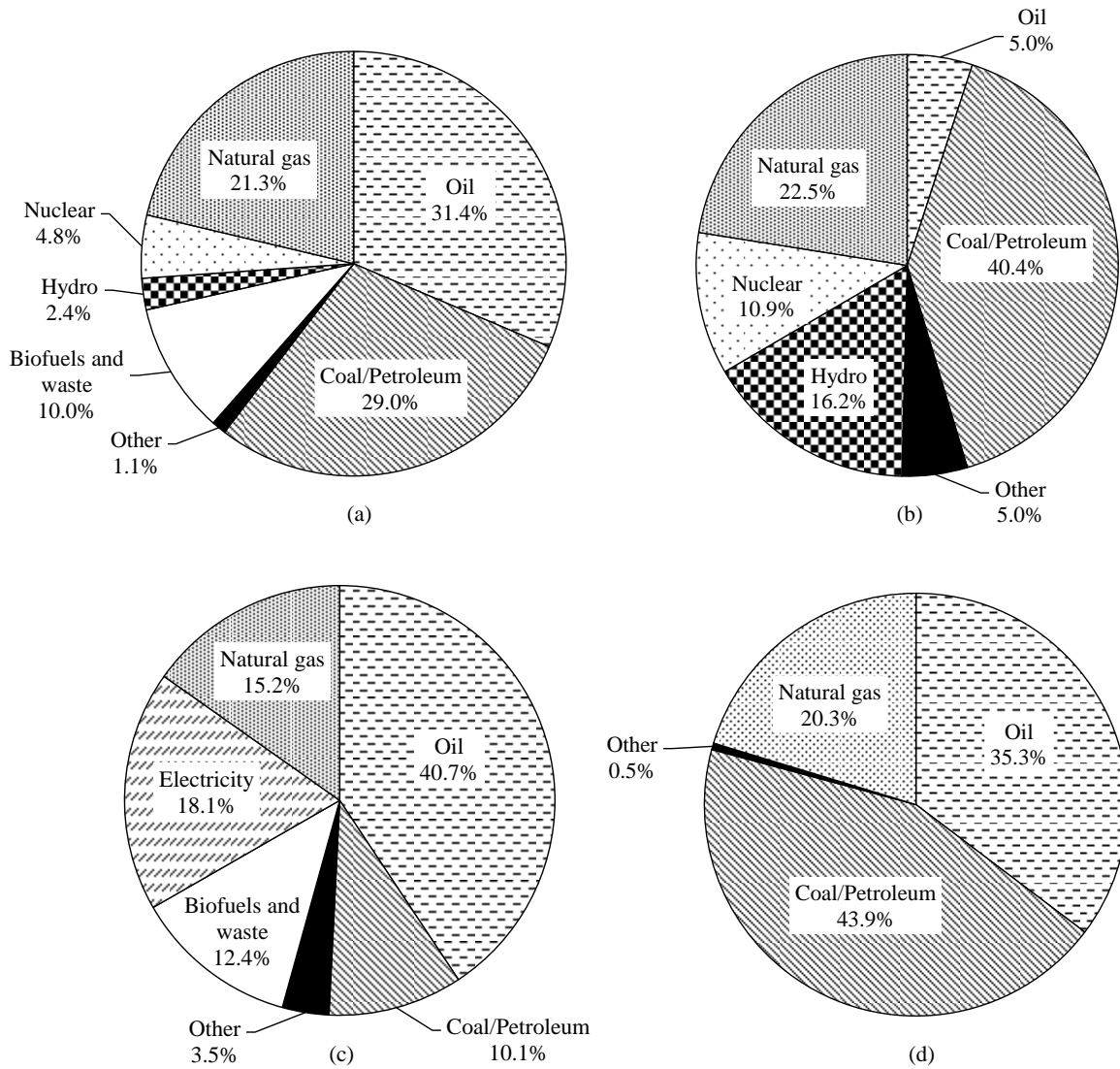


Figure 1.1: (a) Total primary energy supply of the world (13113 MToe); (b) Total world electricity generated by fuel (22126 TWh); (c) World total consumption by fuel (8918 MToe); (d) World total CO₂ emissions by fuel (31342 Mt of CO₂) (Data from IEA, 2014).

The world's energy system is at least a 1.5 trillion dollars market dominated by fossil fuels, where small changes can have a large influence on efforts to reach sustainability. Renewable energy sources are key to achieving this goal (Goldemberg, 2006).

1.2 Hydrogen as a Fuel

Hydrogen presently represents a market of approximately fifty billion US\$ for 40 Mt annual production, and is predominantly used as a chemical substance rather than a fuel. The most of its existing uses are found as processing agent in oil refineries (e.g. for desulphurization and upgrading conventional petroleum) and in chemicals production processes (e.g. methanol, ammonia and pharmaceuticals). Projections of future population increase with the consequence of an augmented obligation of food and of various commodities lead to the logical conclusion that the demand of hydrogen will increase too, at least to satisfy the requirements of conventional transportation fuels, fertilizers and chemicals (Dincer, 2012).

A consequence of the increased energy and food demand is the raise of greenhouse gases (GHG) emissions in the atmosphere. Measures to limit GHG emissions must consider hydrogen production from sustainable energy sources i.e. so-called green hydrogen production methods. As much as 450 billion m³ of hydrogen is currently produced and consumed in the world mainly as raw material for various other chemicals (Gupta, 2008; Sobrino et al., 2010). Furthermore, almost all of this hydrogen is produced by processes which use fossil fuels, hence by 'unclean' approach. Approximately 2.5 tonnes of carbon is released as CO₂ for each tonne of hydrogen produced from hydrocarbons. On the other hand, approximately 5 tonnes of carbon is emitted per tonne of hydrogen to the atmosphere when produced from coal (Gupta, 2008; Scott, 2008). Table 1.1 represents the current hydrogen production scenario in the world.

Presently, hydrogen is mainly produced by steam reforming of natural gases: a process which led to massive emissions of GHG. Close to 50% of the global demand for hydrogen is currently generated via steam reforming of natural gas, about 30% from oil/ naphtha reforming from refinery/chemical industrial off- gases, 18% from coal gasification, 3.9% from water electrolysis and 0.1% from other sources (Muradov and Veziroğlu, 2005).

Table 1.1: Global hydrogen consumption categories (Data extracted from Abbasi and Abbasi, 2011).

Category	Hydrogen consumed	
	Billion m ³	Share (%)
Ammonia producers	273.7	61
Oil refineries	105.4	23
Methanol producers	40.5	9
Others	13.6	3
Merchant users	16.1	4
Total	449.3	100

Unfortunately, at the present level of advancement in different technologies for hydrogen production, the one based on water consumes the maximum energy. It is for this reason only a minor fraction of total hydrogen production in the world is based on water as a raw material presently (Kato, 2009). In the foreseen hydrogen economy of the future, green hydrogen production methods will be applied to supply hydrogen to be used directly as fuel, or to generate synthetic fuels, to produce ammonia and other fertilizers (viz. urea), to upgrade heavy oils (like oil sands), and to produce other chemicals (Levin and Chahine, 2010). Even from early time of hydrogen energy concept development, Awad and Veziroğlu (1984) pointed out the importance of hydrogen in removing environmental damages generated by combustion of fossil fuels. Hydrogen is considered as an ideal energy carrier because of the following reasons:

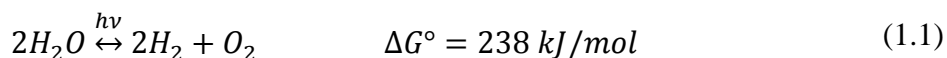
- It has high energy conversion efficiencies.
- It can be produced from water with no emissions.
- It is abundant.
- It can be stored in different forms (e.g. gaseous, liquid, or in together with metal hydrides).
- It can be transported over long distances more efficiently than electricity.
- It can be converted into other forms of energy in more ways than any other fuel.
- It has higher HHV and LHV than most of the conventional fossil fuels.
- If produced from renewable energies and water, its production, storage, transportation and end use do not harm the environment.

1.3 Solar Hydrogen Production

Solar irradiation is the most abundant source of energy on earth. The majority of physical and chemical reactions encountered on earth, including photosynthesis and water and air circulation in the atmosphere, are a direct or indirect result of solar radiation. Fossil fuels (oil, coal, natural gas, etc.) were originally produced by photosynthesis and solar heating. Hence, it is needless to say that all forms of energy (including renewables) are direct/indirect form of solar energy. Solar radiation, although fluctuating over short periods of time, is a constant source of energy over long-term periods. Moreover, unlike conventional power generation stations, gradual expansion of solar power generating systems is relatively inexpensive (Dincer, 2002).

Due to the irregular nature of solar energy, day/night cycles and cloudy days strongly affect the amount of solar energy that reaches the earth's surface. Hence, solar energy needs to be stored in a different form in order to provide continuous supply. As a chemical fuel, hydrogen seems to be a promising storage medium due to its high energy storage capacity and ease of transport (Zamfirescu et al., 2013).

The necessity for a solar energy storage medium and the role of hydrogen to address this concern is discussed to this point. Water splitting is a promising pathway for solar to hydrogen energy transformation since water is plentiful and effortlessly accessible source of hydrogen. A visible light photon has a minimum and maximum energy of 1 eV and 3 eV (or 100 kJ/mol and 300 kJ/mol) respectively, which is sufficient enough to produce hydrogen via water splitting (Van de Krol and Grätzel, 2011). Table 1.2 briefly presents some of the existing pathways for solar hydrogen production systems. The solar water splitting reaction can be written as follows:



In this thesis study, the main focus is placed on electrolysis, photoelectrolysis, photocatalysis, and photoelectrochemical water splitting hydrogen production. The prime reasons for selecting these techniques amongst the ones listed in Table 1.2 are to avoid safety concerns, reduce system energy requirements, and improve system control by choosing low temperature operations instead of the high temperature procedures. Moreover, by avoiding high temperature requirements, the need of large scale solar concentrators can be disregarded.

Besides, by operating the system in ambient conditions, the proposed system can work well in small scales and in geographically isolated areas. Also, by using chloralkali process coupled with the selected solar hydrogen production methods, it is aimed to convert by-products into commercially viable commodities, and as a result, improve system efficiency. The proposed system is developed in a way that product gases are collected without the need of post-separation.

Table 1.2: An overview of solar hydrogen production methods (Adapted from Joshi et al., 2011).

Solar H₂ Production Systems	Type	Processes	Process Description	End Products
PV	Low temperature	Electrolysis	Water electrolysis	H ₂ , O ₂
Photocatalytic		Photocatalysis	Water photocatalysis	H ₂ , O ₂
Photoelectrochemical		Photoelectrolysis	Water photoelectrolysis	H ₂ , O ₂
Photobiological		Photobiolysis	Plant and algal photosynthesis	H ₂
Concentrated solar thermal	High temperature	Thermolysis	Thermal dissociation of water	H ₂ , O ₂
		Thermochemical cycles	Thermochemical cycles using metal oxides	H ₂ , O ₂
		Gasification	Steam-gasification of coal and other solid carbonaceous materials	H ₂ , CO ₂
		Cracking	Thermal decomposition of natural gas (NG), oil, and other hydrocarbons	H ₂ , C
		Steam reforming	Steam reforming of NG, oil and other hydrocarbons	H ₂ , CO ₂
		Electrolysis	Water electrolysis via high temperature and solar thermal electricity generation	H ₂ , O ₂

1.4 Motivation and Objectives

In this section, the motives behind this study and the objectives met during the course of the research are discussed.

1.4.1 Motivation

Solar energy is the only renewable source with sufficient abundance to replace most or all of the current fossil energy use. Conversely, current photovoltaic and solar thermal technologies cannot be scaled considerably because of the chronological and geographical intermittency of sunlight. Hence, effectual and low-cost methods for storing solar energy in a condensed medium are desirable in order to significantly increase the utilization of sun as a principal source. Regardless of their gigantic prospective benefits, the feasibility of photoelectrical, photochemical, and photocatalytic hydrogen production systems at different scales are yet to be explored. The absence of adequate solar hydrogen production systems which are environmentally benevolent, profitable, efficient, and safe is one of the focal problems for the evolution of a solar energy based hydrogen economy.

The fundamental motivation of this work is the potential for combining the photo-techniques in a hybrid reactor to increase the solar spectrum exploitation and hydrogen production revenue as well as transfiguring the by-products into commercially valued commodities. For this determination, a system consisting of semiconductors, electro-catalysts, and ion selective membranes to carry out photoelectrochemical process combined with a chloralkali electrolysis process is developed as a method for solar hydrogen generation.

1.4.2 Objectives

The overall objective of this thesis study is to develop and thermodynamically access a new light-based hydrogen production system. In this regard, the specific objectives of this thesis are given as follows:

1. To develop a continuous type light-based photoelectrochemical hydrogen production system and determine the design aspects for the system.
2. To design all reactor core parts i.e. cell, electrical contacts, gaskets, glassing etc.
3. To conduct CFD analysis to find ideal design parameters based on flow patterns.
4. To use a polymeric membrane electrode assembly as photoelectrode (photocathode, photoanode or both).

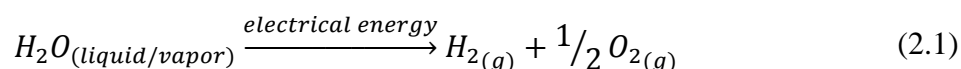
5. To conduct various experimental studies on each process type based on different parameters and ambient conditions to investigate the effect of key variables on product yields and system performance.
6. To theoretically integrate system with desalination to utilise ocean water as saturated brine input to the photoelectrochemical hydrogen production system.
7. To perform calculations for original optics with light concentration and spectral splitting and integration with PV array.
8. To perform comprehensive energy and exergy analyses for electrolysis, photoelectrolysis, and photoelectrochemical experiments.
 - a. To define the properties of system input and products.
 - b. To write mass, energy, entropy and exergy balance equations for all components and use EES software to solve the equations.
 - c. To achieve electrochemical modelling and explore the associations between production yields and applied voltage, incident solar irradiation, and/or any potential voltage drops.
 - d. To compare the results of the balance equations and electrochemical model calculations with experimental outputs, and highlight any inconsistencies and their significance.
 - e. To calculate the energy and exergy efficiencies of the PEC system and the overall large scale conceptual design, conduct parametric studies by altering key parameters affecting the system within an acceptable range, and perform exergy analysis to investigate the potential challenges on the system.
 - f. To determine the entropy generation and irreversibilities with their magnitudes and identify the effects of different parameters on them.
9. To perform optimisation using Genetic algorithm method in EES and maximise energy and exergy efficiencies.

Chapter 2: Literature Review

2.1 Introduction

The sun (because of the sheer magnitude of radiation received on the surface of the earth) and water are considered as limitless sources which makes this methodology eye-catching in the process of hydrogen production. Hence, various studies have argued the prospective benefits of these sources as a sustainable development (Dincer, 2007; Gibson and Kelly, 2010).

As mentioned by Kreuter and Hofmann (1998), electrolysis has been studied extensively in the literature since the beginning of the 1800s as a simple and effective method of splitting water into hydrogen and oxygen. Electrolysers producing hydrogen in both batch and large scales currently meet about 4% of the global hydrogen demand (Ewan and Allen, 2005). The net electrolysis reaction can be written as



There has been a constant effort to reduce the energy requirements of the electrolysis reaction (Connolly, 2012). Van de Krol and Grätzel (2011) described the existing pathways for the conversion of water and sunlight into hydrogen as follows:

- Photoelectrochemical water splitting
- Photocatalytic water splitting
- Coupled photovoltaic – electrolysis systems
- Thermochemical conversion
- Photobiological methods
- Molecular artificial photosynthesis
- Plasma-chemical conversion
- Mechano-catalytic, magnetolysis, radiolysis, etc.

Van de Krol and Grätzel (2011) exclusively focused their study on the first method in the list i.e. photoelectrochemical water splitting with semiconductor photoelectrodes. One of the main reasons/advantages why this approach is appealing is that hydrogen and oxygen are formed at separate electrodes. This not only circumvents safety concerns, but also allows effortless

separation of gases without having to pay a substantial energy penalty for post separation. The second advantage is that this method can be carried out in room temperature which means that there is no need for large scale solar concentrators that would limit its application to large central facilities in sunny regions of the world. The third advantage is that a photoelectrochemical water splitting equipment can be built exclusively from inorganic ingredients. This offers a degree of chemical robustness and durability that is difficult to achieve for organic or biological systems (Van de Krol and Grätzel, 2011).

As stated by Bolton (1978), a lot of attention from the scientific community was received by introduction of solar electricity via PV panels, and the possibility of its electrochemical, photolysis and photoelectrochemical electrolysis applications. Conversely, using photocatalysis is another promising option for 'clean' solar hydrogen production, being potentially applicable for small and large scale hydrogen generators (Kudo, 2007). According to Zamfirescu et al. (2013) and Lewis and Nocera (2006), there is a huge market potential for photocatalysis for many reasons: (i) reasonable solar to hydrogen efficiency; (ii) low process cost with reasonable but cheap catalysts selection; (iii) being able to separate H₂ and O₂ evolution during reaction; (iv) can be produced in mass numbers because of the small reactor systems that meet the requirements for residential applications.

Fujishima and Honda (1972) studied photoelectrochemical water splitting using TiO₂ as photocatalyst. Post this research, this approach was adapted by many researchers for clean and sustainable hydrogen production. Particle sizes of several hundred nanometers to a few micrometers of particulate photocatalytic systems were first validated in 1980 (Sato and White, 1980). MacDonnell (2008) extensively reviewed some past studies on photoreactions generating hydrogen. Various photoelectrochemical and photocatalytic systems for hydrogen production were also studied by Zamfirescu et al. (2008).

Photoelectrochemical (PEC) cells can be a cost effective way to produce hydrogen. Ni et al. (2007) and Nowotny et al. (2005) addressed the main concerns of PEC process i.e. increasing the efficiency and stability of the photoactive materials. In order to achieve the required efficiency target of 10% to be feasible for commercialisation, these issues must be addressed according to Gratzel (2001). According to Cesar et al. (2006) and Kocha et al. (1998), the present stable photoelectrode materials are mostly based on metal oxides which have

low efficiency. Khaselev et al. (2001) experimentally validated two combined PV/electrolysis devices and reached an efficiency of over 16%. Similarly, Licht et al. (2001) studied solar water splitting both theoretically and experimentally and established an efficiency of over 18% solar energy conversion to generate hydrogen fuel. However, the materials used were based on multijunction conventional semiconductor with a short life time (Kurt and Bittner, 2000).

This chapter focuses on the literature review of hydrogen production via electrolysis, photoelectrolysis, and photocatalytic systems as discussed briefly above.

2.2 Hydrogen Production through Electrolysis

Water electrolysis is presently the most extensive industrial process for hydrogen production, and its significance is expected to increase in the future (Linkous, 1992). Vital electrochemical hydrogen production technologies include alkaline, polymer membrane, and ceramic oxide electrolyte. Figure 2.1 illustrates that an electrolyser contains an anode, cathode, an aqueous electrolyte, and an applied potential source. H^+ ions are reduced in cathode, while in anode water is being oxidised. Kainthla et al. (1987) discussed the possibilities of coupling two photovoltaics which was taken a new theorem. The relation of their energy gap to the flat band potential was shown to be very critical. The substances which the principle specifies are appropriate (non-oxides) to form oxides, so that it was essential to coat them with a non-permeable coating.

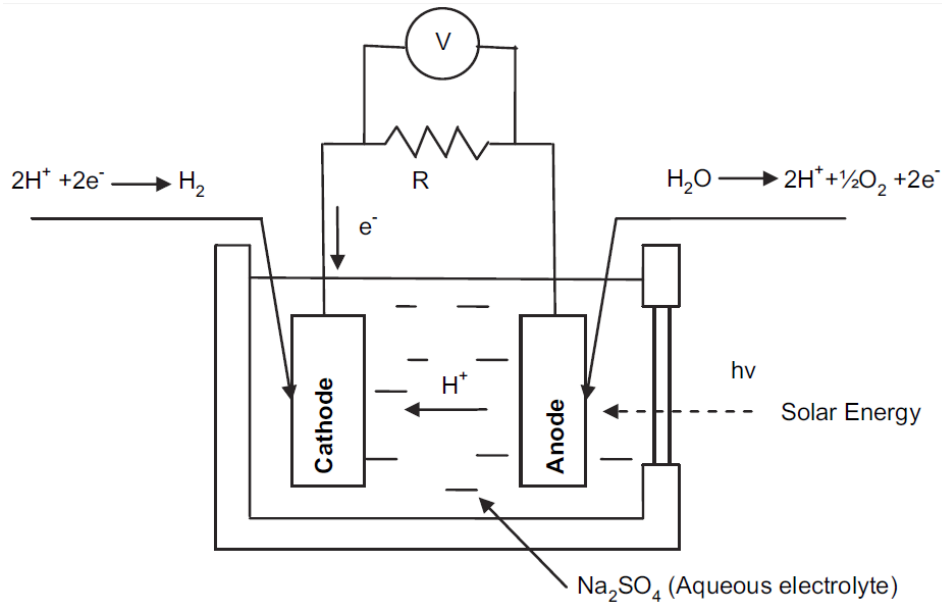


Figure 2.1: Schematic diagram of solar photoelectrolysis (Joshi et al., 2010).

Vijh et al. (1992) investigated different electrode characteristics and their effects on electrochemical stability. They also presented enhanced electrochemical efficiencies and activities (in terms of yield and rate) with increasing electrochemical stability. Apart from electrochemical stability, cost efficiency, abundance, ease of preparation, and environmental impact of the electrodes should also be taken into consideration judiciously while selecting an electrode.

Rausch and Wendt (1992) prepared a number of Raney-nickel cathodes by using different methods and studied their characteristics, as well as hydrogen evolving reaction performances. Pushpavanam et al. (1993) concluded that the activity of the nickel electrodes is improved by coupling it with Raney–nickel, aluminium, or aluminium powders. MacMullin et al. (1999) used electroplating technique to synthesize Nickel–iron alloy cathodes and reported improved electrolytic efficiencies compared to Nickel–only systems.

2.3 Hydrogen Production from Electrochemical Methods

Various scholars have studied diverse areas of electrochemical modeling for diverse practices. For instance Taylor et al. (2013) studied advancement of electrochemical finishing processes through cross innovations and modelling by mathematical and empirical approaches. Mandin et al. (2009) presented electrochemical engineering modelling, both scales theoretical modelling of the electrodes kinetic properties during two-phase sustainable electrolysis. Volgin and Lyubimov (2001) presented mathematical modeling of three-dimensional electrochemical forming of complicated surfaces.

Andersson et al. (2012) performed SOFC modeling considering electrochemical reactions at the active three phase boundaries. In their study it is found that 60% of the polarizations occur in the anode, 10% in the electrolyte, and 30% in the cathode. It is also predicted that the cell current density increases if the ionic transfer tortuosity in the electrodes is decreased or the cell operating temperature is increased. Georgiadou (2003) studied modelling of current density distribution in different electrochemical systems and compared numerical results for local cathodic current density to experimental measurements . Park et al. (2012) conducted an analysis of different chemical, and electrochemical reactions and thermo-fluid flow

in methane feed internal reforming SOFCS and concluded that current density increased with low steam-to-carbon ratio (SCR).

2.4 Chloralkali Modelling

Various researchers have worked on different areas of the chloralkali process. Chikhi et al. (2002) described current distribution in a chloralkali membrane cell. They performed an experimental study and modelling of the membrane cell. Jalali et al. (2009) studied the properties of process conditions on cell voltage, current efficiency and voltage balance of a chloralkali membrane cell. Chandran and Chin (1986) performed a reactor analysis for membrane cell. They also studied electrochemical modeling of the two chamber membrane cell. Yoshida et al. (1989) developed a highly durable low hydrogen overvoltage cathode made of composite-coating a Raney nickel alloy and a metal hydride on a cathode substrate in chloralkali cells and displayed excellent stability under shutdown conditions. Endoh et al. (1988) also developed a low hydrogen overvoltage on a variety of substrates and presented that the cathode exhibits a low hydrogen overvoltage at 50-70 mV at 90°C, at 30 A dm⁻² in a 35 wt% NaOH.

Southworth et al. (2004) studied fugitive mercury emissions from a chloralkali factory and obtained mercury data over a 9-day period. Their principle finding was that fugitive air emissions are episodic and vary with factory operating conditions. McRae (1980) designed an improved integrated and cyclic process that reduced energy costs and wastes while simultaneously controlling impurities important to operation of membrane chloralkali electrolytic cells. O'Brien (1986) presented a method of addition of calcium ions to salt-depleted brine prior to re-saturation while controlling the concentration of sulfate impurity to produce chlorine and high purity alkali metal hydroxide solutions for the electrolysis of aqueous alkali metal chloride solutions.

Rutherford and Ver (1994) proposed a method for reducing calcium and sulfate ion concentration from brine for use in chloralkali membrane plant installations. Furuya and Aikawa (2000) comparatively studied the oxygen cathodes loaded with Ag and Pt catalysts in chloralkali membrane cells and concluded that by optimising the catalyst loading, the lifetime of the oxygen cathodes can be extended further. Ezzell et al. (1984) proposed an electrolytic cell separated into

an anode chamber and a cathode chamber using a membrane comprising of fluorinated polymer membrane to obtain a low-salt caustic for industrial purposes.

A major problem for the chloralkali industry is the contamination of NaOH with chlorate, chiefly when electrolytic cells based on the diaphragm process are employed. Lima et al. (2010) studied the energy losses in chloralkali industry by means of electrochemical diaphragm process. Almeida Filho et al. (2011) compared theoretical and experimental data for current efficiency and concentration of produced NaOH for 34 industrial cells in operation and established a mathematical relationship between the involved variable and performance of the diaphragm of the cell. Vermeiren et al. (2009) developed the casting of an Electrode Diaphragm Electrode (EDE) as a single unit which included the anode, the diaphragm and the cathode operating at minimum cell voltage and highest gas purity possible.

2.5 Heliostat Modelling

The energy and exergy fluxes reflected by the heliostat field depend on factors such as the optical properties of the mirrors. Most of incident radiation of the heliostat is reflected according to its spectral reflectance R_λ . According to Vogel and Kalb (2010) orthodox heliostats use “second surface float glass wet silvered mirrors” which are extremely common in many severe environment applications. They consist of a glass sheet back coated with 700Å silver layer, a 300Å copper layer and 25 μm black paint. The heliostat is made of many flat silver-on-glass mirrors as such, fixed on a metallic structure to form a quasi-paraboloid surface with a focal point at solar tower. The use of silver is justified by its high reflectance in visible range which is of approx. 95% (Zamfirescu and Dincer, 2014).

Kolb et al. (2007) conducted a heliostat cost reduction study and concluded that a more cost effective option is to use aluminum-based stretched metallic mirrors that consist of an aluminum foil stretched over a circular metallic frame prepared of a rectangular steel profile. The aluminum foil is coated with a protective layer such SiO₂ or TiO₂, outlined in Palik (1998) which confers prolonged lifespan while not degrading the spectral reflectance. The spectral reflectance is calculated based on the extinction coefficient of the metal (λ) and the refraction index (Palik, 1998):

$$R_{\lambda} = \frac{(n - 1)^2 + k^2}{(n + 1)^2 + k^2} \quad (2.2)$$

which is valid for normal incidence of the radiation whereas the heliostats are not always positioned normal to the sunrays. Although, some errors will be introduced due to the incidence angle these are relatively small and neglected. During typical design practice the spectral reflectance is not even considered and the reflectance off all heliostats is taken as an averaged value.

Chapter 3: Background

Hydrogen being an abundant element can be found in many constituents in nature such as fresh and sea water, biomass, hydrogen sulphide, and fossil fuels etc. Therefore, to produce hydrogen with zero or low environmental influence, all CO₂ and other pollutants must be processed when hydrogen is extracted from fossil fuels. The primary energy sources to generate hydrogen are thermal, electrical, photonic, and biochemical. Figure 3.1 shows an overview of selected hydrogen production methods with their primary energy sources.

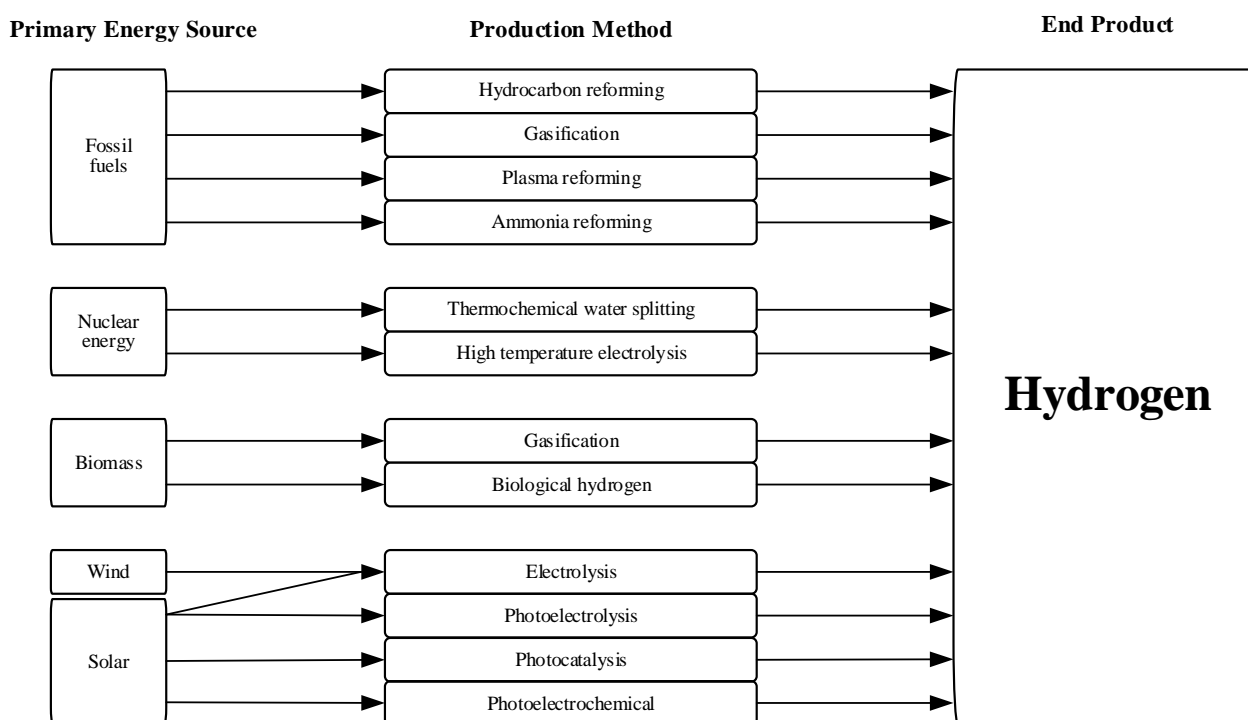


Figure 3.1: Selected hydrogen production methods along with their primary energy source (Adapted from Acar and Dincer, 2014).

3.1 Water Splitting

Water decomposition is a multi-electron chemical process. For a complete reaction cycle, two molecules of water is required to generate one molecule of oxygen and two molecules of hydrogen. At standard conditions, the energy required to drive the reaction is 4.915 eV. This energy can be generated by either of the following ways (Zamfirescu et al., 2011):

- One photon of ultraviolet light with a wavelength shorter than 252.3 nm

- Two photons in the visible spectrum with a wavelength shorter than 504.5 nm
- Four infrared photons of 1.23 eV

For a full reaction cycle to occur, 4 valence electrons of two water molecules must be dislocated. This is not accomplished usually even at high energy with a single photon since one photon can dislocate only a single electron on a higher energy band. Therefore, at least two photons are needed for driving half a cycle and the two other in a following reaction to complete the water splitting process (Zamfirescu et al., 2011).

In nature, photosynthesis is the basic mechanism to split the water molecule. It works through intermediate storage of photoelectrons in complex catalytic cycles. The existing commercial technology of splitting water is based on electrolysis, which can be driven by solar-derived electricity. In an electrolysis process, electrodes are used to “inject” electrons into water for driving the oxygen and hydrogen half-reactions for splitting of water. As mentioned above, the energy to drive the reaction is 1.23 eV in standard conditions, for 4 electrons. Thus, the difference of potential between the electrodes must be at least 1.23 V. The electricity required to drive electrolysis can be obtained from a photovoltaic panel or a solar heat engine, thereby assembling in this way a solar hydrogen generation device (Zamfirescu et al., 2011).

3.2 Photocatalytic Water Splitting

The conceptual design of the photo chemical water splitting reactor is shown in Figure 3.2, which illustrates a vessel comprising two photochemical reactors separated by a proton exchange membrane (PEM). The right side exposed to solar radiation. On the right side, the water photo-oxidation reactor is located, in which selected supramolecular photo-catalysts are dissolved in a proper quantity to generate electrical charges at reaction sites to oxidize water and produce oxygen gas and protons, according to Eq. (2.1). The electrons are “donated” by supramolecular complexes to a positively charged electrode. Fresh water is continuously supplied to this reactor, while all other chemicals remain in solution. The flow rate of fresh water is adjusted such that the water level in the vessel remains constant. The protons released by the photochemical oxidation reaction are driven by a concentration gradient and they cross the proton exchange membrane. In the water reduction reactor, selected supramolecular complexes for photocatalytic reduction of water to hydrogen are dissolved in proper concentration. These catalysts generate

photoelectrons which facilitate reactions (2) e (3) to occur. Electrons, which are transferred from the oxygen-evolving reactor are donated at the electrode surface to the supramolecular devices, which under the influence of photonic radiation transmit negative charges to the reaction sites. Water is not consumed in a steady-state operation; the only overall reaction in this reactor is that of proton reduction to form hydrogen gas. Above the liquid level, the product gases (oxygen and hydrogen, respectively) are continuously extracted with the use of external fans, which maintain low pressure in the system. In order to avoid effective water migration through the proton exchange membrane, the pressure is maintained at about the same level on both sides. In a practical implementation, the photochemical reactor can be constructed with a flat plate type geometry. Some part of this incident radiation (UV and V spectra) is used for the photochemical reaction. The remaining portion (mostly IR) can be used to heat water by a flat panel below the photochemical reactor. A combined hydrogen and heating system can be devised in this way.

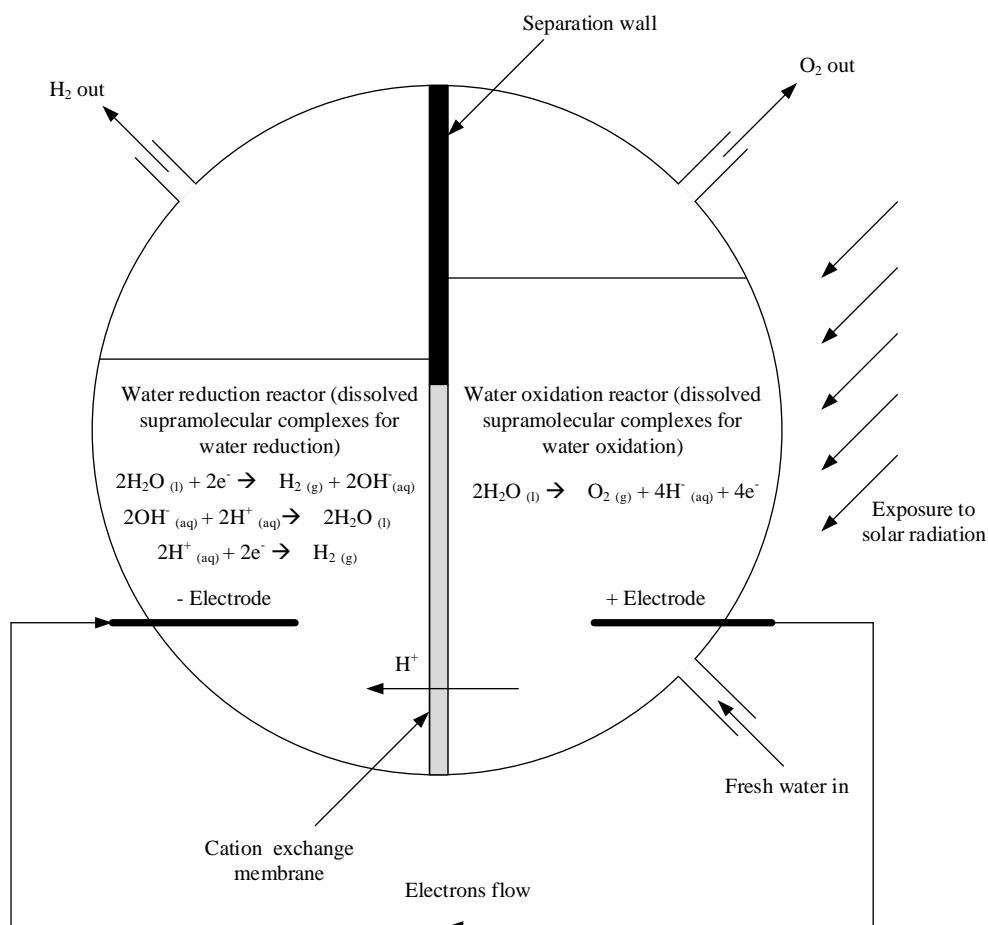
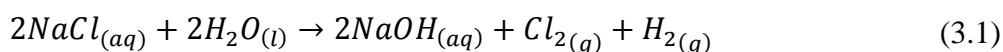


Figure 3.2: Conceptual design of the photochemical water splitting reactor (Adapted from Zamfirescu et al., 2011).

Acar et al. (2014) comparatively assessed visible light-driven heterogeneous photocatalysts for hydrogen production based on technical, environmental, and cost criteria. In their study, photocatalysts are compared based on their (i) rate of hydrogen generation per gram; (ii) rate of hydrogen generation per m² of the specific surface area; and (iii) the band gap energy. They also compared and discussed photocatalysis systems in terms of flammability, reactivity, and their impact on living systems' health.

3.3 Chloralkali Process

As mentioned previously, the chloralkali industry is one amongst the chief electrochemical processes predominantly producing chlorine and sodium hydroxide (caustic soda). The chloralkali process involves the electrolysis of sodium chloride solution (brine) that produces chlorine gas at the anode and sodium hydroxide (caustic soda) at the cathode. The overall chemical reaction can be written as follows (O'Brien et al., 2007; Schmittinger, 2008):



A separator is used between the anode and cathode compartments to avert the mixing of anolyte and catholyte. In the diaphragm cell process, a permeable diaphragm is used to separate the anode from the cathode compartments which is typically made of asbestos fibers. This technology yields a weak caustic stream contaminated with sodium chloride having a concentration of about 30%. Conversely, a mercury cell process is divided into two units: the electrolyser and a secondary electrochemical reactor also commonly known as decomposer. In a mercury cell process, high purity strong caustic solution having a concentration of about 50% is produced (O'Brien et al., 2007; Schmittinger, 2008). In the electrolyser, chlorine gas is produced at the anode and sodium amalgam is produced at the cathode. Furthermore, the sodium amalgam enters a secondary electrochemical reactor. Here, water decomposes into sodium hydroxide and hydrogen gas contaminated with traces of mercury.(Dias, 2005; Schmittinger, 2008).

3.3.1 Membrane Cell Chloralkali Process

With the diaphragm cell process and mercury cell process having contaminated hydrogen gas, the membrane cell process appeared as an alternative to the diaphragm and mercury cells. The membrane cell process is precisely alike to the diaphragm cell where the permeable diaphragm is

replaced by a selective ion-exchange membrane. It also has several advantages over the other processes mainly being highly efficient energetically with high purity caustic soda with lesser environmental impact (Dias, 2005; O'Brien et al., 2007; Schmittinger, 2008). This process also requires a high quality input brine to evade membrane polluting.

Figure 3.3 shows schematic representation of the chloralkali membrane cell process. Chlorine ions are oxidised to chlorine gas at the anode where saturated sodium chloride solution is fed. The sodium ions migrate through the membrane to the cathode compartment. In the cathode compartment, water reduction takes place and hydroxyl ions are produced. Here, the migrated sodium ions combine with the hydroxyl ions. Consequently, hydrogen gas is produced in the cathode. The reactions evolved in this process can be written as follows (Dias, 2005; O'Brien et al., 2007; Schmittinger, 2008):

At the anode:



At the cathode:

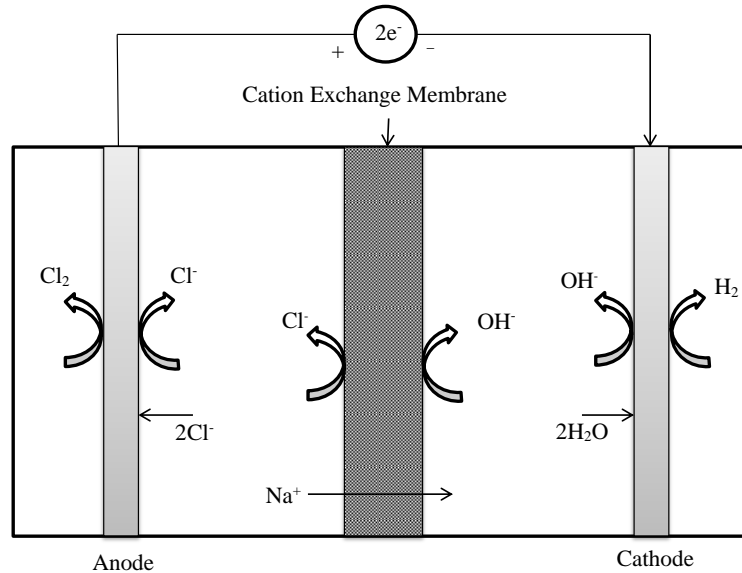
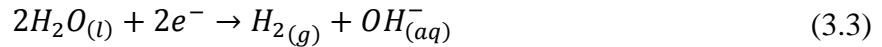


Figure 3.3: Schematic representation of the chloralkali membrane cell process (Adapted from Dias, 2005).

3.3.2 Thermodynamics of Electrochemical Reactions

The electrochemical reactions can advance spontaneously or can be driven by an electric potential. Electrochemical cells where electrode reactions take place spontaneously ($\Delta G < 0$) are called galvanic cells. Conversely, electrochemical cells where chemical reaction is driven by a power supply is characterised as electrolytic cell ($\Delta G > 0$). The Gibbs free energy (ΔG) of an electrochemical reaction at constant temperature and pressure can be written as follows (Hamann et al., 2007):

$$\Delta G = -nFE^0 \quad (3.4)$$

Here, n denotes the number of electrons transferred, F is the Faraday's constant which is the charge required to drive a mole of electrons and E^0 is the standard electrode potential. The minimum electrical work requirement supplied to an electrolytic cell to drive the electrochemical reactions is denoted by ΔG . Table 3.1 shows the anode and cathode potentials for normal operating conditions (90°C, 1 bar, 3.5 M of NaCl and 10 M of NaOH) in a chloralkali membrane cell process.

Table 3.1: Equilibrium electrode potentials for the half electrochemical reactions in a typical chloralkali membrane cell process (Data taken from Schmittinger, 2008).

	Reaction	E^0/V
<i>Anode</i>	$Cl_{2(g)} + 2e^- \rightarrow 2Cl_{(aq)}^-$	1.23
<i>Cathode</i>	$2H_2O_{(l)} + 2e^- \rightarrow H_{2(g)} + 2OH_{(aq)}^-$	-0.99
<i>Overall</i>	$2NaCl_{(aq)} + 2H_2O_{(l)} \rightarrow 2NaOH_{(aq)} + Cl_{2(g)} + H_{2(g)}$	-2.23

3.3.3 Charge Transport in Aqueous Electrolytes

Charges exist as electrons and ions in an electrochemical system. The negatively charged electrons transport through the external circuit from the anode where they are produced to the cathode where they are consumed. The accumulation of ions on the surface of the electrode generates a potential and a concentration gradient. This gradient drives the transport of ions through the electrolytes. Table 3.2 summarises the three major driving forces for charge transport through the electrolytes. Conduction process is driven by temperature (T) difference where

thermal conductivity of the medium plays a major role. In diffusion, driving force is concentration (c) difference and the rate of this process is calculated based on the diffusivity of the medium. Lastly, pressure difference (p) drives convection which also depends on viscosity of the medium.

Table 3.2: Transport processes for charge transport in electrolytes (Adapted from O'Hayre et al., 2006).

<i>Transport process</i>	<i>Driving force</i>	<i>Coupling coefficient</i>	<i>Equation</i>
Conduction, J_m	$\frac{dT}{dx}$	Conductivity, σ	$J = \frac{\sigma}{ z_i F} \frac{dT}{dx}$
Diffusion, J_d	$\frac{dc}{dx}$	Diffusivity, D	$J = -D \frac{dc}{dx}$
Convection, J_c	$\frac{dp}{dx}$	Viscosity, μ	$J = \frac{G_c}{\mu} \frac{dp}{dx}$

In case of metal electrodes, only electric potential gradient drives the electron charge transport. However, in electrolyte solutions, transport mechanisms can be driven by conduction, diffusion and/or convection. The most significant driving force for charge transport in a membrane cell process is the electrical potential gradient which is produced due to the depletion of anions (or accumulation of cations) on the surface of anode and conversely, the depletion of cations (or accumulation of anions) on the surface of cathode. As a result, the positively charged cations transport from the anode to the cathode compartment. The ability of a material to conduct electric current is affected by the material properties and the temperature is measured by its conductivity. The following equation relates the conductivity to the resistance of a conductor:

$$R_c = \frac{l}{\sigma A} \quad (3.5)$$

Here the conductor resistance is denoted by R_c , the conductor conductivity is denoted by σ . l is the length of the conductor and A is the cross-sectional area of the current flow. From Table 3.2, it is clear that the charge transport due to electric field is directly proportional to the potential gradient. The cell potential (E) applied is related with the rate of electric charge flow in accordance to Ohm's law:

$$E = Rj \quad (3.6)$$

where j is the current density through the cell.

3.3.4 Charge Transport through Ion Exchange Membranes

The function of ion exchange membranes are essentially as a separator. In electrolysis process, cation exchange membranes containing fixed negatively charged ions are used to stop the transportation of anions from cathode compartment to anode compartment. (Strathmann, 2004). The fixed ions of the membrane are in equilibrium with the counter ions whereas the ions that carry the same charge as the fixed ions (co-ions) are efficiently excluded from the membrane matrix. This effect is called as the Donnan exclusion effect as explained in Figure 3.4 (Mulder, 1996).

The most significant characteristics of an ion exchange membranes are the following: high permselectivity for counter-ions (excluding co-ions), high ionic conductivity, good mechanical form and chemical stability (Strathmann, 2004). The permselectivity of an ion exchange membrane refers to the ability of the membrane to reject co-ions. As a result of the Donnan exclusion effect, the permselectivity is affected by the electrolyte concentration of the surrounding solution and by the ion-exchange capacity of the membrane. An ideal permselective membrane should completely dismiss co-ions from the membrane matrix.

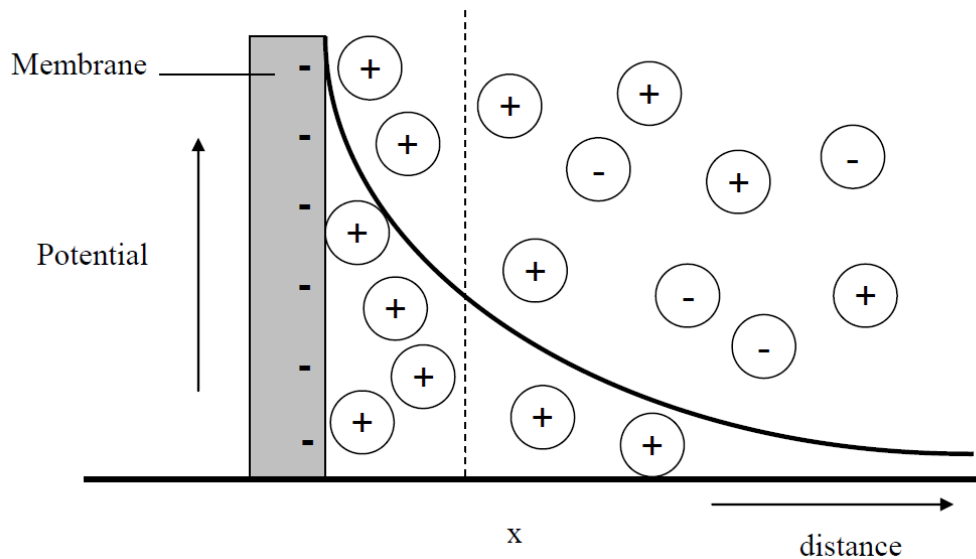


Figure 3.4: Illustration of the Donnan exclusion effect (Adapted from Mulder, 1996).

The ionic concentration of the electrolyte solution is subject to the concentration of the electrolyte solution which affects the swelling of the membrane (water content in the membrane). Additionally, the water content of the membrane, interaction between the mobile and fixed ions and temperature affects intensely the mobility of the ions through the membrane matrix. In general, water content increases the free volume inside the membrane matrix which improves the ability of ions to move across the polymer (Strathmann, 2004; Dias, 2005).

3.3.5 Mass Transport of Reactants

In electrochemical reactions, transport of the reactants from the bulk of the solution to the electrode surface and the removal of products from the surface are inherent steps. When these steps are slow and or the electric field very high, the mass transport at the surface of the electrodes become rate controlling and adversely affects the rate of the electrochemical reaction. This phenomenon is called concentration polarization and is often neglected in the electrolysis process because the raw materials are supplied in excess and no limitations to the mass transport are normally found (Dias, 2005).

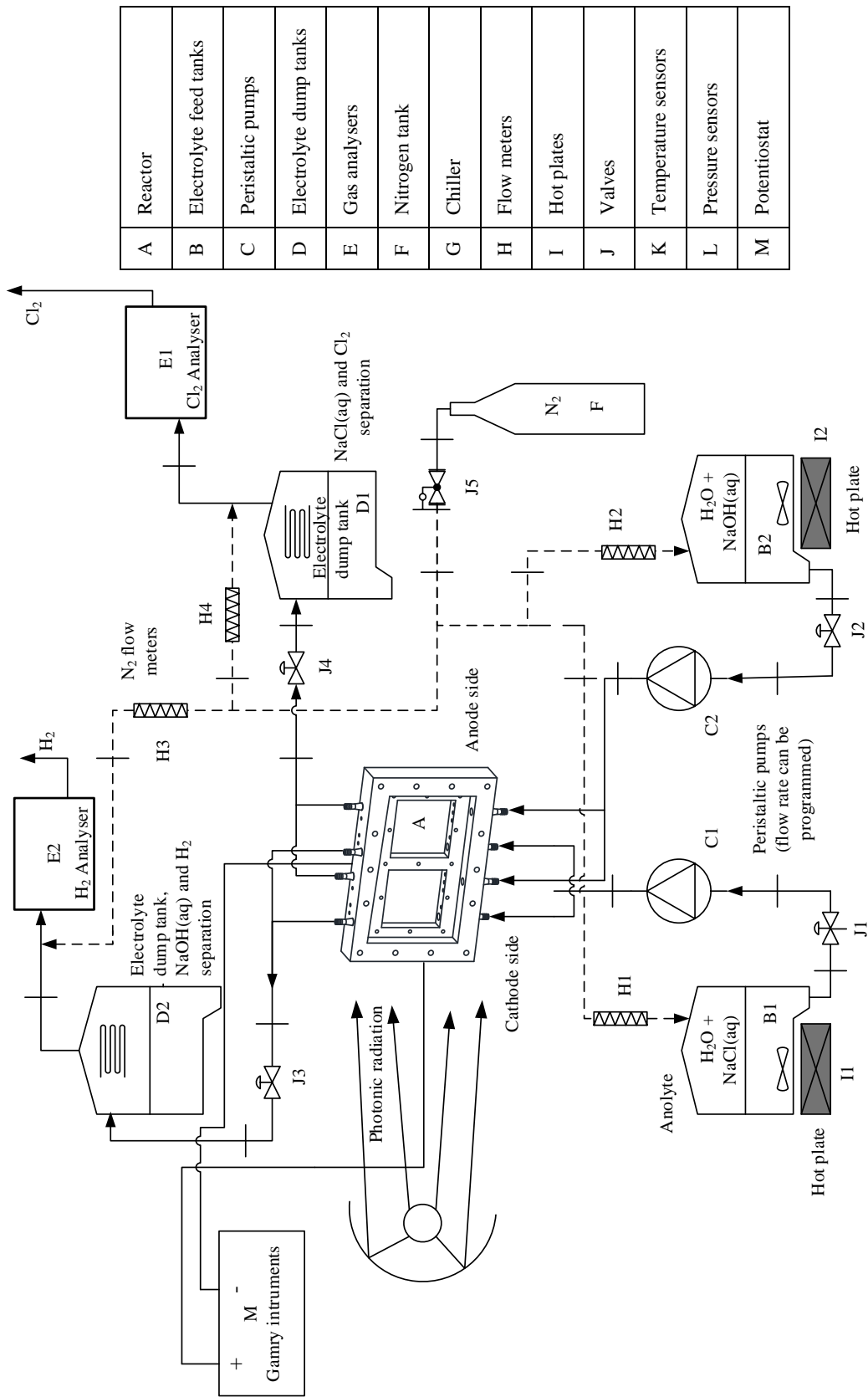
Chapter 4: Experimental Apparatus and Methodology

4.1 System Description

Figure 4.1 presents the process flow diagram of the experimental setup. Aqueous solution of sodium chloride (NaCl) and water (H₂O) present in electrolyte feed tank B1 is fed to the anode side of the reactor (A in Figure 4.1). Likewise, aqueous solution of sodium hydroxide (NaOH) and water (H₂O) present in electrolyte feed tank B2 is fed to the cathode side of the reactor. Note that the electrolytes in feed tanks B1 and B2 are heated using hot plates I1 and I2 respectively and also stirred using magnetic stirrer bars. Before entering the reactor, the electrolytes pass through stop valves and then through the peristaltic pumps (C1 and C2) where the flow rates are externally connected and controlled by a designated computer.

After passing through the reactor, the depleted aqueous solution of sodium chloride is dumped to the electrolyte dump tank (D1 in Figure 4.1). Here the gas (mostly chlorine) is allowed to escape from the top of the dump tank and fed to the gas analyser (E1) where the concentration of chlorine gas is measured. On the other hand, aqueous solution of sodium hydroxide along with the gases produced is fed to the electrolyte dump tank (D2). Here, the gas (mostly hydrogen) is allowed to escape from the top of the dump tank and fed to the hydrogen gas analyser (E2) where the concentration of hydrogen gas is measured. The dotted lines in Figure 4.1 represent the nitrogen gas pipe. Nitrogen is purged through the reactor prior as well as the conclusion of the experiment to keep the PEC reactor away in contact with air (especially oxygen) at all times.

Figure 4.2 shows the experimental setup at UOIT CERL laboratory. A support structure is designed to maintain the reactor tilted by 1 degree for the gases to escape from the cathode and the anode. The hoses are directly connected to the pump and further connected to the electrolyte reservoirs (feed and dump tanks). Valves and T-connectors used to switch between the electrolyte and nitrogen hoses. Figure 4.3 shows the electrical contacts connected to the potentiostat using crocodiles. Figure 4.4 shows the use of solar simulator as a replacement for sunlight with light intensity directly shined on the cathode compartment during experiments. Figure 4.5 shows the rust formed from the use of low quality stainless steel washers which highly affects the experimental results.



A	Reactor
B	Electrolyte feed tanks
C	Peristaltic pumps
D	Electrolyte dump tanks
E	Gas analysers
F	Nitrogen tank
G	Chiller
H	Flow meters
I	Hot plates
J	Valves
K	Temperature sensors
L	Pressure sensors
M	Potentiostat

Figure 4.1: Process flow diagram of the novel photoelectrochemical hydrogen production system.

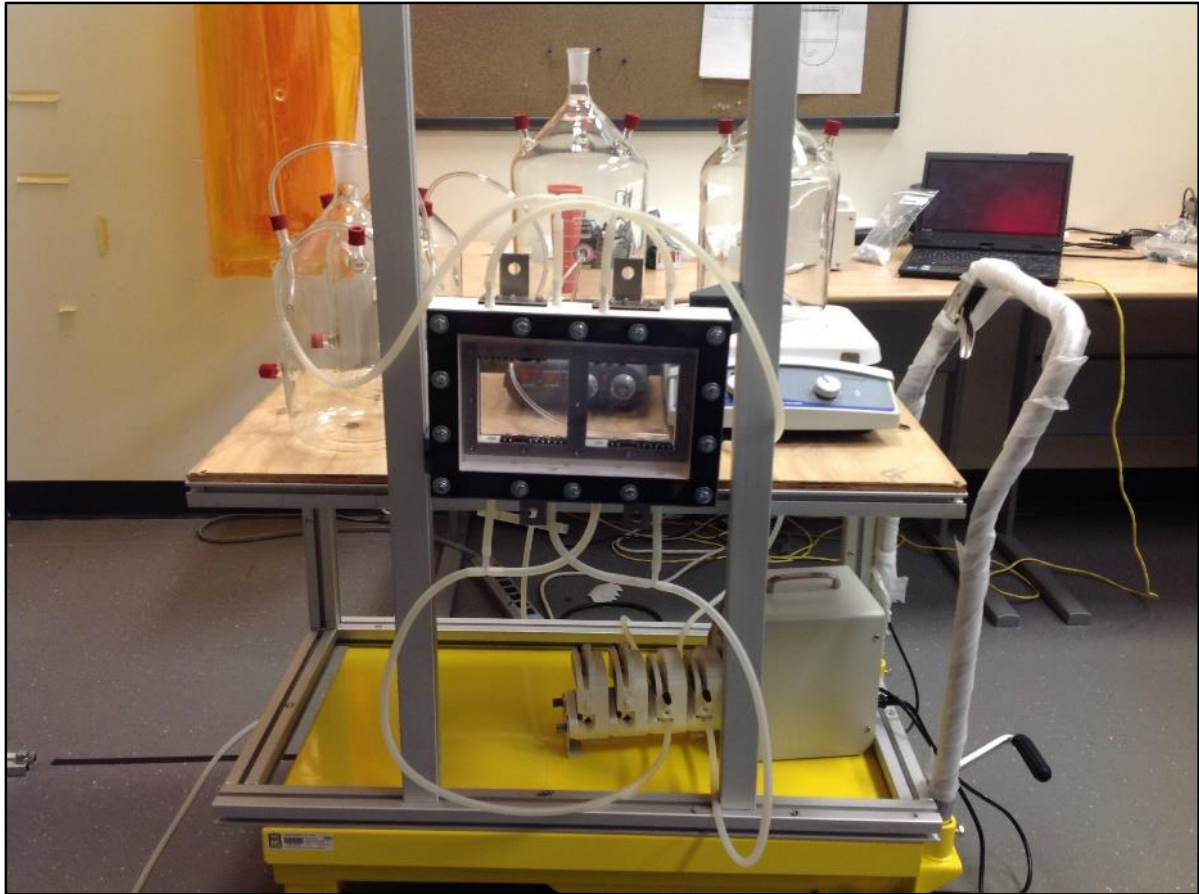


Figure 4.2: Overall PEC system setup.

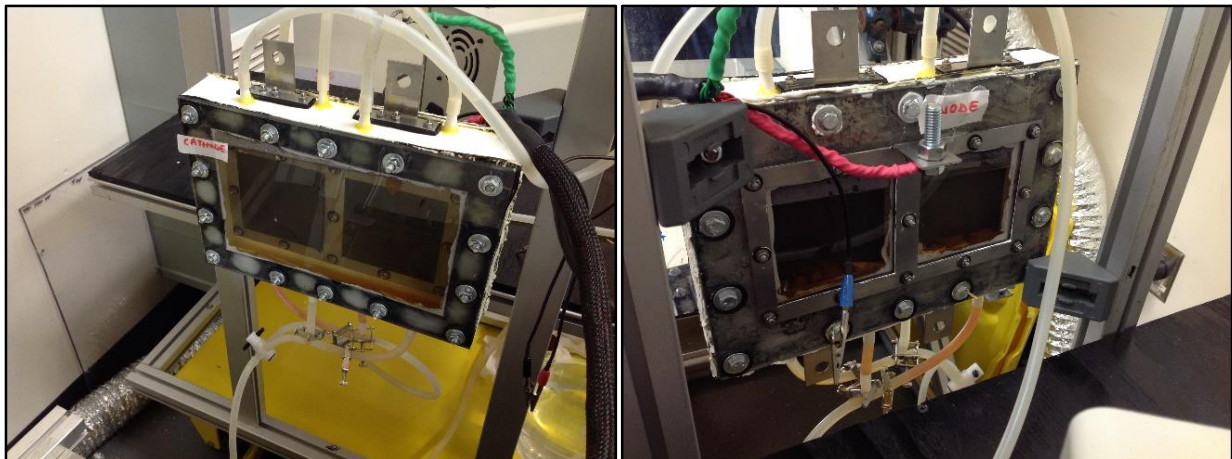


Figure 4.3: Cathode and anode sides of the reactor during operation.

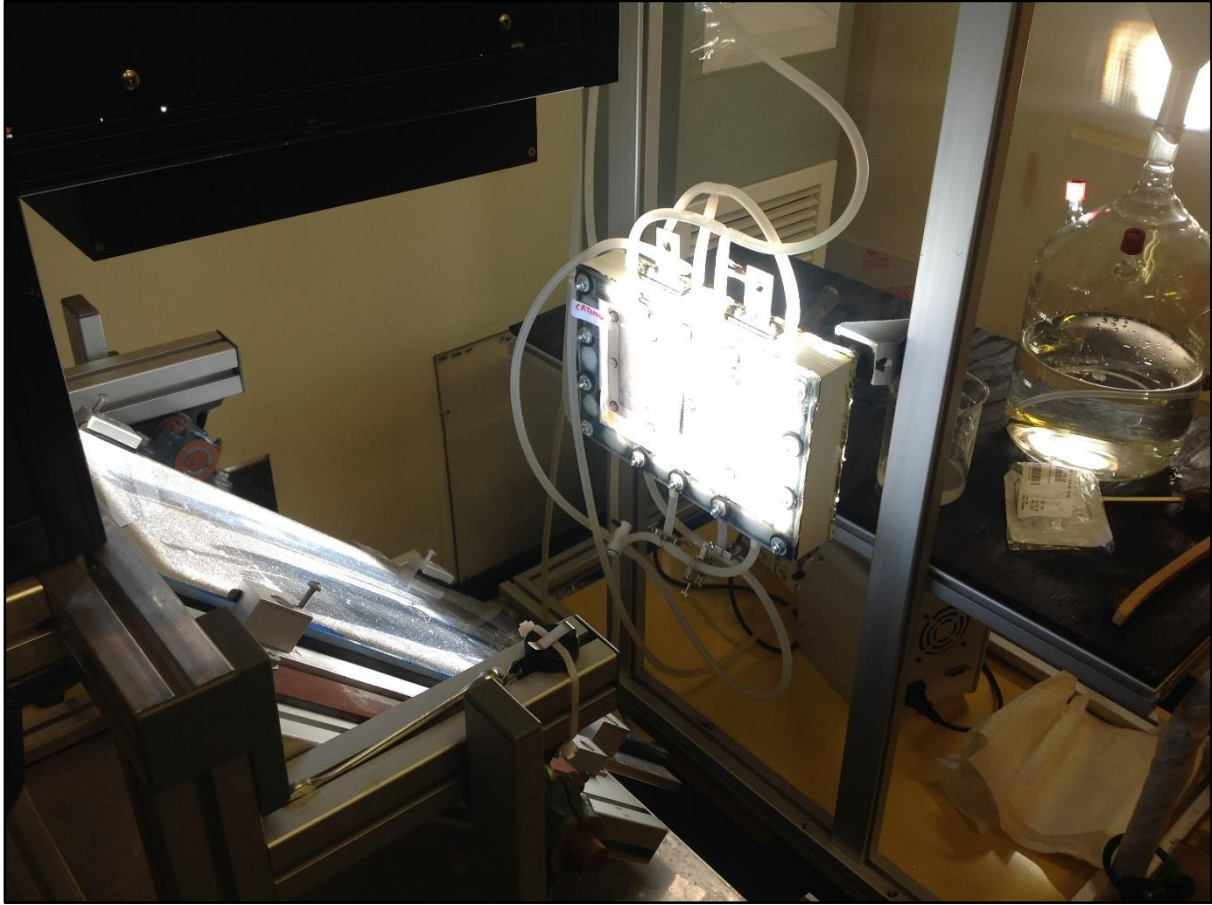


Figure 4.4: PEC system exposed to solar simulator.



Figure 4.5: Anode side oxidation due to damage in stainless steel washers.

4.2 Reactor Design

The efficiency of water electrolyzers depends on the proper design of system components (cells, cell stacks, gas-liquid separators, etc.). In particular, the gas-liquid circulation flow rate and the gas-liquid separation efficiency are important system parameters playing a significant role in overall performance of the units. These quantities, which are dependent on the gas-liquid flow patterns, could be calculated and analysed using proper gas-liquid flow models and computer modelling tools.

The design of the photoelectrochemical reactor was carefully and precisely designed in AUTOCAD® and SOLIDWORKS®, keeping in mind several key points such as the inlet and outlet holes positions and diameters. To improve the designs of electrolyser reactor, the general-purpose CFD software, ANSYS (2011), has been used to model the flow of water in electrolysis units under typical and alternative conditions. The CFD simulation results have been used to properly design the system components (cells, anode, cathode, membrane etc.). ANSYS is a well-recognized general-purpose CFD software package that has been validated and successfully used around the world for more than 20 years. Its main features and capabilities have been described in ANSYS (2011). The software serves as a cost-effective and convenient framework for modelling and design when a proper CFD model has been developed and validated for a particular application. The detailed CAD drawings are provided in Appendix A.

4.2.1 Modelling Approach

The modelling approach is based on applying the standard $k - \varepsilon$ (built-in) CFD model available in the FLUENT software. This package enables us to account for the differences (slips) in velocities and temperatures of gas and liquid and calculate 3-D distributions of pressure, velocity components, temperatures and volume fractions. In the FLUENT, the two-equation conservation equations are solved under specified operating conditions with appropriate boundary conditions, turbulence models and constitutive inter-phase correlations. The drag force (skin friction coefficient) and wall shear stress between liquid and solid phases are calculated. The cathode section of the reactor was first modelled in SolidWorks® with one water inlet and outlet for $NaOH + H_2$ gas-liquid mixture as shown in the left side of Figure 4.6. The model was then modified to two inlets and two outlets as shown in the right side of Figure 4.6.

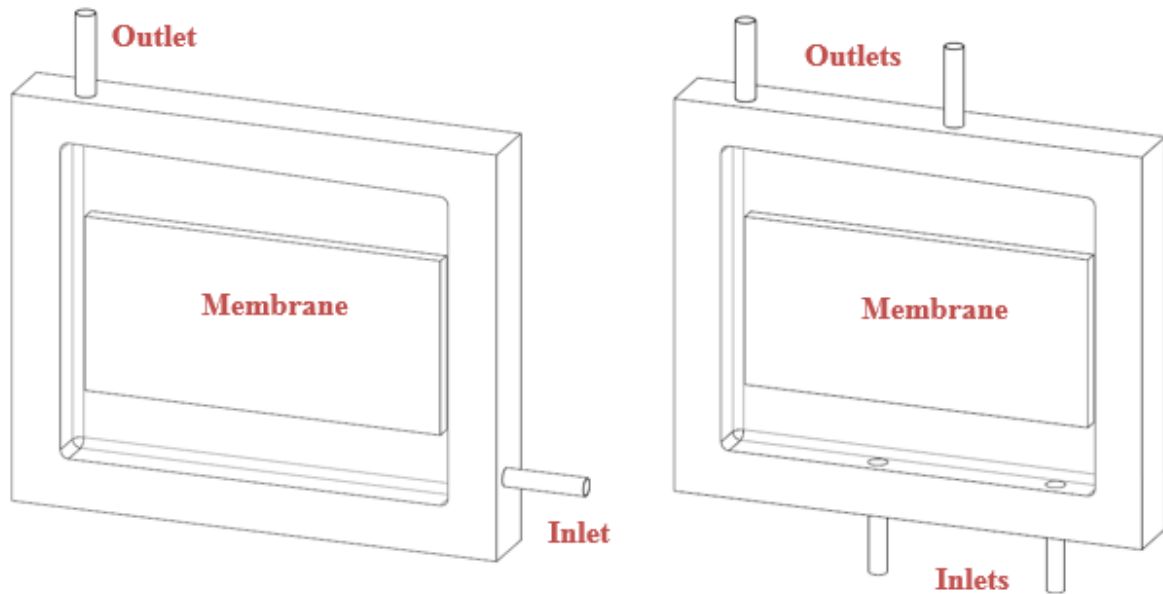


Figure 4.6: (Left) initial design (1 inlet 1 outlet), (right) modified design (2 inlets, 2 outlets).

The membrane can be modelled as a simple rectangular box (bluff body) approximately 10mm thick attached at the back wall of the reactor (shown in Figure 4.6). The reaction rate and the production of gases depend entirely on how well the water from the inlet pipe/hose arrives inside the reactor and encounters with the membrane. The more surface area of the membrane coming in contact with the incoming water, better the efficiency of the reaction that takes place inside the reactor.

If we take a cross section A-A from the modified model as shown in the Figure 4.7, we can see the side view of the membrane. This enables us to illuminate three different cases of 2D CFD problems as following:

- Case 1: Front view of initial model with one inlet and one outlet (Figure 4.6, left).
- Case 2: Front view of modified reactor with two inlets and two outlets (Figure 4.6, right).
- Case 3: Side view of modified reactor where the membrane is considered as a bluff body (Figure 4.7).

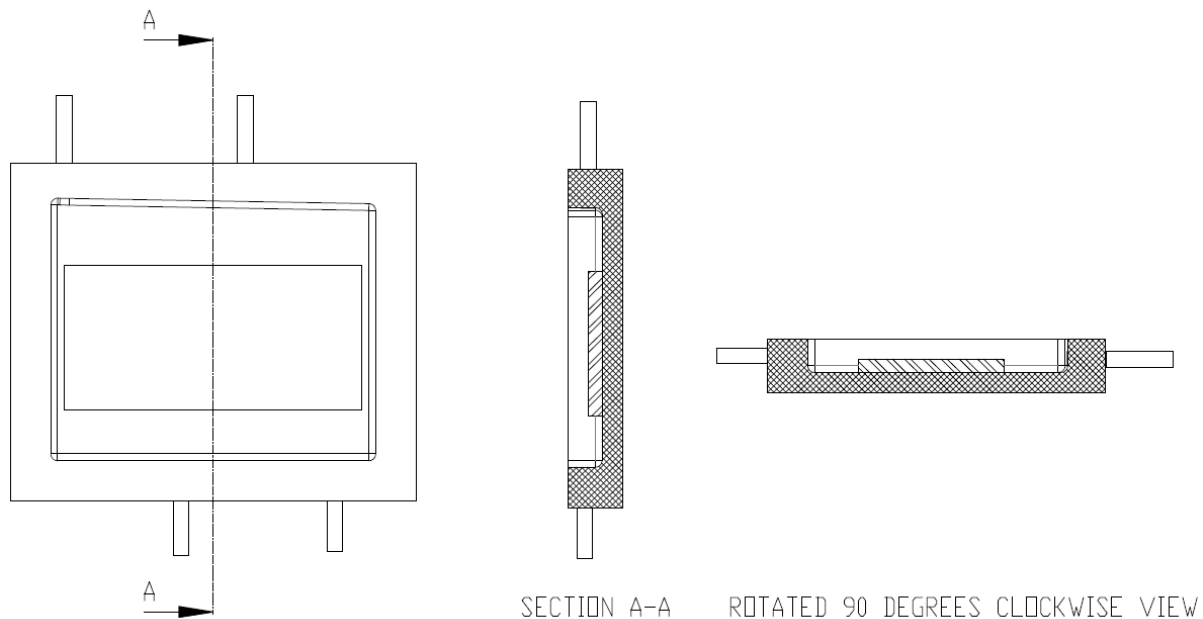


Figure 4.7: Cross section view to model the liquid flow over the membrane.

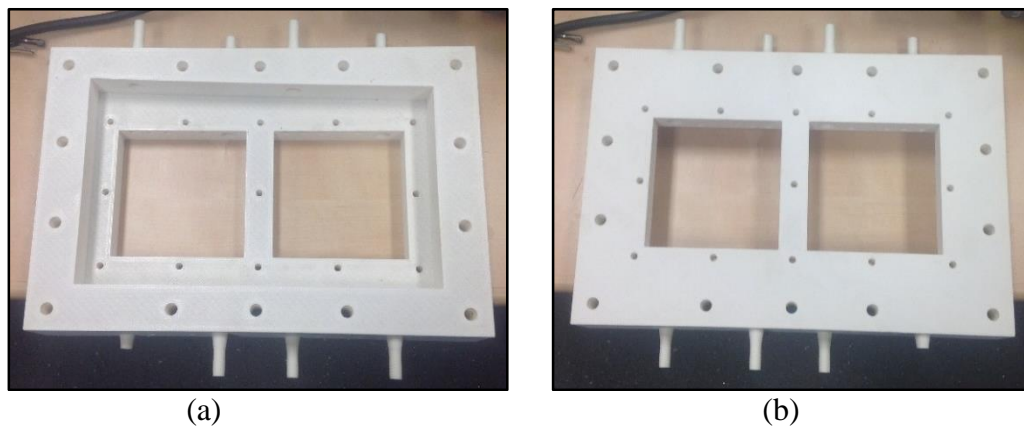


Figure 4.8: (a) Front/top view after rapid prototyping, (b) back view after rapid prototyping.

Figure 4.8 shows the finished manufactured part from the 3D printer. The photoelectrochemical reactor core materials are described in Table 4.1. Every part of the PEC reactor is being prudently designed using mechanical design softwares such as AUTOCAD[®] and SOLIDWORKS[®]. The remarks section justifies the reason for selecting the particular material/company during the selection process. For instance, the PEC electrolyser cell was built using rapid prototyping (3D printing) technology that uses acrylonitrile butadiene styrene (ABS) material. As discussed previously, the nature of the electrolyser is such that the same cell can be used in two different configurations i.e. chloralkali and water splitting. Hence, highly resistant

and lightweight ABS material was chosen since the chloralkali cycle involves chlorine gas which is a good oxidising agent.

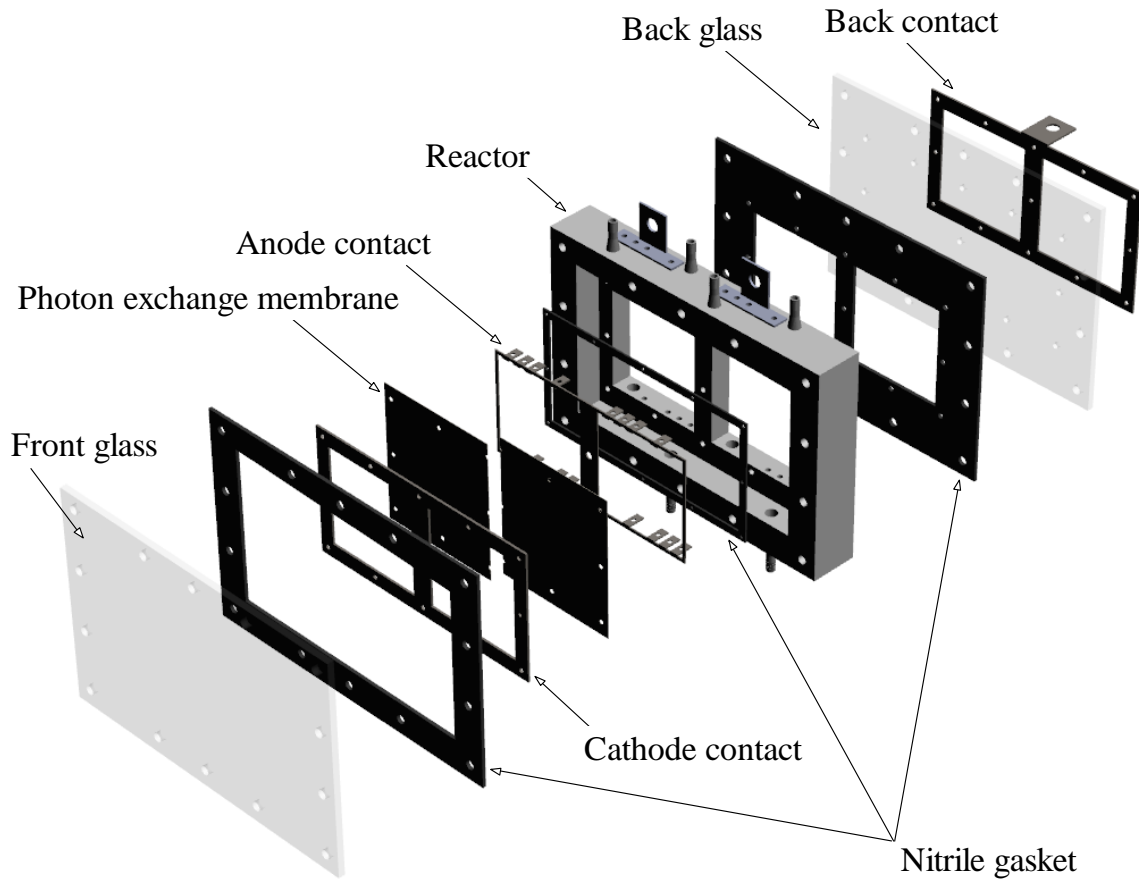


Figure 4.9: Extended view of photoelectrochemical reactor.

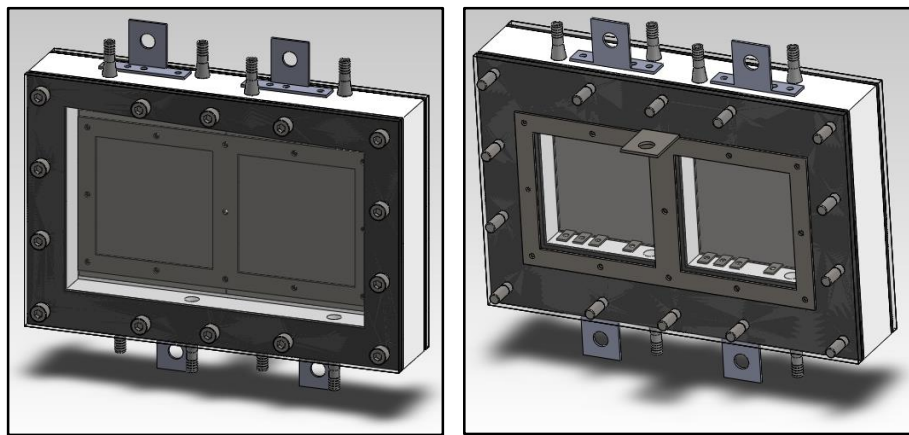


Figure 4.10: Reactor assembly model sketched in SolidWorks.

Table 4.1: Properties of reactor core components.

Part	Material	Company bought from	Remarks
Reactor Chamber	Acrylonitrile Butadiene Styrene (ABS)	Cimetrix Solutions, Oshawa, Canada	ABS polymers are resistant to aqueous acids, alkalis, concentrated hydrochloric and phosphoric acids, alcohols, and animal, vegetable, and mineral oils
Nitrile Gaskets x 3	Nitrile Rubber	Parts and Shapes, Oshawa, Canada	Compressibility, flexibility, and strength have been taken into justification during the selection process of gaskets for the reactor.
Anode and Cathode Contact	Stainless Steel 316	Durmach, Oshawa, Canada	Type 316 stainless steel are more corrosion resistant than those made from 18-8 stainless steel. They are also resistant to chemicals and solvents.
Hydrogen Screener Membrane Electrode Assembly x 2	Non-woven Carbon Fibres + PTFE + Carbon Black + PFSA + Catalyst (Pt on C)	Alpha Aesar Ward Hill, MA, USA	Bigger active surface area and light sensitive cathode
Front and Back window	Glass	UOIT Stores, Oshawa, Canada	The purpose of using glass is to: 1. observe the reactions with naked eye; 2. illuminate the cation exchange membrane (cathode side) of the reactor directly with sunlight.

Figure 4.9 shows the exploded view of the designed PEC reactor. Figure 4.10 shows the front and back isometric views of the SolidWorks model for the reactor.

4.3 Electrical Contacts Installation

The anode and cathode side of the reactor needs to be in contact with a conductive material (in this case stainless steel 316 is used) so that the electrolyte has a constant supply of electrons. These electrons can be supplied by various sources such as a PV array. The bending process of the anode is shown in Figure 4.11a, b, and c. It is important to note that bending must be done in the right direction because of the non-symmetric positions of the contacts. Figure 4.11d shows

the anode being placed on the reactor supported by rubber gaskets, tightened by rods, washers. The anode contact is made of stainless steel 316 and has a thickness of 2mm.

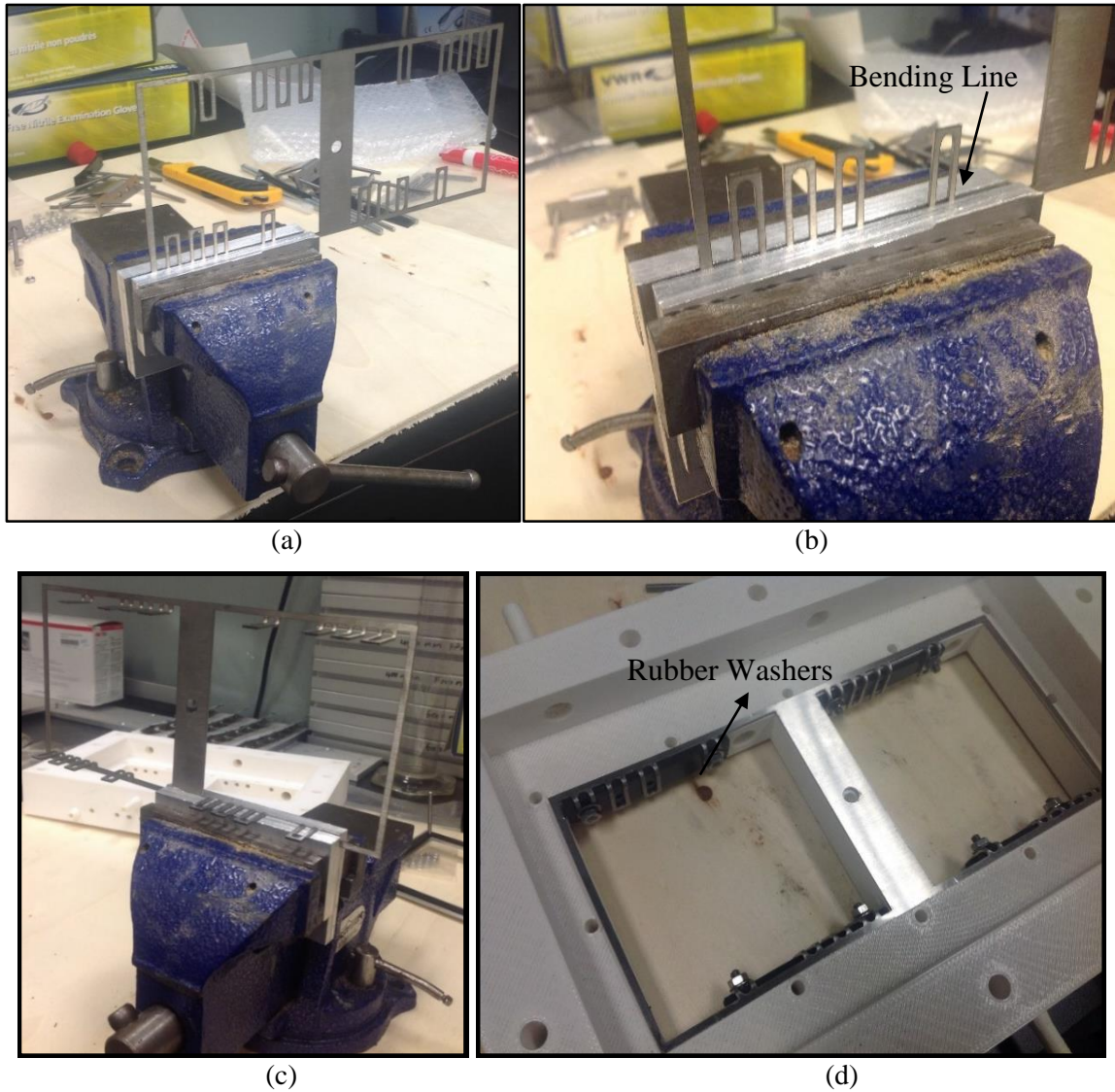


Figure 4.11: Anode bending process (a) mounting on bench vice, (b) adjusting height, (c) bending using hammer, (d) after installation in the reactor using gaskets.

The details of the electrical contacts installation can be seen in Figure 4.12. After successfully bending and installation of the anode contact, a plastic film was used as a dummy membrane prior to the MPEA membrane. Details of the membrane installation is given in section 4.4.

4.4 Membrane Installation

The installation of the hydrogen screener membrane electrode assembly is one of the most challenging tasks, mainly because of the following reasons:

- Any contact of the membrane surface with atmospheric air should be avoided since this affects the lifespan of the membrane.
- Any purging of the MPEA should only be done with inert gases such as nitrogen.
- MPEAs will not work well when they are not fully humidified.
- An activation process as suggested by the manufacturer should be followed before use.
- Excessive differential pressure between anode and cathode may damage the membrane.

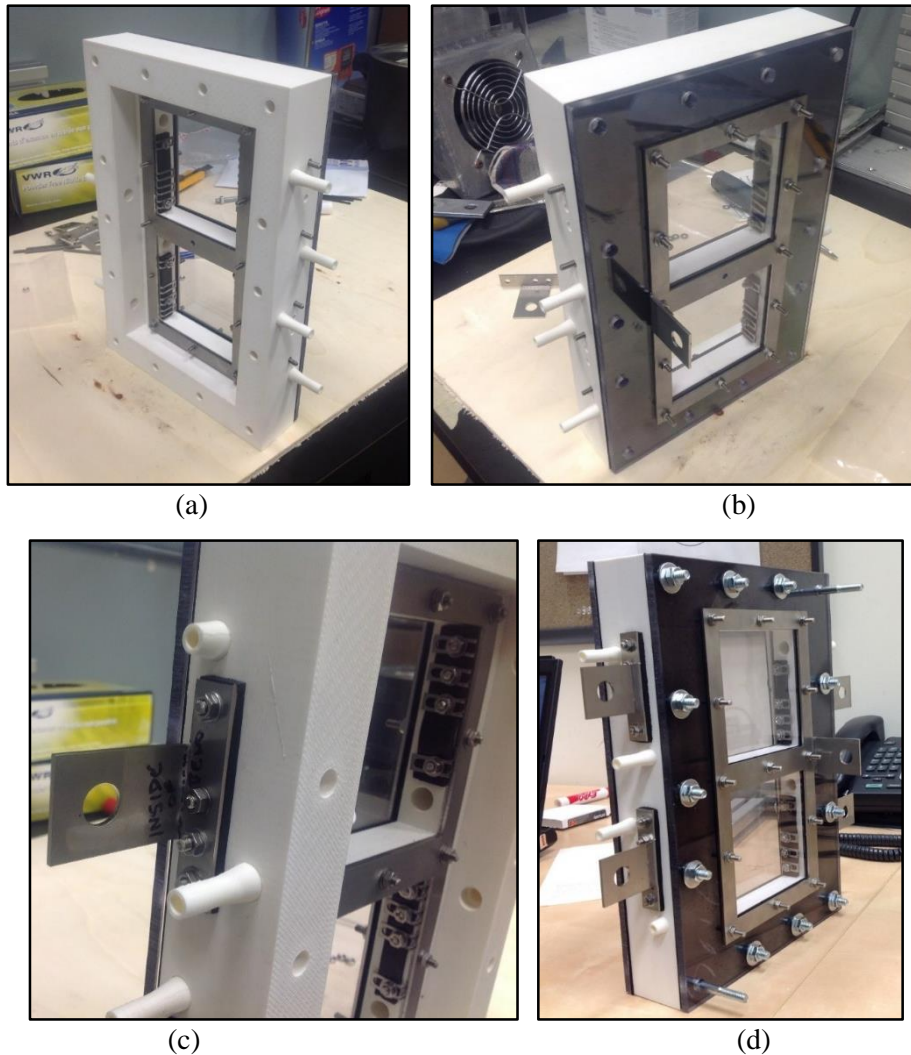


Figure 4.12: (a) Cathode contact, (b) back contact, (c) side contact, (d) back view of the reactor after contacts installation.

Due to the nature of the difficulty in the installation of the membrane, the installation process is done in the glove box in CERL lab which is constantly purged with Nitrogen gas. The reactor and all the other components along with the membrane is carefully placed inside the glove box before purging the glove box with nitrogen gas as shown in Figure 4.13. To complete seal the reactor, silicon glue is applied on the rubber gaskets and glass window is placed on top which closes any path for oxygen to come in contact with the membrane as shown in Figure 4.14.

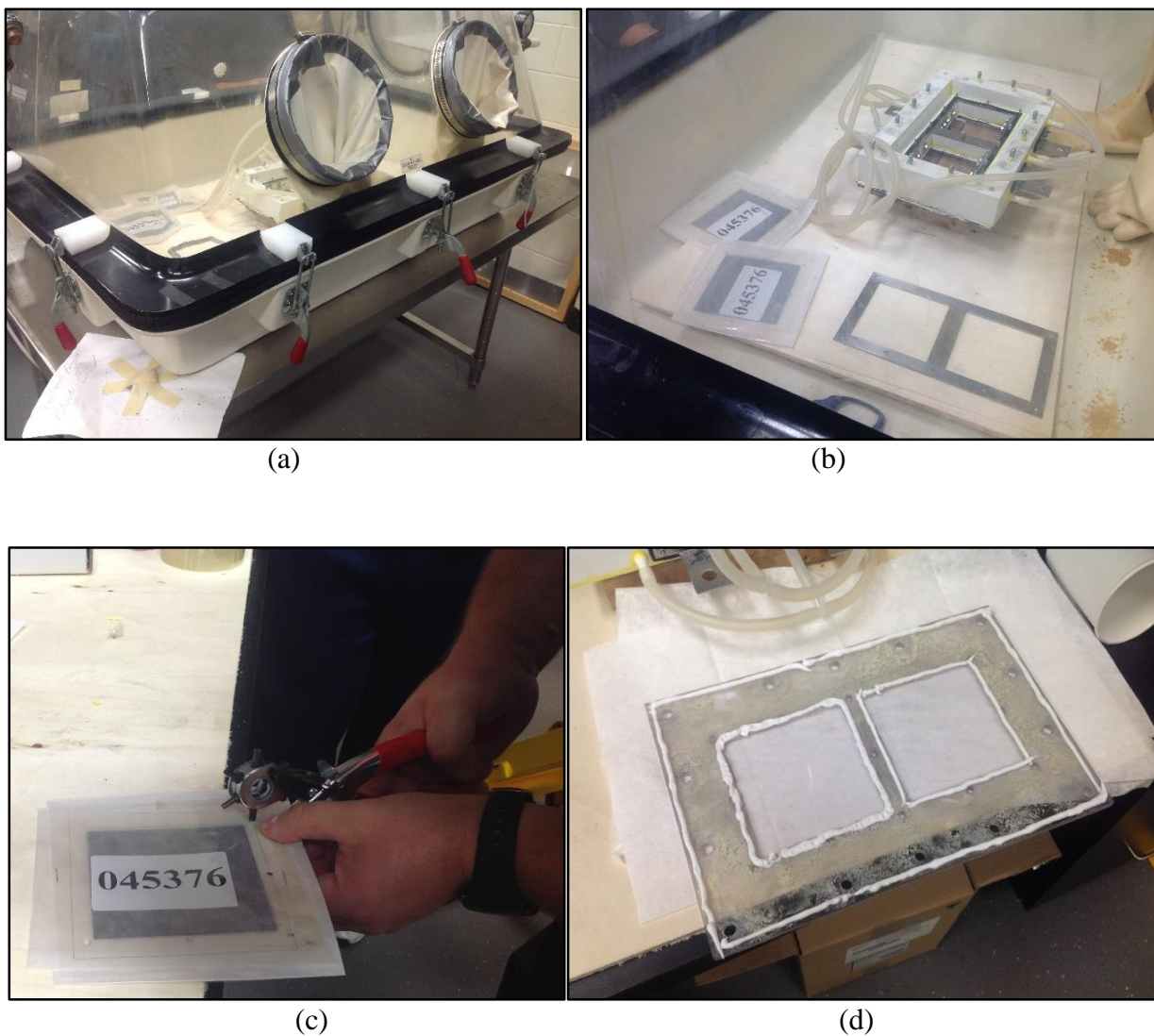
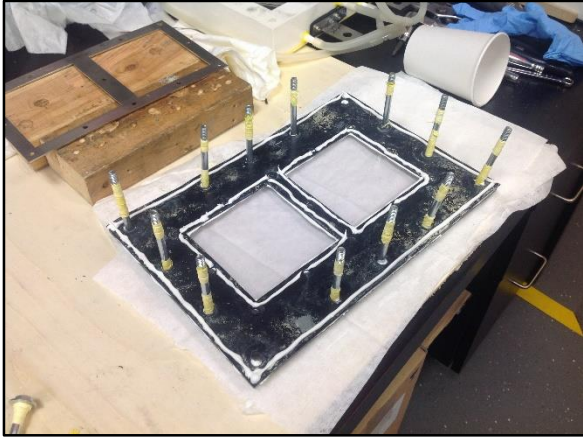
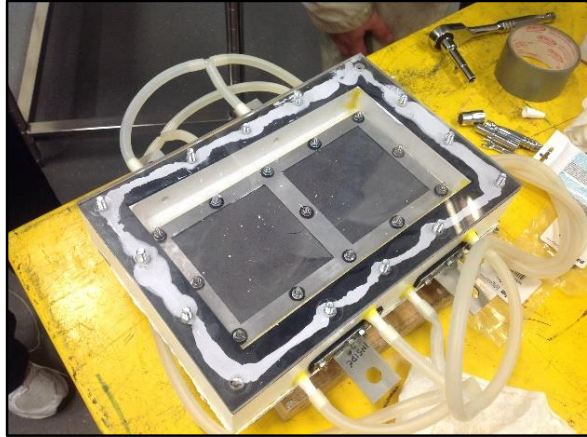


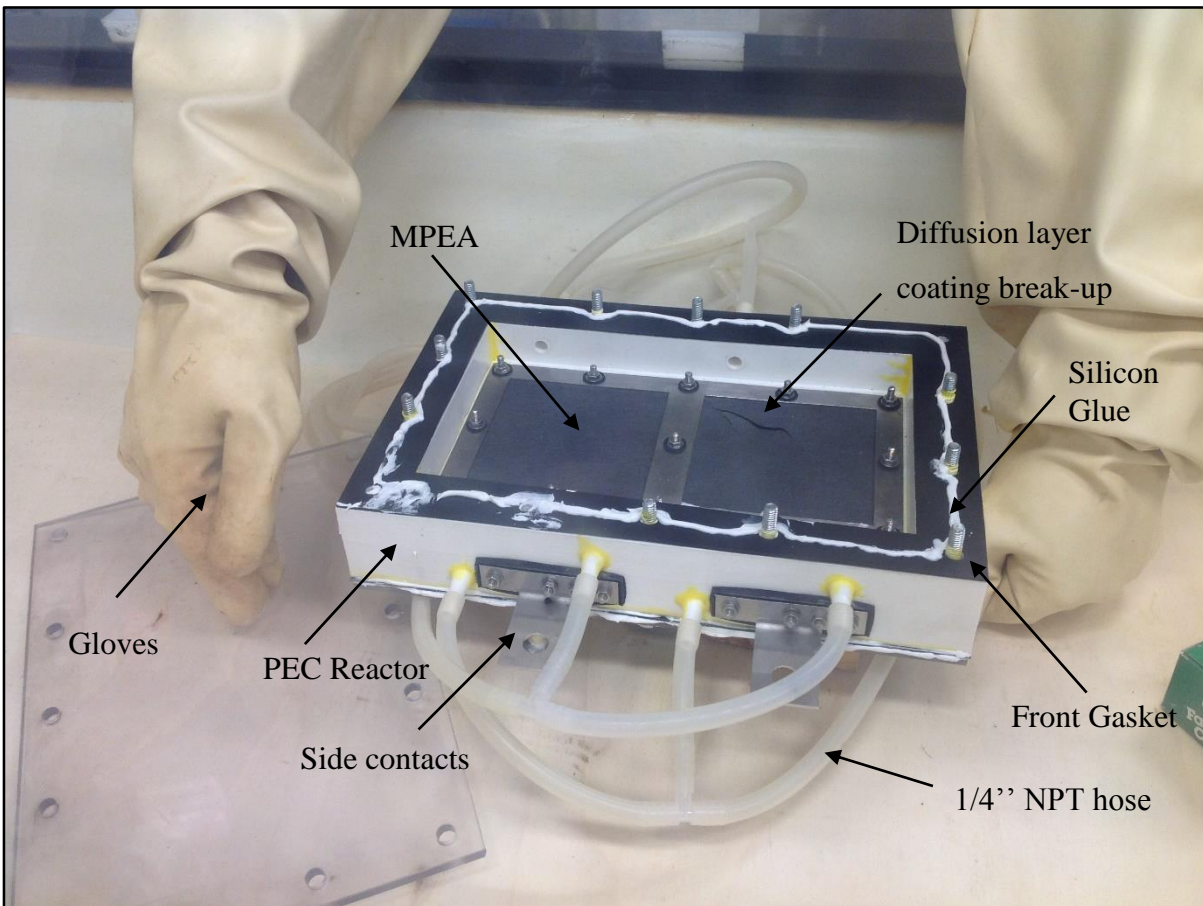
Figure 4.13: (a) Glove box, (b) inside the glove box before installation, (c) punching holes through the membrane using puncher, (d) applying silicon paste.



(a)



(b)



(c)

Figure 4.14: (a) Teflon covering the screws, (b) silicon glue applied to gaskets, (c) after installation of MPEA in an inert environment (glove box).

4.5 Instruments and Devices

4.5.1 Potentiostat

The cathode side of the reactor is exposed directly to photonic radiation which is assisted electrically by means of potentiostat (M). A potentiostat is a device which will apply a potential (or voltage) across a pair of electrodes and simultaneously measures the current which flows through a solution of an anolyte. Figure 4.15 shows the potentiostat used in this study. The potentiostat used for this research in the Gamry 3000 high-performance Potentiostat/Galvanostat/ZRA which has a maximum current of ± 3 A and a maximum voltage of ± 32 Volts. Another device which is used in conjunction with the Gamry potentiostat is the Gamry reference 30k booster. Attached to the Reference 3000, it boosts its current limit to ± 30 A with a compliance limits of +20 and -2.5 V allowing bandwidth EIS measurements up to 300 kHz.



Figure 4.15: (a) Reference 3000 high performance potentiostat, (b) reference 30k booster.

4.5.2 Peristaltic Pump

A multichannel peristaltic pump from Langer Instruments, BT100-2J, is used to validate, monitor, and control inlet and outlet flow rates of both anode and cathode compartments. BT100-2J can support flow rates between 0.002 – 380 mL/min and it allows each channel to have a different flow rate, making it possible to change each inlet/outlet flow rates independently. The

speed can be adjusted manually or automatically through external control. It also has the advantage of store the running parameters automatically which makes it fairly easy to operate. Figure 4.16b shows the peristaltic pump in operation.

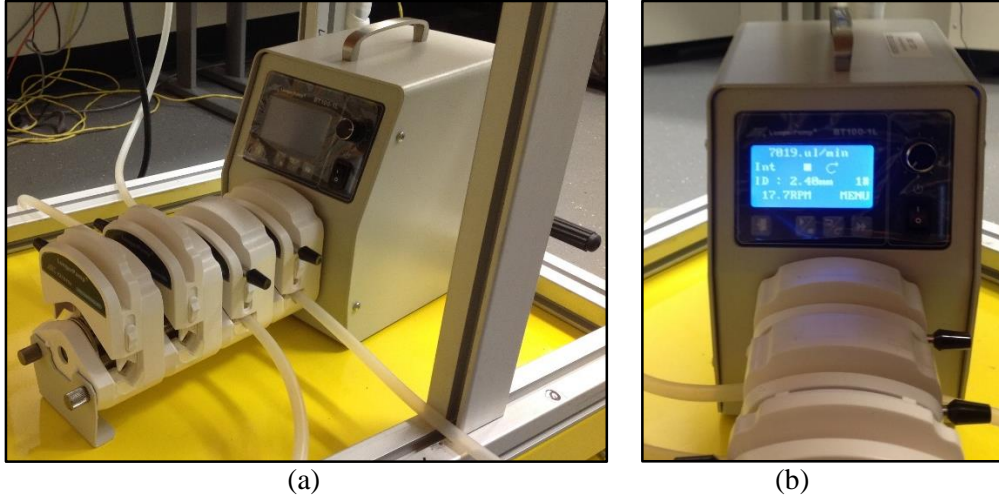


Figure 4.16: (a) Multichannel BT100-2J Peristaltic pump, (b) pump during system operation.

The pump can be externally controlled using the software provided by Langer instruments. This enables us to change the flow rates at merit and also store the data electronically.

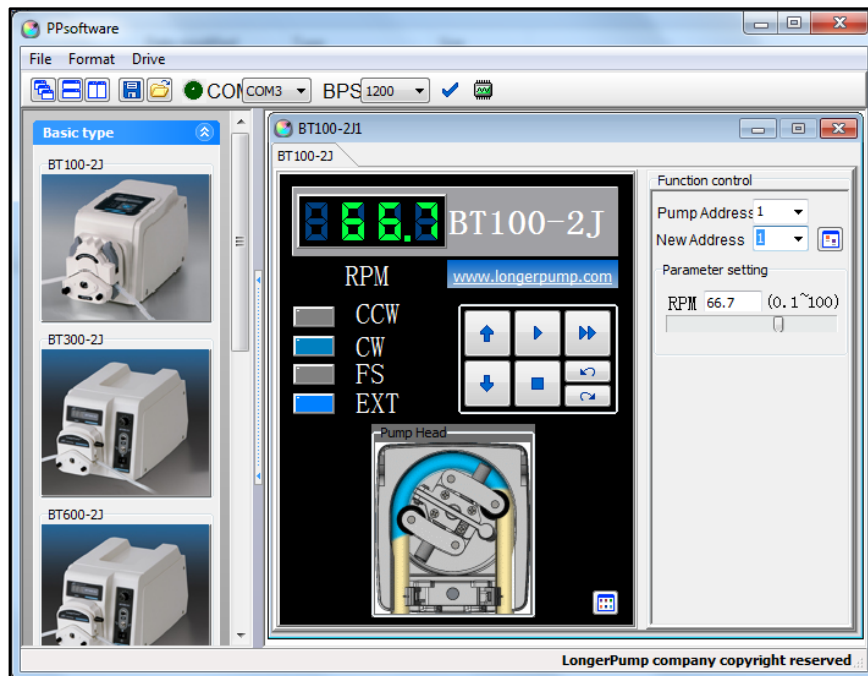
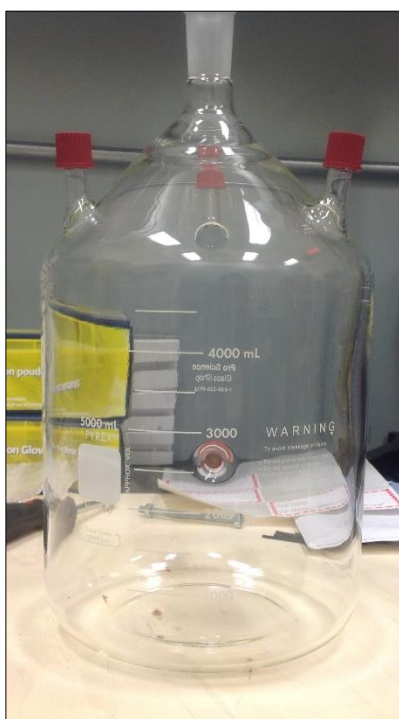


Figure 4.17: Peristaltic pump software for external control of flow rates.

4.5.3 Hot Plates, Reservoirs, and Magnetic Bars

Hot plates or electric heaters shown in Figure 4.18c are used in order to heat the two inlet streams, when the experiment is required to run at temperatures higher than the atmospheric temperature. The heaters are bought from Fisher Scientific™ Isotemp™ Digital Hotplates. In addition, a magnetic stir bar Figure 4.18b is used to keep the anolyte and catholyte homogenous. Figure 4.18a shows the reservoir or the electrolyte feed tank. This is custom made by ProScience GlassShop Division with a capacity of 6000 mL. These glass vessels have 24/40 center neck and 4 #14 Chemglass screw thread connectors with caps and sealing rings.



(a)



(b)



(c)

Figure 4.18: (a) Electrolyte feed/dump tank, (b) magnetic stirrer bar, (c) hot plate/electric heater.

4.6 Large Scale Conceptual Design

A block illustration is presented in Figure 4.19 which describes the large scale conceptual proposed system. The solar radiation harvested by the heliostat field (#1) is concentrated on the aperture of a hot mirror placed at the top of solar tower. The hot mirror, acting as spectral splitter consists of a selected dielectric coating deposited on-face of a borosilicate glass. The hot mirror

diverts (by reflection) the long wave spectrum portion (#4) of the concentrated radiation (#2) toward a volumetric solar receiver placed at the tower foot.

The transmitted radiation (#3) is dispersed and partially scattered in a large-size cavity receiver at the back of the hot mirror. Inside the cavity receiver are placed PV arrays and photo-reactors. Special coatings are applied on the PV arrays and photo-reactors. Owing to the coating, the PV arrays reflect back the photons of high energy spectrum while absorbing only in the range of 500–800 nm. The photo-reactors consist of cylindrical tubes in glass, covered with high band pass coating which reflects wavelengths longer than 500 nm.

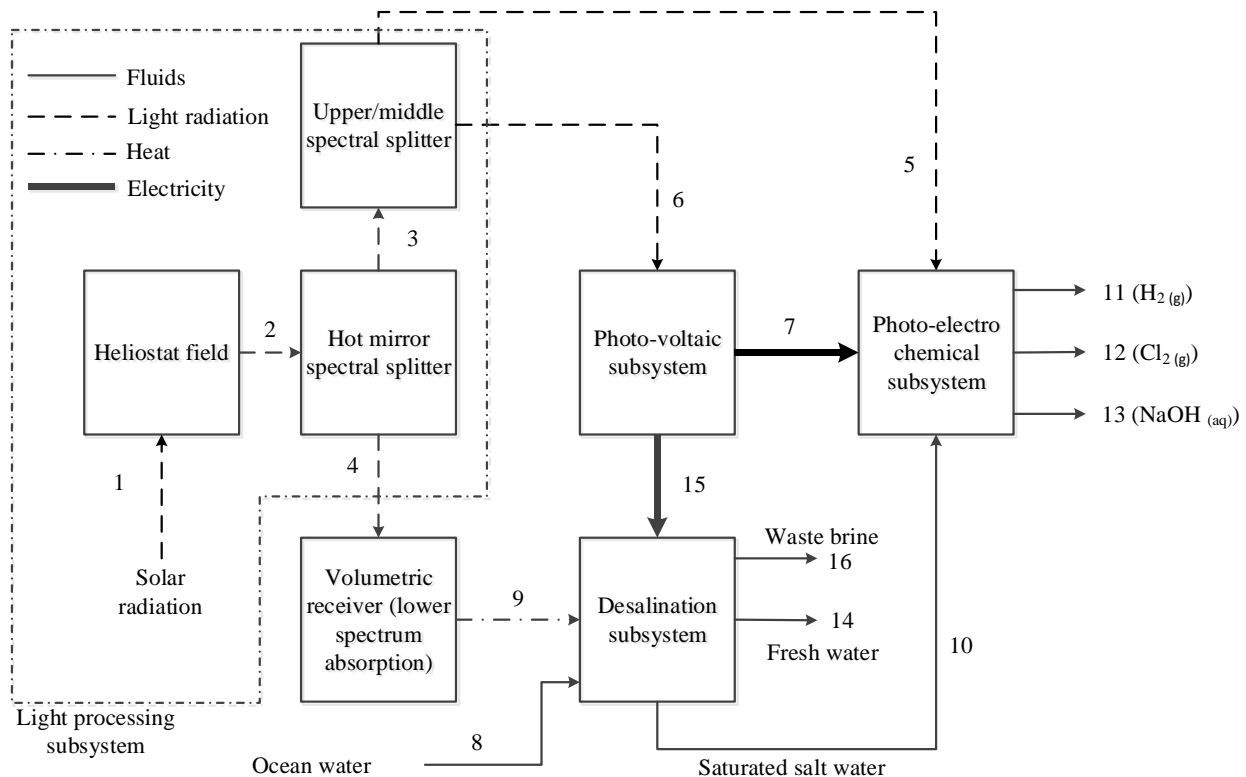


Figure 4.19: Conceptual block diagram of the integrated system for solar hydrogen production.

The optical arrangement inside the enclosure is such that it acts as a spectral splitter which divides the incoming light in (#3) into a high energy spectrum (#5) and middle spectrum (#6). Ocean/salty water (#8) is utilised by desalination system (#9) along with the volumetric solar receiver placed at the tower foot. The desalination process produces fresh water (#14) and saturated salt water as a by-product. The photoelectrochemical reactor system consumes high energy spectrum light (#5), electricity from PV arrays (#7) and saturated brine (#10). From these

aqueous wastes the photoelectrochemical system generates three valuable products: hydrogen (#11), chlorine (#12) and sodium hydroxide (#13).

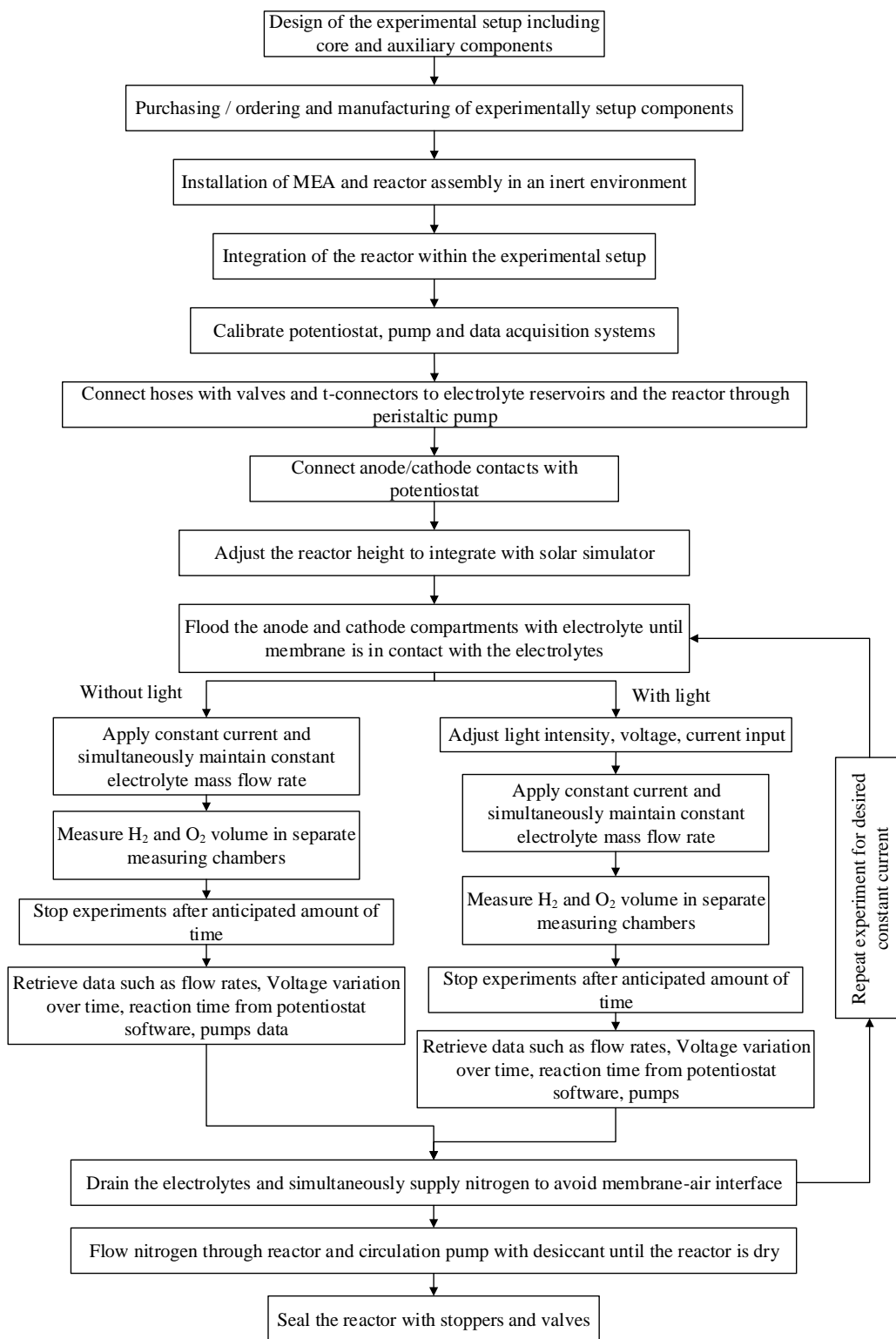


Figure 4.20: Experimental procedure overview.

Comprehensive energy and exergy analyses are accomplished for the suggested integrated system. This would provide substantial information about the performance, efficiency and pollutant emissions. Energy and exergy balance equations is written for all system components to eventually form a closed algebraic system. The solution of the system leads to the determination of the exergy destructions for each component, the exergy corresponding to produced hydrogen and the overall system efficiency. An overview of the experimental procedure is shown in Figure 4.20.

Chapter 5: Analyses

Comprehensive thermodynamic performance of the light-based hydrogen production system has been performed by conducting quantitative energy and exergy analyses including system efficiencies. Economic analysis is also performed based on the present worth method. In this chapter, the assumptions, procedure, balance equations, and efficiency definitions used to evaluate the proposed system's performance are described and explained. During the course of this study, the following assumptions are made:

- Ambient temperature (T_0) and pressure (P_0) are 25°C and 1 atm, respectively.
- Reactants and products are at reaction temperature and pressure in all chemical reactions.
- All processes occur at steady state.
- All processes proceed to completion.
- Potential and kinetic energy changes are neglected.
- Change in the control volume (reactor) is neglected.
- Hydrogen, oxygen, and chlorine gases are assumed to be ideal.
- Average field factor is 0.7 (Zamfirescu and Dincer, 2014).
- Spectral splitting system is devised similarly as in Zamfirescu and Dincer (2014) and includes exactly the same reflective coatings for the hot mirror, PV filter and PEC filter.
- Desalination subsystem is based on the Oceanside Plant California described in Sharqawy et al. (2011). This system has been previously analysed by Ghosh and Dincer (2014); the same exergy efficiency and process parameters are considered herein.
 - Water input salinity is $\omega_8 = 1.55\text{g/kg}$.
 - Exit brine salinity is $\omega_{16} = 6.11\text{g/kg}$.
 - Work input for the required by the desalination process 1.47 kJ/kg.
 - Fresh water product represents a fraction of 78% of the input brine.
 - Heat engine is incorporated into the desalination unit to utilise the power from the heat input provided by the thermal receiver in Figure 4.19 #9.
 - Temperature in #9 (Figure 4.19) is fixed at 200°C.
- Efficiency of thermal receiver is assumed to be 83% (Zamfirescu and Dincer, 2014).

- Based on the evaluation of the Reynolds number for the pipe duct which evaluates to 12924.65 and 8148.17 respectively, the following assumptions are made for ANSYS simulations:
 - Fully developed: A fully developed flow is when your boundary layer is fully developed, forming a D-shaped velocity profile with 0 velocity at the wall and streamline velocity at the centreline.
 - Fully Turbulent: High Reynolds number suggests that the flow is highly turbulent in the pipe.
 - Pressure driven flow: It is assumed that the outlets in the model are pressure outlets. i.e. the flow is due to the pressure difference in the outlets and inlets.
 - Gravity, $g = 9.81 \text{ m/s}^2$ in the negative y direction.
 - $k-\varepsilon$ model: Two-equation models account for the transport of the turbulence velocity scale and the length scale. They employ a transport equation for the length scale which allows the determination of the length scale distribution even in complex flow situations. Therefore, two-equation models are the simplest models that promise success for flows for which length scale cannot be prescribed empirically in an easy way.
- The work input from the magnetic stirrer is considered to be negligible.

A location is chosen where sufficient solar radiation exist; this is assumed to be 2 MWh/m² per year. The AM 1.5 solar spectrum is also assumed according to the ASTM (2013).The number of operational sunlight hours per year is taken 4000 h based on the study presented previously by Zamfirescu and Dincer (2014). Thus, the annual average direct and circumsolar irradiance is taken 500 W/m².

5.1 Thermodynamic Concepts

In this section, general mass, energy, entropy and exergy balance equations are written. In the forthcoming sections, these general equations are modified based on the assumptions and operating conditions of the proposed system. Consequently, based of these balanced equations, the rate of heat and work input/output, rate of entropy generation, rate of exergy destruction, and energy and exergy efficiencies are calculated.

5.1.1 Mass Balance Equation (MBE)

The conservation of mass in a control volume of any system can be described in its general form as follows:

$$\frac{dm_{cv}}{dt} = \sum \dot{m}_{in} - \sum \dot{m}_{out} \quad (5.1)$$

Here, m and \dot{m} represent the mass and mass flow rate whereas the subscripts ‘ cv ’, ‘ in ’ and ‘ out ’ indicate the control volume, inlet and outlet of the control volume, respectively. During steady state operation, Eq. (5.1) becomes:

$$\sum \dot{m}_{in} = \sum \dot{m}_{out} \quad (5.2)$$

5.1.2 Energy Balance Equation (EBE)

According to the first law of thermodynamics, the conservation of energy equation in a control volume can be expressed as follows:

$$E_2 - E_1 = \delta Q - \delta W \quad (5.3)$$

Here, Q and W are heat and work exchanges between the control volume and surroundings respectively. Subscripts 1 and 2 signify the initial and final states respectively. E represents the sum of all forms of energy i.e. kinetic, potential and/or flow energy that the system can possess at a given state. The general transient form energy balance equation can be written as follows:

$$\frac{dE_{cv}}{dt} = \dot{Q}_{cv} - \dot{W}_{cv} + \sum \dot{m}_{in} \left(h_{in} + \frac{V_{in}^2}{2} + gz_{in} \right) - \sum \dot{m}_{out} \left(h_{out} + \frac{V_{out}^2}{2} + gz_{out} \right) \quad (5.4)$$

Here, \dot{Q}_{cv} and \dot{W}_{cv} represent the rate of heat and power exchange within the control volume, respectively. The specific enthalpy, velocity, and elevation and gravitational acceleration are denoted by h , V , z , and g , respectively. As mentioned before, with the assumption that all reactions occur at steady state, the energy balance equation can now be written as follows:

$$\sum \dot{m}_{in} h_{in} + \dot{Q}_{cv} + \dot{W}_{cv} = \sum \dot{m}_{out} h_{out} \quad (5.5)$$

5.1.3 Entropy Balance Equation (EnBE)

In accordance with the second law of thermodynamics, the entropy balance equation can be written as follows:

$$\frac{ds_{cv}}{dt} = \sum \dot{m}_{in}s_{in} - \sum \dot{m}_{out}s_{out} + \sum \frac{\dot{Q}_{cv}}{T_0} + \dot{S}_{gen} \quad (5.6)$$

Here, s represents the specific entropy and \dot{S}_{gen} is the rate of entropy generation. The second law of thermodynamics states that entropy is not conserved unlike energy, instead entropy is generated due to irreversibilities in the system. Hence, the amount of entropy leaving the control volume surpasses the input entropy due to entropy generation associated with irreversibilities. As mentioned earlier, Eq. (5.6) with the steady state assumptions, the entropy balance equation (EnBE) can now be written as follows:

$$\sum \dot{m}_{in}s_{in} + \sum \frac{\dot{Q}_{cv}}{T_0} + \dot{S}_{gen} = \sum \dot{m}_{out}s_{out} \quad (5.7)$$

5.1.4 Exergy Balance Equation (ExBE)

Dincer and Rosen (2012) defined exergy as the maximum work that can be extracted from a system interacting with a reference environment. In addition to energy, investigating exergy allows us to accomplish a quantitative evaluation of imperfection sources and indicate potential process improvements from thermodynamics point of view, taking into account economic analysis also (Szargut et al., 1987). Exergy is also exempt from the conservation law alike entropy. Exergy balance is a statement of law of energy degradation as it describes the irreversible loss of exergy due to process irreversibilities. The exergy balance equation for system components in general can be written as follows:

$$\frac{dEx_{cv}}{dt} = \sum \dot{E}x_Q + \sum \dot{E}x_w + \sum \dot{E}x_{in} - \sum \dot{E}x_{out} - \dot{E}x_{dest} \quad (5.8)$$

Here, $\dot{E}x_Q$ denotes the exergy transfer due to heat, $\dot{E}x_w$ signifies exergy transfer rates associated with shaft work. The exergy transfer rates associated with the input and output flow streams are represented by $\dot{E}x_{in}$ and $\dot{E}x_{out}$. The system irreversibility is described by the rate of exergy destruction $\dot{E}x_{dest}$. With steady state assumptions, Eq. (5.8) can be written as follows:

$$\sum \dot{E}x_Q + \sum \dot{E}x_w + \sum \dot{m}_{in} ex_{in} = \sum \dot{m}_{out} ex_{out} + \dot{E}x_{dest} \quad (5.9)$$

Here, $\dot{E}x_Q$ is the exergy of heat transfer also described as the thermal exergy flow. During a chemical reaction in a control volume at a reaction temperature T , the maximum rate of conversion from thermal energy to useful work is described by $\dot{E}x_Q$. Mathematically, this can be written as follows:

$$\dot{E}x_Q = \dot{Q} \left(1 - \frac{T_0}{T} \right) \quad (5.10)$$

where $(1 - T_0/T)$ is dimensionless exergetic temperature also known as the Carnot efficiency working between the ambient temperature T_0 and the reaction temperature T . Note that the exergy transfer associated with shaft or boundary work is equal to work and the exergy transfer rate can be specified by the power or the work transfer rate. For a constant control volume, the exergy transfer rate associated with work can be expressed as follows:

$$\dot{E}x_w = \dot{W}_{cv} \quad (5.11)$$

As described in Kotas (1995), exergy of a flow of matter can be defined as the maximum amount of work obtainable when the flow is brought from its initial state to the reference state during a process of interaction with its environment. The exergy associated with the flow of a stream consists of physical exergy (ex^{ph}), chemical exergy (ex^{ch}), kinetic exergy (ex^{ke}) and potential exergy (ex^{pe}). Hence, the specific exergy of a stream can be written as follows:

$$ex_{flow} = ex^{ph} + ex^{ch} + ex^{ke} + ex^{pe} \quad (5.12)$$

If the changes in both kinetic and potential energies are negligible, Eq. (5.12) for a stream (i) can be written as follows:

$$ex_i = ex_i^{ph} + ex_i^{ch} = (h - h_0)_i - T_0(s - s_0)_i + ex_i^{ch} \quad (5.13)$$

Here, h and h_0 are specific enthalpies, and s and s_0 are the specific entropies at the defined and the reference environment states, respectively. The chemical exergy of an ideal gas mixture can be formulated by the following relation (Sato, 2004):

$$ex_{mix}^{ch} = \sum y_i ex_i^{ch} + RT_0 \sum y_i \ln y_i \quad (5.14)$$

Here, y_i is the mole fraction of the component/stream i in the gas mixture. The chemical exergy of a solid fuel is calculated based on the following formula (Kotas, 1995)

$$ex_{fuel}^{ch} = \left(LHV + (w \times h_{fg}) \right) \varphi_{dry} + 9.417s \quad (5.15)$$

Here, LHV is the net calorific value and w is the moisture content of the fuel. h_{fg} is the latent heat of water at T_0 and s denotes the mass fraction of sulphur in the fuel. φ_{dry} is the ratio of chemical exergy and can be defined in terms of dry organic substances contained in the fuel for an oxygen to carbon ratio between less than 0.667 as follows (Kotas, 1995)

$$\varphi_{dry} = 0.1882 \frac{h}{c} + 0.061 \frac{o}{c} + 0.404 \frac{n}{c} + 1.0437 \quad (5.16)$$

The letters denote the mass fraction of carbon (c), hydrogen (h), oxygen (o) and nitrogen (n) respectively. For an oxygen to carbon ratio between 0.667 and 2.67, φ can be written as follows (Kotas, 1995):

$$\varphi = \frac{0.1882 \frac{h}{c} - 0.2509 \left(1 + 0.7256 \frac{h}{c} \right) + 0.0404 \frac{n}{c} + 1.0437}{1 - 0.3035 \frac{o}{c}} \quad (5.17)$$

The following relation can be used for liquid fuels:

$$\varphi = 0.1882 \frac{h}{c} + 0.0432 \frac{o}{c} + 0.2169 \frac{s}{c} \left(1 - 2.0628 \frac{h}{c} \right) + 1.0401 \quad (5.18)$$

To calculate the chemical exergy of a fuel (Hydrogen in this case) the following simplification can be made in accordance with (Szargut and Styrylska, 1964):

$$\varphi = \frac{ex_{fuel}^{ch}}{LHV} \quad (5.19)$$

The rate of exergy destruction ($\dot{E}x_{dest}$) is proportional to the rate of entropy generation within the control volume and can be expressed as follows:

$$\dot{E}x_{dest} = T_0 \dot{S}_{gen} \quad (5.20)$$

5.2 Light Processing Subsystem

The evaluation of light exergy at any point along the optical path has to be carefully done in order to write the exergy balance equations for the light processing units. Here, the method developed in Zamfirescu and Dincer (2014) is used to determine the exergy of the light as a function of spectral irradiance.

Light carries entropy because at interaction with matter irreversibilities occur due mainly to the vibronic dissipation. The entropy carried by a light flux of spectral irradiance I_λ [W/m²nm] is given by

$$\dot{S} = \frac{1}{c_\lambda} \int_0^\infty \lambda I_\lambda d\lambda = \frac{1}{T_{rad}} \int_0^\infty I_\lambda d\lambda \quad (5.21)$$

where $c_\lambda = 0.00533016 \text{ mK}$ is the photonic constant derived by Chen et al. (2008) Following Zamfirescu and Dincer (2014), in Eq. (5.21), the temperature of the photonic radiation T_{rad} is introduced which can be explicitly expressed as follows

$$T_{rad} = c_\lambda \frac{\int_0^\infty I_\lambda d\lambda}{\int_0^\infty \lambda I_\lambda d\lambda} \quad (5.22)$$

Therefore, the exergy of light in function of spectral irradiance is given as follows:

$$\dot{E}x = \left(1 - \frac{T_0}{T_{rad}}\right) \dot{E} \text{ with } \dot{E} = A \int_0^\infty I_\lambda d\lambda \quad (5.23)$$

where T_0 is the reference temperature, \dot{E} is the energy rate associated with the light flux [W] and A is the incidence area of the light flux.

Based on the above considerations the energy and exergy balance equations for the light processing subsystem are formulated as given in Table 1. The total exergy destroyed consisting in the sum of energy due to energy losses (\dot{E}_l) and exergy destruction component at system interaction with the surroundings is accounted in the exergy balance equations. The energy rate at each particular state point is determined based on various assumptions and equations. With the help of the energy rates calculated, the entropy rates are then determined according to Eq. (5.21). Further, the temperature of the light radiation is determined according to Eq. (5.22). Once the

temperature of the radiation is found the Carnot factor is determined and further the exergy rate of the light flux as given by Eq. (5.23).

The energy and exergy balance equations for the heliostat field (process 1 – 2) is given as follows:

$$\dot{E}_1 = \dot{E}_2 + \dot{E}_{l,1-2} \quad (5.24)$$

$$\dot{E}x_1 = \dot{E}x_2 + \dot{E}x_{dest,1-2} \quad (5.25)$$

The energy and exergy balance equations for the hot mirror spectral splitter (process 2–3–4) is given follows:

$$\dot{E}_2 = \dot{E}_3 + \dot{E}_4 + \dot{E}_{l,2-3-4} \quad (5.26)$$

$$\dot{E}x_2 = \dot{E}x_3 + \dot{E}x_4 + \dot{E}x_{dest,2-3-4} \quad (5.27)$$

The energy and exergy balance equations for the upper/middle spectral splitter (process 3–5–6) is given as follows:

$$\dot{E}_3 = \dot{E}_5 + \dot{E}_6 + \dot{E}_{l,3-5-6} \quad (5.28)$$

$$\dot{E}x_3 = \dot{E}x_5 + \dot{E}x_6 + \dot{E}x_{dest,3-5-6} \quad (5.29)$$

Assuming a reference spectrum – for example AM 1.5 solar spectrum given in ASTM (2013), the temperature (T_1), energy rate (\dot{E}_1), entropy rate (\dot{S}_1) and exergy rate ($\dot{E}x_1$) of solar radiation entering the system can be written as follows:

$$T_1 = \frac{\dot{E}_1}{\dot{S}_1} \quad (5.30)$$

$$\dot{E}_1 = A_h \int_0^{\infty} I_{dni,\lambda} d\lambda \quad (5.31)$$

$$\dot{S}_1 = \int_0^{\infty} \frac{\dot{E}_{1,\lambda}}{T_\lambda} d\lambda \quad (5.32)$$

$$\dot{E}x_1 = \left(1 - \frac{T_0}{T_1}\right) \dot{E}_1 \quad (5.33)$$

where A_h denotes the total area of heliostats; $I_{dni,\lambda}$ represent the spectral irradiance of direct normal radiation. It is assumed that the heliostats track the sun.

As mentioned in Section 2.3, the majority of the incident radiation according get reflected according to its spectral reflectance $R_{\lambda,h}$. The reflectance of silver mirrors drops sharply in UV region. On the other hand, the reflectance of aluminum remains fairly high for all spectrum except a small drop in the region of 800–900 nm. Zamfirescu and Dincer (2014) give the values of extinction and refraction coefficients and reflectance for aluminum and silver which are considered as possible choices for our proposed system. Using the reflectance data from heliostat mirror ($R_{\lambda,h}$) we can obtain the entropy rate (\dot{S}_2) and the equivalent temperature of reflected radiation (T_2):

$$\dot{S}_2 = \int_0^{\infty} \frac{\dot{E}_{2,\lambda}}{T_\lambda} d\lambda \quad (5.34)$$

$$T_2 = \frac{\dot{E}_2}{\dot{S}_2} \quad (5.35)$$

The energy of incident radiation of the spectral splitter (#2 in Figure 4.19) will be smaller than \dot{E}_1 due to various types of losses which vary depending on the heliostat position in the field and on the sun angle. These losses can be collectively represented as into a compounded optical field loss factor defined by as follows

$$F_{field} = f_\theta f_s f_b f_{at} f_\gamma f_a \quad (5.36)$$

The factors on the right hand side of equation 5.16 represent the losses due to momentarily incident angle (θ) of the sun with respect to reflecting surfaces, shading of surfaces (s), partial blocking (b) or reflected light, atmospheric attenuation (at), optical aberration (γ) and light interception (a) by the spectral splitter, and the incident angle of concentrated radiation on the spectral splitter surface plane, respectively (Zamfirescu and Dincer, 2014).

The factor F_{field} is taken as an averaged one for all heliostats. This value can be calculated by comprehensive solar field modeling based on known heliostat positions, optical characteristics and known geographical location. Using the compounded factor for heliostat field losses, the energy and the exergy of the concentrated radiation beam at the entrance in solar splitter module atop of the tower can be calculated as follows:

$$\dot{E}_2 = F_{\text{field}} A_h \int_0^{\infty} R_{\lambda,h} I_{\text{dni},\lambda} d\lambda \quad (5.37)$$

where $R_{\lambda,h} \in (0,1)$ denote the spectral reflectance of heliostat mirrors.

$$\dot{E}x_2 = \left(1 - \frac{T_0}{T_2}\right) \dot{E}_2 \quad (5.38)$$

The entropy and temperature of radiation #4 reflected by the dielectric coating can be calculated based on the spectral reflectance $R_{\lambda,d}$

$$\dot{S}_4 = \int_0^{\infty} \frac{\dot{E}_{4,\lambda}}{T_\lambda} d\lambda \quad (5.39)$$

$$T_4 = \frac{\dot{E}_4}{\dot{S}_4} \quad (5.40)$$

There is also a radiation component which is reflected by the glass supporting the mirror. However, this radiation is neglected because it is logical to assume that this radiation is scattered and dissipated and will not intercept in #4 in Figure 4.19. The energy and exergy of the dielectric coating can therefore be written as follows:

$$\dot{E}_4 = \gamma \int_0^{\infty} \dot{E}_{4,\lambda} d\lambda \quad (5.41)$$

$$\dot{E}x_4 = \left(1 - \frac{T_0}{T_4}\right) \dot{E}_4 \quad (5.42)$$

Here, $\gamma \in (0,1)$ is the intercept factor of the secondary concentrator system (compound parabolic concentrator).

The transmitted UV/V light is attenuated by glass substrate which has an assumed spectral reflectance $R_{\lambda,g}$ (or transmittance $1 - R_{\lambda,g}$). Consequently, the entropy, temperature, energy, and exergy balance equations of radiation in #3 (Figure 4.19) are written as follows:

$$\dot{S}_3 = \int_0^{\infty} \frac{\dot{E}_{3,\lambda}}{T_\lambda} d\lambda = \frac{\dot{E}_3}{T_3} \quad (5.43)$$

$$T_3 = \frac{\dot{E}_3}{\dot{S}_3} \quad (5.44)$$

$$\dot{E}_3 = F_{\text{field}} A_h \int_0^{\infty} R_{\lambda,h} (1 - R_{\lambda,d}) (1 - R_{\lambda,g}) I_{\text{dni},\lambda} d\lambda \quad (5.45)$$

where $R_{\lambda,d}$ signifies the spectral reflectance of dielectric coating of the hot mirror. $R_{\lambda,g}$ signifies the spectral reflectance of hot mirror glass substrate.

$$\dot{E}x_3 = \left(1 - \frac{T_0}{T_3}\right) \dot{E}_3 \quad (5.46)$$

The transmitted and dispersed radiation from (#3 in Figure 4.19) enters the cavity receiver. Here the scale of the present application is a large, enclosed room at the top of the tower. Inside the cavity there are PV arrays and photocatalytic reactors on which the photonic radiation impacts. The PV arrays absorb and reflect radiation in accordance to the spectral reflectance $R_{\lambda,PV}$ of their coating. The selected coating is such that the photons with wavelength shorter than approx. 500 nm are reflected back in the cavity receiver. The photocatalytic reactors are coated such that they reflect photons with wavelength longer than approx. 500 nm. Hence, we can write the entropy and temperature for (#6 in Figure 4.19, the PV arrays absorbers) as follows:

$$\dot{S}_6 = \int_0^\infty \frac{\dot{E}_{6,\lambda}}{T_\lambda} d\lambda \quad (5.47)$$

$$T_6 = \frac{\dot{E}_6}{\dot{S}_6} \quad (5.48)$$

Likewise, the energy and exergy balance equations for the PV arrays can be written as

$$\dot{E}_6 = F_{\text{field}} A_h \int_0^\infty (1 - R_{\lambda,PV}) R_{\lambda,h} (1 - R_{\lambda,d}) (1 - R_{\lambda,g}) I_{\text{dni},\lambda} d\lambda \quad (5.49)$$

where $R_{\lambda,PEC}$, $R_{\lambda,PV}$ are spectral reflectances of PEC and PV, respectively.

The photocatalytic reactors absorb radiation in accordance to the spectral transmittance of the high-pass coating, which is given by $1 - R_{\lambda,cat}$. Therefore, the entropy and temperature equations can be written as follows:

$$\dot{S}_5 = \int_0^\infty \frac{\dot{E}_{5,\lambda}}{T_\lambda} d\lambda \quad (5.50)$$

$$\dot{T}_5 = \frac{\dot{E}_5}{\dot{S}_5} \quad (5.51)$$

Correspondingly, the energy and exergy balance equations for the photocatalytic reactor can be written as follows:

$$\dot{E}_5 = F_{\text{field}} A_h \int_0^{\infty} (1 - R_{\lambda, \text{PEC}}) R_{\lambda, \text{PV}} R_{\lambda, \text{h}} (1 - R_{\lambda, \text{d}}) (1 - R_{\lambda, \text{g}}) I_{\text{dni}, \lambda} d\lambda \quad (5.52)$$

$$\dot{E}x_5 = \left(1 - \frac{T_0}{T_5}\right) \dot{E}_5 \quad (5.53)$$

5.3 Volumetric Receiver

A compound parabolic concentrator is used to re-concentrate the infrared radiation reflected by the hot mirror on a volumetric receiver. Here, the light radiation is converted into high temperature heat. The temperature is chosen such that it serves the desalination subsystem. Denoted with T_9 (#9 in Figure 4.19) the temperature at which high temperature flux generated by the receiver is transferred to the desalination subsystem. Hence, the exergy rate in #9 (see Figure 4.19) is given as follows:

$$\dot{E}x_9 = \left(1 - \frac{T_0}{T_9}\right) \dot{Q}_9 \quad (5.54)$$

with $\dot{Q}_9 = \dot{E}_9$ being the energy rate in #9 (Figure 4.19) which is in form of a heat flux.

The subsequent energy and exergy balance equations for the volumetric receiver can be written as follows:

$$\dot{E}_4 = \dot{E}_9 + \dot{E}_{1,4-9} \quad (5.55)$$

$$\dot{E}x_4 = \dot{E}x_9 + \dot{E}x_{\text{dest},4-9} \quad (5.56)$$

5.4 Desalination Subsystem

The purpose of the desalination subsystem integrated within the solar hydrogen production plant is two-fold:

- To generate a concentrated NaCl solution for the photoelectrochemical chloralkali process which extracts three valuable chemicals from it (H₂, Cl₂, NaOH)
- To generate fresh water as an additional marketable by-product.

Figure 5.1 shows the desalination subsystem, which has two functional units, namely, the desalination unit (based on reverse osmosis) and the brine concentration unit (based essentially on thermal distillation).

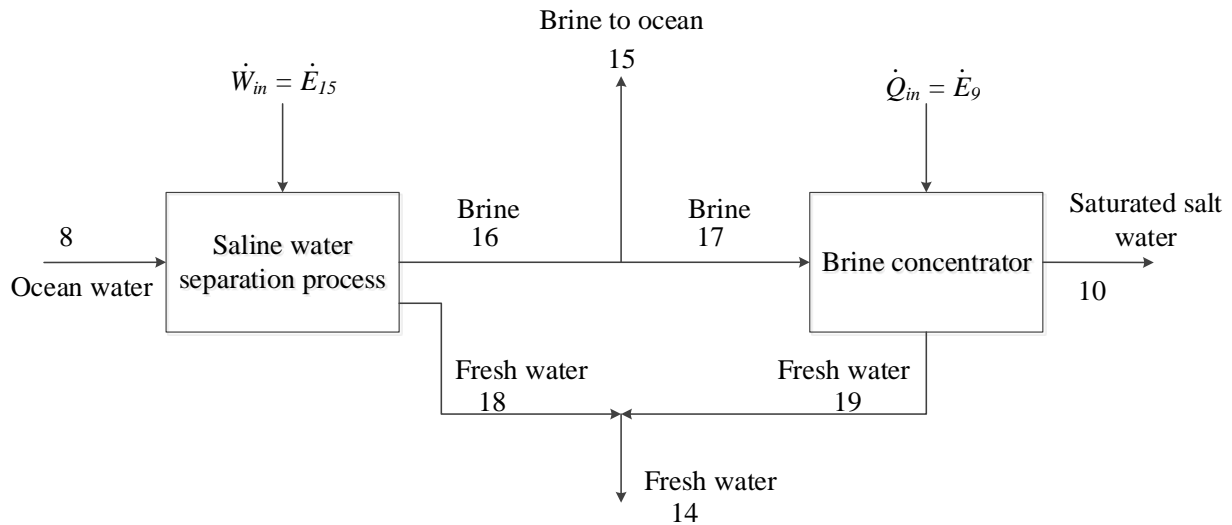


Figure 5.1: Process flow schematic for the desalination subsystem.

Ocean water assumed at atmospheric temperature and pressure with salinity of $\omega_8 = 1.55$ g/kg. The dead state salinity of sea water (needed for exergy calculations) is assumed to $\omega_0 = 35$ g/kg. The specific exergy is calculated as

$$ex = (h - h_0) - T_0(s - s_0) + \sum \omega(\mu - \mu^0) \quad (5.57)$$

where h , s , μ and ω are the specific enthalpy and entropy, chemical potential, and salinity (mass fraction), respectively.

The minimum work of separation for a desalination plant is the work of a reversible system. This can be calculated based on exergy balance equation shown below for the reverse osmosis desalination unit using in which exergy destruction is set to zero as explained and detailed by Sharqawy et al. (2011) and Ghosh and Dincer (2014).

The mass, energy, entropy and exergy balance equations for the reverse osmosis desalination unit can be written as follows:

$$\begin{aligned} \text{MBE:} \quad \dot{m}_8 &= \dot{m}_{16} + \dot{m}_{18}; \dot{m}_8 \omega_8 = \dot{m}_{16} \omega_{16} + \dot{m}_{18} \omega_{18} & (5.58) \\ \omega_{18} &\cong \omega_{19} \cong 0 \end{aligned}$$

$$\text{EBE:} \quad \dot{m}_8 h_8 + \dot{W}_{des} = \dot{m}_{16} h_{16} + \dot{m}_{18} h_{18} \quad (5.59)$$

$$\text{EnBE:} \quad \dot{m}_8 h_8 + \dot{S}_{gen,des} = \dot{m}_{16} s_{16} + \dot{m}_{18} s_{18} \quad (5.60)$$

$$\text{ExBE:} \quad \dot{m}_8 ex_8 + \dot{W}_{des} = \dot{m}_{16} ex_{16} + \dot{m}_{18} ex_{18} + \dot{E}x_{dest,des} \quad (5.61)$$

The concentrated brine coming out of the reverse osmosis desalination unit is further concentrated until saturated in the brine concentrator unit (Figure 5.1). The mass, energy, entropy and exergy balance equations for the salt concentration unit can be written as follows:

$$\begin{aligned} \text{MBE:} \quad \dot{m}_{17} &= \dot{m}_{10} + \dot{m}_{19}; \dot{m}_{16} = \dot{m}_{15} + \dot{m}_{17}; \dot{m}_{18} + \dot{m}_{19} = \dot{m}_{14} & (5.62) \\ \dot{m}_{17} \omega_{17} &= \dot{m}_{10} \omega_{10} + \dot{m}_{19} \omega_{19} \end{aligned}$$

$$\text{EBE:} \quad \dot{m}_{17} h_{17} + \dot{Q}_9 = \dot{m}_{10} h_{10} + \dot{m}_{19} h_{19} \quad (5.63)$$

$$\text{EnBE:} \quad \dot{m}_{17} s_{17} + \frac{\dot{Q}_9}{T_9} + \dot{S}_{g,conc} = \dot{m}_{10} s_{10} + \dot{m}_{19} s_{19} \quad (5.64)$$

$$\text{ExBE:} \quad \dot{m}_{17} ex_{17} + \dot{Q}_9 \left(1 - \frac{T_0}{T_9}\right) = \dot{m}_{10} ex_{10} + \dot{m}_{19} ex_{19} + \dot{E}x_{dest,conc} \quad (5.65)$$

The desalination unit is considered here based on a case study, as shown later in the Results and Discussion section. From this case study the exergy efficiency is determined and further the power required for the desalination unit $\dot{W}_{in} = \dot{E}_{15} = \dot{E}x_{15}$ is calculated as follows:

$$\dot{E}_{15} = \dot{E}x_{15} = \dot{W}_{in} = \frac{\dot{W}_{min}}{\eta_{ex,des}} \quad (5.66)$$

5.5 Photovoltaic Subsystem

This system comprises the PV-array and the power electronics. The PV-array operates under concentrated radiation of middle spectrum. Hence, the electric power generated by PV subsystem must be calculated based on the spectral response of the selected PV-cells. This response can be

determined with the help of cell performance parameters such as: open circuit voltage (V_{oc}), short circuit current density (J_{sc}), filling factor (FF), band gap energy (E_g), saturation current density (J_0), internal resistance (R_s), and spectral quantum efficiency (Φ_λ).

The energy and exergy produced by the PV-array under concentrated spectral radiation is equal to the maximum power generated. This is given as shown in McEvoy et al. (2003) by the following equation:

$$\dot{E}_{x7} = \dot{E}_7 = \dot{W}_{\max} = A_{PV} FF J_{sc} V_{oc} \quad (5.67)$$

where J_{ph} is the current density which is approximately equal with the photocurrent ($J_{sc} \cong J_{ph}$). The photocurrent depends on the spectral quantum efficiency Φ_λ and the spectral irradiance of the concentrated radiation according to the following equation:

$$J_{sc} \cong J_{ph} = \frac{e F_{field} A_h}{A_{PV} h c} \int_0^\infty \lambda \Phi_\lambda (1 - R_{\lambda,PV}) R_{\lambda,h} (1 - R_{\lambda,d}) (1 - R_{\lambda,g}) I_{dni,\lambda} d\lambda \quad (5.68)$$

The open circuit voltage is related to photocurrent according and to the exchange current density (J_0) to the following equation compiled from McEvoy et al. (2003):

$$v_{oc} = \frac{e V_{oc}}{kT} = \ln \left(1 + \frac{J_{ph}}{J_0} \right) \text{ with } J_0 \left[\frac{A}{m^2} \right] = 1.5E9 \exp \left(-\frac{E_g}{k T_{PV}} \right) \quad (5.69)$$

The filling factor is given by the following empirical correlation from McEvoy et al. (2003) namely:

$$FF = \frac{v_{oc} - \ln(v_{oc} + 0.72)}{V_{oc} + 1} \left(1 - \frac{R_s J_{sc}}{V_{oc}} \right) \quad (5.70)$$

5.6 Photoelectrochemical Subsystem

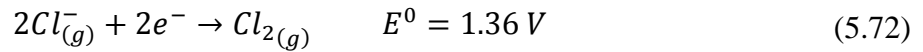
The photoelectrochemical subsystem consists of a photoelectrochemical cell where the chloralkali process is conducted and auxiliaries (anolyte and catholyte circulation system, pumps, NaOH concentration system etc.). According to Chlistunoff (2005) the membrane chloralkali technology is mature and no major improvement is foreseen except if new methods

are devised to depolarize the electrodes such that the net power consumed from the grid is reduced. A method of depolarizing the electrodes is proposed by a research group at University of Ontario Institute of Technology as described in Rabbani et al. (2014).

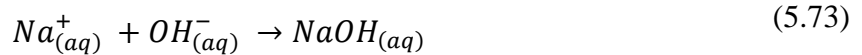
The photoelectrochemical cell is similar with a typical membrane-based electrochemical chloralkali process except that a photo-cathode is used by the PEC; in addition, the photocathode and the anode are attached to the membrane forming a so-called MPEA (membrane photoelectrode assembly). The cell reduces water at the photo-cathode according to the half reaction:



At the anode, chlorine is formed from saturated NaCl aqueous solution as follows:



Thus the total cell voltage (except the overpotentials) is $E^0 = 2.1877 V$ which is higher than 1.23 V for water electrolysis. However, the chlorine and NaOH by-products which are well marketable, justify the additional energy expense needed to operate the cell. The caustic soda forms in the catholyte can be written as follows:



Here, the sodium ions migrate from the anolyte, through the cation exchange membrane (NAFION®). The sodium ions form in the anolyte by NaCl dissociation is shown by the following reaction:



Figure 5.2 shows the process flow diagram for the PEC subsystem. As suggested by Chlistunoff (2005) the practical overvoltage of the membrane-based chloralkali electrochemical cell is 3.1 V at 0.4 A/cm²; thence, the cell overvoltage is of the order of 0.92 V. In the photoelectrochemical cell proposed herein semiconductors embedded in the photocathode materials which generate sufficient voltage to depolarize the electrodes significantly. We assume that the photocathode is electroplated with Cu₂O semiconductors. The band gap of this

semiconductor is 2.137 eV (580 nm). Once excited, the energy level of the electron drops to a level corresponding to the Fermi level of the platinum active centers which are deposited on the photocathode surface to catalyse the half-reaction (11). The molar rate of produced hydrogen depends on the photon rate in #5 (Figure 5.1) and the photocatalytic quantum efficiency, Φ_{PEC} and is given as follows:

$$\dot{n}_{H_2} = \frac{\Phi_{PEC} F_{field} A_h}{2N_A h c} \int_{580 \text{ nm}}^{\infty} (1 - R_{\lambda,PEC}) R_{\lambda,PV} R_{\lambda,h} (1 - R_{\lambda,d}) (1 - R_{\lambda,g}) \lambda I_{dni,\lambda} d\lambda \quad (5.75)$$

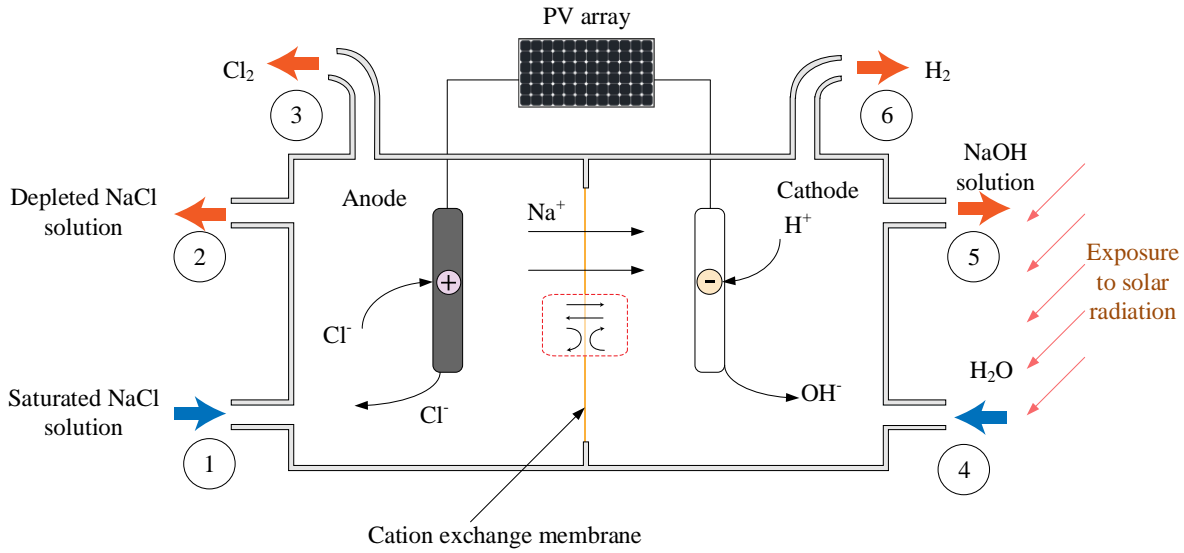


Figure 5.2: Schematic of the light-based hybrid photoelectrochemical reactor.

Assume that 50% of the voltage required by the cell is supplied directly by light while the rest is applied voltage to the electrodes. Thence, for a practical cell the applied voltage can be assumed to $V_{PEC} = 1.55 \text{ V}$. The required power from the PV-subsystem is therefore:

$$\dot{E}_7 = \dot{E}x_7 = \dot{W}_{PEC} = 2\dot{n}_{H_2} F V_{PEC} \quad (5.76)$$

5.6.1 Mass Balance Equation

The steady state mass balance equation (MBE) for the proposed light-based PEC reactor (Figure 5.3) can be written as follows:

$$\dot{m}_1 + \dot{m}_4 = \dot{m}_2 + \dot{m}_3 + \dot{m}_5 + \dot{m}_6 \quad (5.77)$$

where \dot{m}_1 signifies the mass flow rate in (kg/s) of inlet brine (aqueous NaCl solution) entering the reactor cell, \dot{m}_2 represents mass flow rate in (kg/s) of outlet brine (depleted NaCl solution). Consequently, \dot{m}_4 represents the mass flow rate of water in (kg/s) entering the cathode compartment, \dot{m}_5 denotes the mass flow rate of sodium hydroxide (NaOH) solution. \dot{m}_3 and \dot{m}_6 represents the mass flow rate in (kg/s) of chlorine gas and hydrogen gas leaving the reactor cell respectively.

The mass flow rate of salt (NaCl) entering the anode compartment is given as follows:

$$\dot{m}_{s1} = \dot{m}_1 x_{s1} \quad (5.78)$$

Here, x_{s1} is the mass fraction of NaCl in stream 1. The mass flow rate of water entering the anode section can be written as follows:

$$\dot{m}_{w1} = \dot{m}_1 - \dot{m}_1 x_{s1} = \dot{m}_1 (1 - x_{s1}) \quad (5.79)$$

Similarly, the mass flow rate of aqueous solution of NaCl leaving the anode section of the cell as can be written as follows:

$$\dot{m}_{s2} = \dot{m}_2 x_{s2} \quad (5.80)$$

Here, x_{s2} is the mass fraction of NaCl in stream 2. The mass flow rate of water leaving the anode section can be written as follows:

$$\dot{m}_{w2} = \dot{m}_2 - \dot{m}_2 x_{s2} = \dot{m}_2 (1 - x_{s2}) \quad (5.81)$$

With Eqs. (5.78) - (5.81), the NaCl consumption in the anode compartment can be calculated as follows:

$$\dot{m}_{s,con} = \dot{m}_{s1} - \dot{m}_{s2} = \dot{m}_1 x_{s1} - \dot{m}_2 x_{s2} \quad (5.82)$$

$$\dot{n}_{s,con} = \frac{\dot{m}_{s1} - \dot{m}_{s2}}{58.44} = \frac{\dot{m}_1 x_{s1} - \dot{m}_2 x_{s2}}{58.44} \quad (5.83)$$

Here, $\dot{m}_{s,con}$ and $\dot{n}_{s,con}$ are the mass and molar composition rates of NaCl in the anode section in kg/s and kmol/s, respectively. Note that the molar weight of NaCl is taken as 58.44 kg/kmol.

Since the system is assumed to be operating at steady state, the following statements can be taken into account while conducting mass balance calculations:

- The chlorine gas is not accumulated in the system.
- The sodium ions are not accumulated in the system.
- The water in streams 1 and 2 are not electrolysed.

With the above listed assumptions, we can write the molar (\dot{n}_3) and mass (\dot{m}_3) flow rates in kmol/s and kg/s for chlorine gas leaving the anode section of the reactor (stream 3) as follows:

$$\dot{n}_3 = \frac{\dot{n}_{s,con}}{2} = \frac{\dot{m}_{s1} - \dot{m}_{s2}}{116.88} = \frac{\dot{m}_1 x_{s1} - \dot{m}_2 x_{s2}}{116.88} \quad (5.84)$$

$$\dot{m}_3 = MW_{Cl_2} \times \dot{n}_3 = 35.45 \times \dot{n}_{s,con} = \frac{\dot{m}_{s1} - \dot{m}_{s2}}{1.64} = \frac{\dot{m}_1 x_{s1} - \dot{m}_2 x_{s2}}{1.64} \quad (5.85)$$

Note that the molecular weight of Cl_2 is taken as 70.91 kg/kmol. The sodium ions from the consumed salt leave the system only at stream 5. The molecular weight of NaOH is taken to be 40 kg/kmol. x_{s2} represents the mass fraction of NaOH in stream 5 leaving the cathode section. Hence we can write the molar (\dot{n}_5) and mass (\dot{m}_5) flow rates in kmol/s and kg/s for NaOH leaving the anode section of the reactor (stream 5) as follows:

$$\dot{n}_{NaOH} = \frac{\dot{m}_{NaOH}}{40} = \frac{x_{s5} \dot{m}_5}{40} = \dot{n}_{s,con} = \frac{\dot{m}_1 x_{s1} - \dot{m}_2 x_{s2}}{58.44} \quad (5.86)$$

$$\dot{m}_5 = \frac{\dot{m}_1 x_{s1} - \dot{m}_2 x_{s2}}{1.64} \quad (5.87)$$

With the third assumption taken into consideration, during steady state operation, it is safe to say that the amount of water entering the anode section in stream 1 will be equal to the one leaving the anode section at stream 2. Hence:

$$\dot{m}_{w1} = \dot{m}_{w2} = \dot{m}_1 - \dot{m}_1 x_{s1} = \dot{m}_1 (1 - x_{s1}) \quad (5.88)$$

$$\dot{m}_2 = \frac{\dot{m}_1 (1 - x_{s1})}{1 - x_{s2}} \quad (5.89)$$

From the overall reaction stoichiometry i.e. $NaCl + 2H_2O \rightarrow Cl_2 + H_2 + 2NaOH$, it is clear that the rate of formation of Cl_2 and H_2 are equal. Hence, using the molecular weight of H_2 as 2.02 kg/kmol, we can write the following:

$$\dot{n}_6 = \frac{\dot{m}_1 x_{s1} - \dot{m}_2 x_{s2}}{116.88} \quad (5.90)$$

$$\dot{m}_2 = \frac{\dot{m}_1 x_{s1} - \dot{m}_2 x_{s2}}{57.86} \quad (5.91)$$

5.6.2 Energy Balance Equation

The energy balance equation for the proposed light-based PEC reactor can be written as follows:

$$\dot{m}_1 h_1 + \dot{m}_4 h_4 + \dot{W}_{in} + \dot{Q}_{in} = \dot{m}_2 h_2 + \dot{m}_3 h_3 + \dot{m}_5 h_5 + \dot{m}_6 h_6 \quad (5.92)$$

Here h_{1-6} represents the specific enthalpies of the associated streams. \dot{W}_{in} corresponds to the total work input to the system. \dot{Q}_{in} corresponds to the heat input required to keep the reaction above room temperature. Note that this is not always needed and this value will be zero when the reactions occur at room temperature. The work input is electricity for electrolysis process. On the contrary, the work input is solar energy for photoelectrolysis and photoelectrochemical processes. These can be represented by the following equations:

Electrolysis process:
$$\dot{W}_{in} = \dot{W}_{elec} = Vi \quad (5.93)$$

Photoelectrolysis process:
$$\dot{W}_{in} = \eta_{PV} I A_{PV} \quad (5.94)$$

Photoelectrochemical process:
$$\dot{W}_{in} = \eta_{PV} (1 - \alpha) I A_{PV} + \alpha I A_{PC} \quad (5.95)$$

Here, V is in Volts (V), i is current in Amps (A), η_{PV} and A_{PV} are the efficiency and area of the PV panels, respectively. I is the light intensity per square metre of heliostat area, A_{PC} is the area of photocathode, and α is the portion of solar light spectrum used by photocathode for photocatalytic hydrogen production.

5.6.3 Voltage Balance Equation

The minimum required input work is equal to the change in Gibbs free energy for a constant temperature and pressure electrochemical process. As suggested by Ulleberg (2003), according

to Faraday's law, the voltage required for a reversible electrochemical process can be expressed as follows:

$$V_{rev} = \frac{\Delta G(T)}{n_e F} \quad (5.96)$$

Here, n_e is the number of electrons transferred per electrolyzed molecule and F is Faraday's constant which is equal to 96,485.3415 s-A/mol. Note that due to the irreversibilities in the system the required voltage V is always larger than the reversible voltage V_{rev} . Electrochemical modelling is used as studied by Chandran and Chin (1986) to find the required potential by taking into account the decomposition voltage and ohmic losses across different components of the reactor. For the system shown in Figure 5.2, the overall voltage balance across the reactor can be written as

$$V = E^\circ + V_A + V_{sol,a} + V_{CEM} + V_{sol,c} + V_C \quad (5.97)$$

Here, E° represents the open circuit cell voltage also known as decomposition voltage. V_A symbolises the voltage drop across the anode electrode, $V_{sol,a}$ signifies the voltage drop across anolyte solution (brine solution), V_{CEM} represents the voltage drop across the cation exchange membrane, $V_{sol,c}$ denotes the voltage drop across catholyte solution (i.e. voltage drop in NaOH solution) and V_C represents the voltage drop across the cathode. In anode compartment, the chlorine ion is oxidised into chlorine gas.

According to Chandran and Chin (1986), applying Nernst equation to the anode reaction: $2Cl^- \rightarrow Cl_2 + 2e^-$ gives the following:

$$E^\circ_A = E^\circ_{Cl^-/Cl_2} + \frac{RT}{nF} \ln \left(\frac{P_{Cl_2}}{(\gamma_{Cl^-})^2} \right) \quad (5.98)$$

Here, R is the gas constant. T represents the reaction temperature in K, n represents the number of electrons used to oxidize chlorine ion. P_{Cl_2} and γ_{Cl^-} are the partial pressure of chlorine gas and activity coefficient of chlorine ion, respectively. $E^\circ_{Cl^-/Cl_2}$ is the standard electrode potential of chlorine (V).

Consequently, applying Nernst equation to the cathode reaction $2H_2O + 2e^- \rightarrow H_2 + OH^-$, we get:

$$E^{\circ}_C = E^{\circ}_{H_2O/H_2+OH^-} + 2.303 \frac{RT}{nF} \ln \left(\frac{P_{H_2}}{(\gamma_{OH^-})^2} \right) \quad (5.99)$$

Here, n represents the number of electrons used to oxidize hydroxyl ion (in this case, $n = 2$). P_{H_2} and γ_{OH^-} represent the partial pressure of hydrogen gas and activity coefficient of hydroxyl ion, respectively. $E^{\circ}_{H_2O/H_2+OH^-}$ is the standard electrode potential of hydrogen, typically established as 0.8280 V.

As suggested by Chandran and Chin (1986) applying the Nernst equation on the overall reaction $2H_2O + 2NaCl \rightarrow H_2 + Cl_2 + 2NaOH$, we get the following:

$$E^{\circ}_{overall} = -2.18 + 0.0004272T + \frac{8.314 T \ln \beta}{96500} \quad (5.100)$$

Here, β is dependent upon the partial pressures of hydrogen and chlorine in the gas phase and the activity coefficients of sodium chloride and sodium hydroxide. The value of β can be written as

$$\beta = \frac{\gamma_{NaCl} \sqrt{P_{Cl_2}} \sqrt{P_{H_2}}}{\gamma_{NaOH}} \quad (5.101)$$

where γ_{NaCl} denotes the density of activity coefficient of sodium chloride and γ_{NaOH} denotes the activity coefficient of sodium hydroxide. The activity coefficient of sodium chloride (γ_{NaCl}) depends on its molar concentration, M (mol/L), which can be evaluated as (Chandran and Chin, 1986):

$$\gamma_{NaCl} = 0.63 \exp(0.028 M_{NaCl}) \quad 1.2 \leq M_{NaCl} < 2 \quad (5.102)$$

$$\gamma_{NaCl} = 0.575 \exp(0.07 M_{NaCl}) \quad 2 \leq M_{NaCl} < 3.5 \quad (5.103)$$

$$\gamma_{NaCl} = 0.5 \exp(0.112 M_{NaCl}) \quad 3.5 \leq M_{NaCl} < 6 \quad (5.104)$$

The activity coefficient of sodium hydroxide (γ_{NaOH}) depends on its molar concentration, M (mol/L), which is evaluated as (Chandran and Chin, 1986):

$$\log \gamma_{NaOH} = -\frac{U\sqrt{M_{NaOH}}}{1 + \sqrt{2} M_{NaOH}} + B M_{NaOH} + C M_{NaOH}^2 + D M_{NaOH}^3 + E M_{NaOH}^4 \quad M_{NaOH} < 12 \quad (5.105)$$

$$B = 0.0065 + 0.0016 T - 1.8 \times 10^{-5} T^2 \quad (5.106)$$

$$C = 0.014 - 0.0005 T + 5.6 \times 10^{-6} T^2 \quad (5.107)$$

$$D = 0.0006 + 5 \times 10^{-5} T - 6.48 \times 10^{-7} T^2 \quad (5.108)$$

$$E = 5.96 \times 10^{-6} - 1.81 \times 10^{-6} T + 2.4 \times 10^{-8} T^2 \quad (5.109)$$

$$U = 0.00087 T + 0.486 \quad 25^\circ\text{C} \leq T \leq 40^\circ\text{C} \quad (5.110)$$

$$U = 0.00144 T + 0.46 \quad 40^\circ\text{C} \leq T \leq 100^\circ\text{C} \quad (5.111)$$

$$\log \gamma_{NaOH} = a + b M_{NaOH} + c M_{NaOH}^2 \quad M_{NaOH} \geq 12 \quad (5.112)$$

$$a = -0.327 + 0.0031 T - 3.29 \times 10^{-5} T^2 \quad (5.113)$$

$$b = 0.0988 - 0.00059 T \quad (5.114)$$

$$c = -2.14 \times 10^{-6} - 3.93 \times 10^{-7} T + 0.53 \times 10^{-8} T^2 \quad (5.115)$$

The voltage drop across the anode is calculated as

$$V_A = c_A \log \left(\frac{i}{i_{0,a}} \right) \quad (5.116)$$

Here, c_A is a constant which is determined experimentally. $i_{0,a}$ signifies the exchange current density. Both c_A and $i_{0,a}$ are dependent upon the nature of the reaction (in the present study, this would be the chlorine evolution reaction, along with the operating conditions and electrode material). $i_{0,a}$ also depends on the anode material and temperature (i.e. for graphite electrode at 90°C , $i_0 = 0.0125$). For a dimensionally stable anode, the voltage drop for the chlorine evolution reaction can be calculated as

$$V_A = 0.0277 \log \left(\frac{i}{i_0} \right) \quad (5.117)$$

The voltage drop across the anolyte solution can be determined as follows:

$$V_{sol,a} = i \times \frac{d_{Am}}{K_{NaCl}} \quad (5.118)$$

Here, i represents the current density, d_{Am} is the distance between the anode and cation exchange membrane, K_{NaCl} represents the electrical conductivity of the brine. The electric conductivity of brine is a function of both concentration and operating temperature. This can be estimated as

$$K_{NaCl} = (1.1 - (0.33\sqrt{\Omega_{NaCl}})(\lambda_{NaCl}\Omega_{NaCl})) \quad (5.119)$$

Here, λ_{NaCl} is a temperature dependent variable and Ω_{NaCl} is a concentration and density dependent variable. These are defined as follows:

$$\lambda_{NaCl} = 5.67 + 0.229T \quad (5.120)$$

$$\Omega_{NaCl} = \frac{M_{NaCl} \times \rho_{NaCl}}{1000 + (58.5 M_{NaCl})} \quad (5.121)$$

Here, ρ_{NaCl} denotes the density of the brine solution (kg/m³) which depends on temperature and solution concentration and can be calculated from:

$$\rho_{NaCl} = A + B T + C T^2 + D T^3 + E T^4 \quad 0^\circ\text{C} \leq T \leq 300^\circ\text{C} \quad (5.122)$$

$$A = (1.001 + 0.7666x - 0.0149x^2 + 0.2663x^3 + 0.8845x^4) \quad (5.123)$$

$$B = (-0.0214 - 3.496x + 10.02x^2 - 6.56x^3 - 31.37x^4) \quad (5.124)$$

$$C = (-5.263 + 39.87x - 176.2x^2 + 363.5x^3 - 7.784x^4) \times 10^{-3} \quad (5.125)$$

$$D = (15.42 - 167x + 980.7x^2 - 2573x^3 + 876.6x^4) \times 10^{-6} \quad (5.126)$$

$$E = (-0.0276 + 0.2978x - 2.017x^2 + 6.345x^3 - 3.914x^4) \times 10^{-6} \quad (5.127)$$

where x is the solution concentration (kg salt/kg solution).

The voltage drop across the cation exchange membrane is given as follows:

$$V_{CEM} = \frac{i \times \sigma_{CEM}}{K_{CEM}} \quad (5.128)$$

Here, i is the current density, σ_{CEM} is the membrane thickness and K_{CEM} denotes the electrical conductivity of the membrane. Electrical conductivity depends on a lot of factors such as the chemical structure of the membrane, ionic form, operating temperature, pH of the fluids with which membrane is in contact with, and the permeability of the membrane. This value is generally estimated and provided by the manufacturer. The voltage drop across the catholyte solution, $V_{sol,c}$ can be determined as follows:

$$V_{sol,c} = \frac{i \times d_{CM}}{K_{NaOH}} \quad (5.129)$$

Here, d_{CM} is the distance between the cathode and the cation exchange membrane, K_{NaOH} represents the electrical conductivity of sodium hydroxide. K_{NaOH} is a function of its concentration, operating temperature and density which is estimated as

$$K_{NaOH} = K_{NaOH,100^\circ C} \left(\frac{T}{373} \right)^s \exp \left(-\frac{E^*}{R} \left(\frac{1}{T} - \frac{1}{373} \right) \right) \quad (5.130)$$

$$\frac{E^*}{R} = 4456.5 + ((\Omega_{NaOH} - 2)(5109.5 - 4456.5)) \quad 2 \leq \Omega_{NaOH} < 3 \quad (5.131)$$

$$\frac{E^*}{R} = 5409.6 + ((\Omega_{NaOH} - 3)(4706.5 - 5109.8)) \quad 3 \leq \Omega_{NaOH} < 4 \quad (5.132)$$

$$\frac{E^*}{R} = 535.2\Omega_{NaOH} + 2617.8 \quad 4 \leq \Omega_{NaOH} < 7 \quad (5.133)$$

$$\frac{E^*}{R} = 967.5\Omega_{NaOH} + 548.2 \quad 7 \leq \Omega_{NaOH} < 16 \quad (5.134)$$

$$s = -9.6 + ((\Omega_{NaOH} - 2)(11.3 - 9.9)) \quad 2 \leq \Omega_{NaOH} < 3 \quad (5.135)$$

$$s = -11.3 + ((\Omega_{NaOH} - 3)(11.3 - 10)) \quad 3 \leq \Omega_{NaOH} < 4 \quad (5.136)$$

$$s = -1.06\Omega_{NaOH} - 5.8 \quad 4 \leq \Omega_{NaOH} < 7 \quad (5.137)$$

$$s = -2.44\Omega_{NaOH} + 5.3 \quad 7 \leq \Omega_{NaOH} < 16 \quad (5.138)$$

where $K_{NaOH,100^\circ C}$ represents the electrical conductivity of the aqueous sodium hydroxide at $100^\circ C$, it is depends on the concentration of the sodium hydroxide in the aqueous solution which can be estimated as

$$K_{NaOH,100^\circ C} = 2.6 + 40.9 \Omega_{NaOH} - 5.03 \Omega_{NaOH}^2 + 0.13 \Omega_{NaOH}^3 \quad 2 \leq \Omega_{NaOH} < 7 \quad (5.139)$$

$$K_{NaOH,100^\circ C} = 140.9 \quad 7 \leq \Omega_{NaOH} < 9 \quad (5.140)$$

$$K_{NaOH,100^\circ C} = 156 - 1.5 \Omega_{NaOH} \quad 9 \leq \Omega_{NaOH} < 16 \quad (5.141)$$

where Ω_{NaOH} depends on the concentration and density levels of the NaOH solution:

$$\Omega_{NaOH} = \frac{M_{NaOH} \rho_{NaOH}}{1000 + (40 M_{NaCl})} \quad (5.142)$$

The voltage drop across the cathode can be written as follows:

$$V_c = c_c \log \left(\frac{i}{i_{0,c}} \right) \quad (5.143)$$

Here, c_c is the constant which is determined experimentally, $i_{0,c}$ represents the exchange current density. Both c_c and $i_{0,c}$ depend on the nature of the reaction. $i_{0,c}$ also depends on the cathode material and the temperature (i.e. for steel $i_{0,c} = 0.0656$).

5.6.4 Entropy Balance Equation

Consequently, the steady state entropy balance equation for the light-based PEC reactor can be written as

$$\dot{m}_1 s_1 + \dot{m}_4 s_4 + \frac{\dot{Q}_{in}}{T_0} + \dot{S}_{gen} = \dot{m}_2 s_2 + \dot{m}_3 s_3 + \dot{m}_5 s_5 + \dot{m}_6 s_6 \quad (5.144)$$

Here, s_{1-6} represents the specific entropies of the associated streams. \dot{S}_{gen} is the rate of entropy generation of the reactor and T_0 is the ambient temperature.

5.6.5 Exergy Balance Equation

The steady state exergy balance equation for the light-based PEC reactor can be written as follows:

$$\dot{m}_1 ex_1 + \dot{m}_4 ex_4 + \dot{W}_{in} + \dot{Q}_{in} \left(1 - \frac{T_0}{T_r}\right) = \dot{m}_2 ex_2 + \dot{m}_3 ex_3 + \dot{m}_5 ex_5 + \dot{m}_6 ex_6 \quad (5.145)$$

5.6.6 Reynolds Number

The Reynolds Number, the non-dimensional velocity, can be defined as the ratio of the inertia force (ρuL) and the viscous or friction force (μ) and interpreted as the ratio of twice the dynamic pressure (ρu^2) and the shearing stress ($\mu u/L$)

$$Re = \frac{\rho uL}{\mu} = \frac{uL}{\nu} \quad (5.146)$$

where Re is the dimensionless Reynolds number, ρ is the density (kg/m^3), u is the velocity based on the actual cross section area of the duct or pipe (m/s), μ is the dynamic viscosity (Ns/m^2), L is the characteristic length (m), and ν is the kinematic viscosity (m^2/s).

For the modified reactor shown in Figure 4.6, we can calculate the Reynolds number for the pipe and the rectangular duct. For the pipe, the characteristic length is the hydraulic diameter which is given as

$$d_h = \frac{4\pi(r_o^2 - r_i^2)}{2\pi(r_o + r_i)} = 2(r_o - r_i) \quad (5.147)$$

The hydraulic diameter of a rectangular tube or duct is given as

$$d_h = \frac{4ab}{2(a + b)} = \frac{2ab}{a + b} \quad (5.148)$$

5.6.7 Transport Equations

In fluid dynamics, turbulence kinetic energy (TKE) is the mean kinetic energy per unit mass associated with eddies in turbulent flow. In ANSYS fluent, the turbulence kinetic energy, k is defined as follows:

$$\frac{\partial}{\partial t}(\rho k) + \frac{\partial}{\partial x_i}(\rho k u_i) = \frac{\partial}{\partial x_j} \left[\left(\mu + \frac{\mu_t}{\sigma_k} \right) \frac{\partial k}{\partial x_j} \right] + P_k + P_b - \rho \varepsilon - Y_M + S_k \quad (5.149)$$

The scalar dissipation rate ε is computed with a model transport equation similar to that used in the standard k - ε model and can be defined as follows:

$$\frac{\partial}{\partial t}(\rho\varepsilon) + \frac{\partial}{\partial x_i}(\rho\varepsilon u_i) = \frac{\partial}{\partial x_j} \left[\left(\mu + \frac{\mu_t}{\sigma_\varepsilon} \right) \frac{\partial \varepsilon}{\partial x_j} \right] + C_{1\varepsilon} \frac{\varepsilon}{k} (P_k + C_{3\varepsilon} P_b) - C_{2\varepsilon} \rho \frac{\varepsilon^2}{k} + S_\varepsilon \quad (5.150)$$

The turbulent (or eddy) viscosity can be calculated as follows:

$$\mu_t = \rho C_\mu \frac{k^2}{\varepsilon} \quad (5.151)$$

where P_k is the kinetic energy due to mean velocity gradients, P_b is the buoyancy, Y_M is the fluctuating dilatation, σ_k is the turbulent Prandtl number for k (1.0), σ_ε is the turbulent Prandtl number for ε (1.3), $C_{1\varepsilon}$ is 1.44, $C_{2\varepsilon}$ is 1.92, C_μ is 0.09, and S_k and S_ε are user-defined source terms.

5.6.8 Meshing Details

The mesh generation study is one of the most critical aspects of engineering simulation. Too many cells may result in long solver runs, and too few may lead to inaccurate results. ANSYS meshing technology provides a means to balance these requirements and obtain the right mesh for each simulation in the most automated way possible. Unless specified otherwise, ANSYS meshing automatically sets default mesh size controls on the geometry. However, to obtain more control over certain areas of the model global, body, face, edge or vertex sizing controls are inserted. The details of these sizing controls are listed in Table 5.1

Figure 5.3 displays the generated mesh for case 1 and 2 respectively. It is noticeable that two different meshing techniques are used for case 1 and 2. While case 1 displays a tetrahedral mesh, case 2 displays an unstructured hexahedral mesh technique. An irregular pattern of the tetrahedral mesh is expected to provide non-symmetrical distributions of the major field variables. Hence both mesh techniques are applied to get the most accurate results possible.

Table 5.1: Meshing details.

Sizing	Case 2: Front view	Case 3: Membrane
Use advanced size function	On: Curvature	On: Curvature
Relevance center	Fine	Coarse
Smoothing	High	Medium
Span angle centre	Fine	
Curvature normal angle	10	18
Min size	4.5607E-002 mm	7.881E-002 mm
Max face size	4.56070 mm	7.8810 mm
Max size	9.12150 mm	15.7620 mm
Growth rate	12 mm	1.2
Minimum edge length		0.50 mm
Inflation		
Inflation option	Smooth transition	Smooth transition
Transition ratio	0.272	0.272
Maximum layers	2	2
Growth rate	1.2	1.2
Statistics		
Nodes	3917	1831
Elements	3696	1746

Figure 5.4 displays the mesh generated for the third case. It is evident that high numbers of divisions are given at the edges and corners especially around the membrane (bluff body).

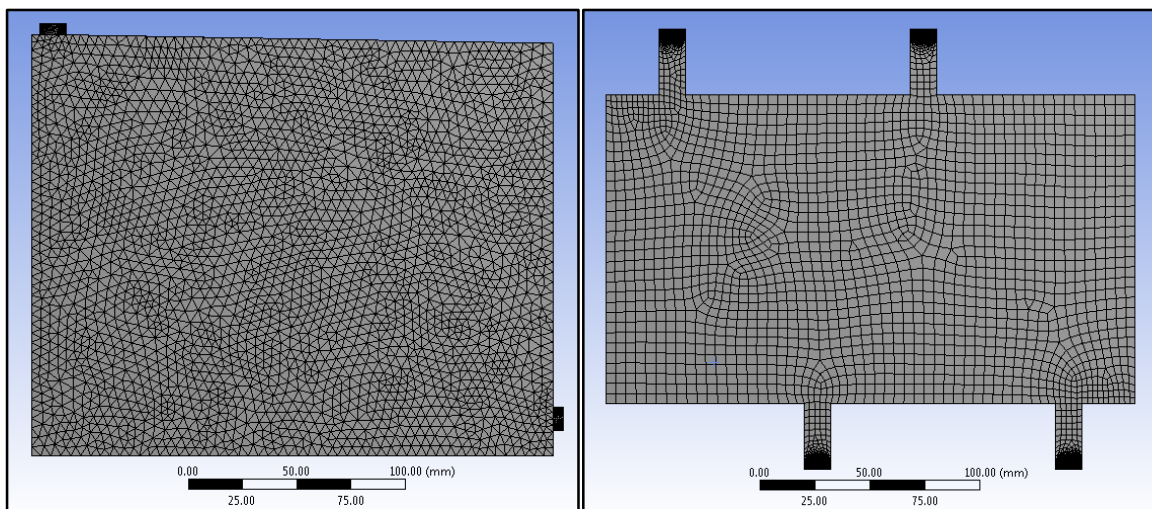


Figure 5.3: Case 1 and 2 mesh using ICEM CFD.

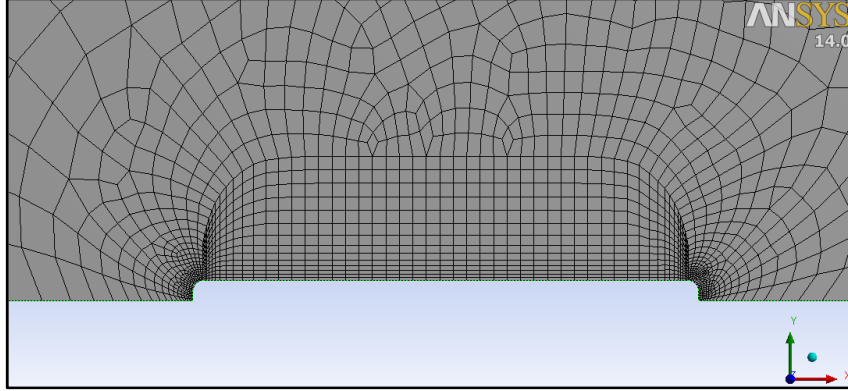


Figure 5.4: Case 3 mesh using ICEM CFD.

5.7 Energy and Exergy Efficiencies

The determination of energy losses and exergy destruction for solar field allows for subsequent calculation of efficiencies according to the following equations:

$$\eta_{en,field} = \frac{\dot{E}_2}{\dot{E}_1} = 1 - \frac{\dot{E}_{loss}}{\dot{E}_1} \quad (5.152)$$

$$\eta_{ex,field} = \frac{\dot{E}x_2}{\dot{E}x_1} = 1 - \frac{\dot{E}x_d}{\dot{E}x_1} \quad (5.153)$$

The field efficiencies can be calculated for each day of the year and for each hour of daylight. Furthermore, average values can be determined for each month and for the year. Consequently, the energy and exergy efficiencies of the spectral splitter are defined as follows:

$$\eta_{en,hm} = 1 - \frac{\dot{E}_{loss}}{\dot{E}_2} \quad (5.154)$$

$$\eta_{ex,hm} = 1 - \frac{\dot{E}x_d}{\dot{E}x_2} \quad (5.155)$$

The energy and exergy efficiencies of the filter splitter are defined as follows:

$$\eta_{en,fs} = 1 - \frac{\dot{E}_{loss}}{\dot{E}_3} \quad (5.156)$$

$$\eta_{ex,fs} = 1 - \frac{\dot{E}x_d}{\dot{E}x_3} \quad (5.157)$$

The thermal energy rate generated by the volumetric receiver results from the energy efficiency of the receiver, which can be assumed based on practical values. The thermal efficiency of the receiver, representing the ratio of the delivered heat rate to the light energy rate provided as an input, is defined by the following equation:

$$\eta_{en,rec} = \frac{\dot{Q}_9}{\dot{E}_4} \quad (5.158)$$

The exergy efficiency of the desalination plant is defined as the ratio of the minimum work of separation (\dot{W}_{min}) required for the desalination process to the actual work consumed. This may be written as follows:

$$\eta_{ex,des} = \frac{\dot{W}_{min}}{\dot{W}_{in}} \quad (5.159)$$

The energy efficiency of the photoelectrochemical reactor system can be defined as the ratio of the useful energy output from the system to the input energy to the system.

$$\eta_{en} = \frac{\sum \text{Useful energy output}}{\sum \text{Energy input}} \quad (5.160)$$

For the present PEC system, energy efficiency can be defined in two ways. In the first definition, only hydrogen is considered as the desired/useful output. This equation can be written as follows:

$$\eta_{en,1} = \frac{\dot{m}_6 HHV_{H_2}}{\dot{W}_{in} + \dot{m}_1 h_1 + \dot{m}_4 h_4} \quad (5.161)$$

In the second definition, hydrogen gas along with sodium hydroxide and chlorine gas is considered as desired/useful outputs. Therefore, the second energy efficiency equation can be written as follows:

$$\eta_{en,2} = \frac{\dot{m}_6 HHV_{H_2} + \dot{m}_3 h_3 + \dot{m}_5 h_5}{\dot{W}_{in} + \dot{m}_1 h_1 + \dot{m}_4 h_4} \quad (5.162)$$

Here, HHV is the higher heating value of hydrogen and \dot{W}_{in} is the input work to the PEC system as shown in Eqs. (5.93)-(5.95).

The exergy efficiency of the PEC system can be defined based on the exergy content of the system inputs and outputs. This definition is based on the second law of thermodynamics and

gives a better insight of the system performance. Correspondingly, the exergy efficiency can be defined as the ratio of the useful exergy output from the system to the total exergy input below:

$$\eta_{ex} = \frac{\text{Useful exergy output}}{\text{Total exergy input}} = 1 - \frac{\text{Total exergy destruction}}{\text{Total exergy input}} \quad (5.163)$$

Similar to the energy efficiency for the present PEC system is defined by two different ways. In the first definition, only where hydrogen is considered as the desired/useful output. Hence, the exergy efficiency can now be written as follows:

$$\eta_{ex,1} = \frac{\dot{m}_6 ex_6}{\dot{W}_{in} + \dot{m}_1 ex_1 + \dot{m}_4 ex_4} \quad (5.164)$$

In the second case, chlorine and sodium hydroxide solution is also considered as the desired/useful output in addition to hydrogen. Hence, the second exergy efficiency definition can now be written as follows:

$$\eta_{ex,2} = \frac{\dot{m}_6 ex_6 + \dot{m}_3 ex_3 + \dot{m}_5 ex_5}{\dot{W}_{in} + \dot{m}_1 ex_1 + \dot{m}_4 ex_4} \quad (5.165)$$

5.8 Optimisation Study

One of the key goals in this research work is to optimise the energy and exergy efficiency of the PEC system and the large scale integrated system. Single objective optimisation can be applied with object function being the energy/exergy efficiency. Some trade-offs can also be considered such as maximising the efficiency of the PEC system while minimising the cost to build the reactor. Hence, multi-objective optimisation can be formulated for improved system design and operation. Genetic algorithms are commonly used for multi-objective optimisation problems. Figure 5.6 shows the flow chart of a genetic algorithm for multi-objective optimisation process.

As reviewed by (Dincer and Rosen, 2012), there are numerous analytical and numerical methods for optimisation of complex systems. A multi-objective optimisation problem can be reduced to a single objective function by applying constraints or formulating a compounded objective function. For instance, if the objective function to minimise are: (i) Sustainability Index $SI = 1 - \psi$ (Dincer and Rosen, 2012), and the cell Voltage expressed in Eq. (5.93) where both

these parameters depend on a number of variables $x_i, i = 1 \dots n$, the multi-objective optimisation problem can now be formulated mathematically as

$$\min\{SI(x_i), LPC(x_i), i = 1 \dots n | N = \text{fixed constraints}\} \quad (5.166)$$

where N represents the number of outputs in the PEC system.

As mentioned in Dincer and Zamfirescu (2014), the multi-objective optimisation problem (Eq. (5.166)) can now be simplified to k single objective optimisation problems as follows:

$$\min\{SI(x_i), i = 1 \dots n | LPC_j, j = 1 \dots k, n = \text{fixed}, \text{other constraints}\} \quad (5.167)$$

Other methods of optimisation such as Lagrange multiplier can be applied such as evolutionary algorithms with random but educated search depending on the nature of the constraints. The search progresses with these evolutionary algorithms according to the natural selection theory of the fittest. These methods can be applied to discontinuous functions which is a great advantage when complex systems are optimised.

As mentioned previously the design of the PEC system requires the application of multi-objective multivariable optimisation methods where the goal is to maximise the efficiency and minimise the cost. The best design selection must be made based on a trade-off analysis. The Pareto front specifies the best performance as shown in Figure 5.5. The system's profitability increases with increase in the number of generated outputs.

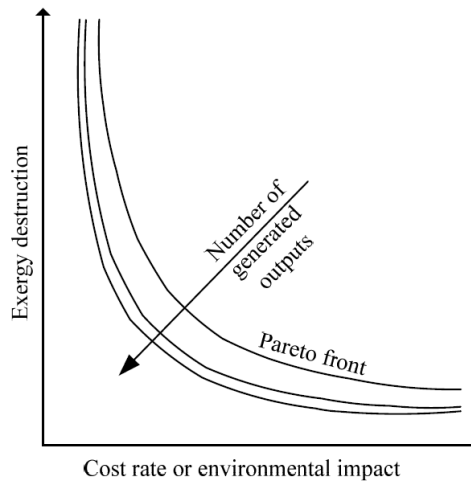


Figure 5.5: Multi-objective optimisation of systems (Dincer and Zamfirescu, 2014).

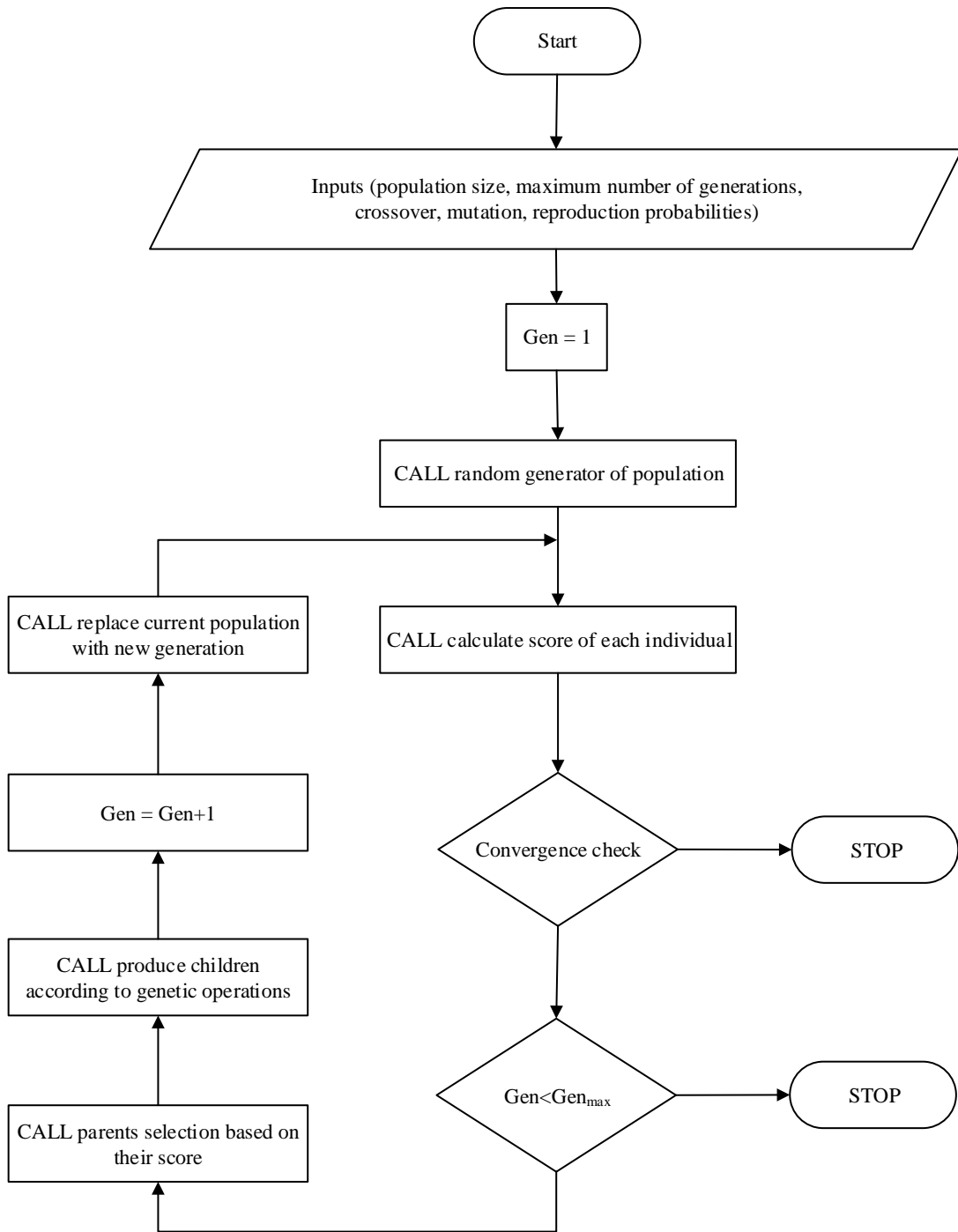


Figure 5.6: Genetic algorithm optimisation technique flowchart (Adapted from Tarique, 2011).

Chapter 6: Results and Discussion

Two types of results are obtained in this work. First results reflect the system analysis through energy and exergy methods. Exergy destructions for each component and the overall energy and exergy efficiencies as well as production rate are reported for a relevant case study. The second type of results refer to comparative assessment of the system aiming to determine the system feasibility and potential with respect to conventional systems.

6.1 System Efficiencies and Exergy Destructions

Here, a case study is considered which is chosen such that the system efficiencies, exergy destructions, and production rates can be conservatively determined. A location is chosen where sufficient solar radiation exist; this is assumed to be 2 MWh/m^2 per year. The AM 1.5 solar spectrum is also assumed according to the ASTM (2013). The number of operational sunlight hours per year is taken 4000 h based on the study presented previously by Zamfirescu and Dincer (2014). Thence, the annual average direct and circumsolar irradiance is taken 500 W/m^2 .

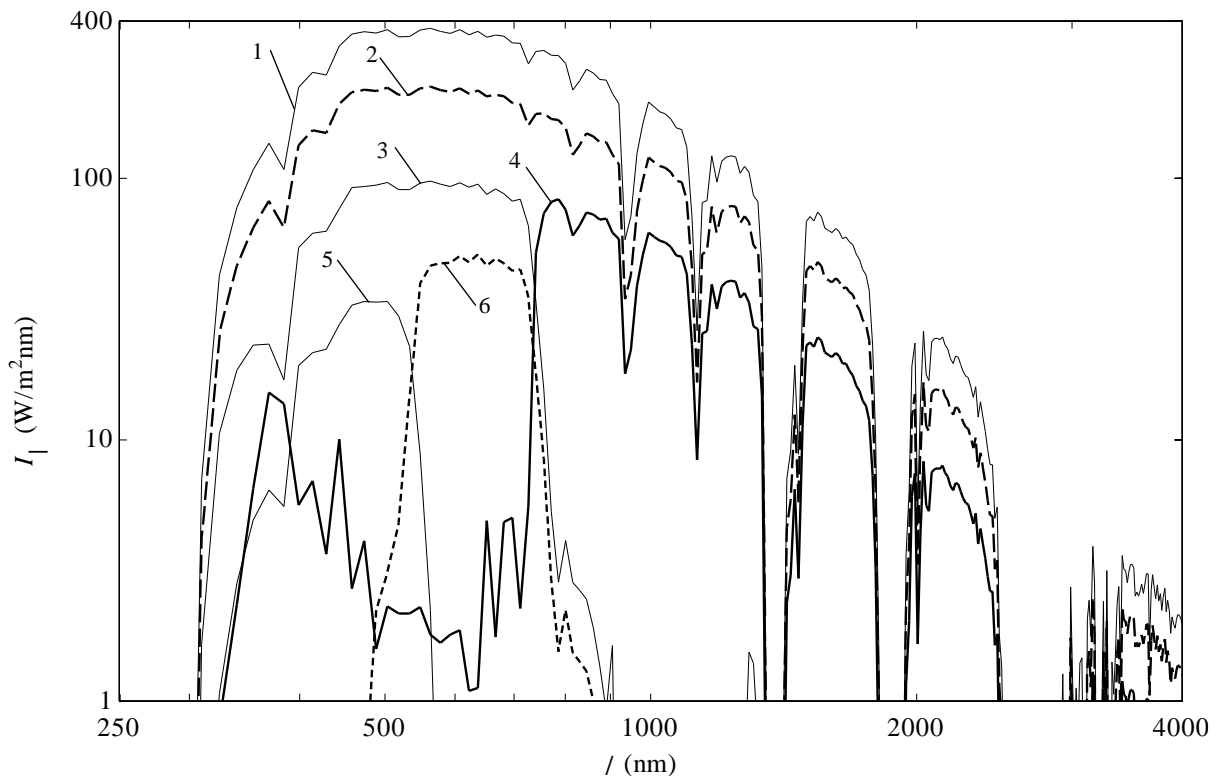


Figure 6.1: Spectral irradiance within the light processing subsystem.

The Engineering Equation Solver (EES) is used to solve the balance equations of each system component. The results for the “light processing subsystem” are given here first. For this subsystem, energy rate, exergy rate, entropy rate, and temperature of the light radiation for state points 1-6 are given in Table 6.1 with respect to square metre of reflecting surface. As remarked, the temperature of the upper spectrum radiation (#5 in Figure 4.19) is the highest with 9089 K while the infrared radiation has (#4 in Figure 4.19) 4486 K.

Also, exergy is lost along the light pathway as the incident is 475.4 W per square metre of reflecting surface whereas the processed radiation in #4, #5, and #6 in Figure 4.19 totals $156.9 + 54.92 + 80.83 = 292.65$ W representing 38.4% losses due to irreversibilities.

The way in which the spectral splitter performs can be observed in Figure 6.1 which shows the spectral irradiance at each state point along the light pathway. The most of exergy destruction in this system is due to the heliostat field; the shading, blocking, light attenuation and intercept factor of the light affect largely the light radiation losses in the process 1 – 2. The pie chart from Figure 6.2 shows the exergy destructions within the light processing subsystem. It can be seen that the heliostat field account for 91% of the exergy destruction within the light processing subsystem, followed by 5% and 4% for the upper/middle spectral splitter and hot mirror spectral splitter respectively. The total exergy destruction corresponds to 182.71 W per square metre of heliostat.

Table 6.1: Energy, exergy, entropy, and temperature within light processing subsystem.

<i>State</i>	\dot{E} (W)	\dot{E}_x (W)	\dot{S} (W/K)	<i>T</i> (K)
1	500	475.4	0.08246	6064
2	324.9	308.7	0.05433	5979
3	150.1	145.3	0.01615	9294
4	168.1	156.9	0.03747	4486
5	56.79	54.92	0.006248	9089
6	83.89	80.83	0.01028	8163

Table 6.1 demonstrates the energy in W per square metre of reflecting area, exergy in W per square metre of reflecting area, and entropy in W/K per square metre of reflecting area and temperature of all state points within the light processing subsystem. The salinity in g salt/kg solution, specific exergy in kJ/kg, specific enthalpy in kJ/kg and specific entropy in kJ/kgK for all the state points in the desalination subsystem is demonstrated in Table 6.2.

Table 6.2: Salinity, specific exergy, enthalpy, and entropy of the desalination subsystem.

State	ω (g salt/kg solution)	ex (kJ/kg)	h (kJ/kg)	s (kJ/kgK)
8	1.55	0.7319	62.93	0.2245
10	6.11	25.01	85.88	0.2625
14	0.23	0	104.9	0.3672
15	6.11	0.8742	62.55	0.2244

The state parameters for the desalination system have been determined based on balanced equations and stated assumptions. The exergy destruction depends on the energy efficiency of the heat engine incorporated to the desalination unit and on the considered fraction f of the flow diverted to the salt concentration subunit; $f = \dot{m}_{17} / \dot{m}_{16}$ (Figure 5.1). The exergy destruction per kg of brine water input is shown in Figure 6.3 for f varied from 0 to 1 and two extreme values for heat engine efficiencies. The impact of heat engine efficiency is remarked.

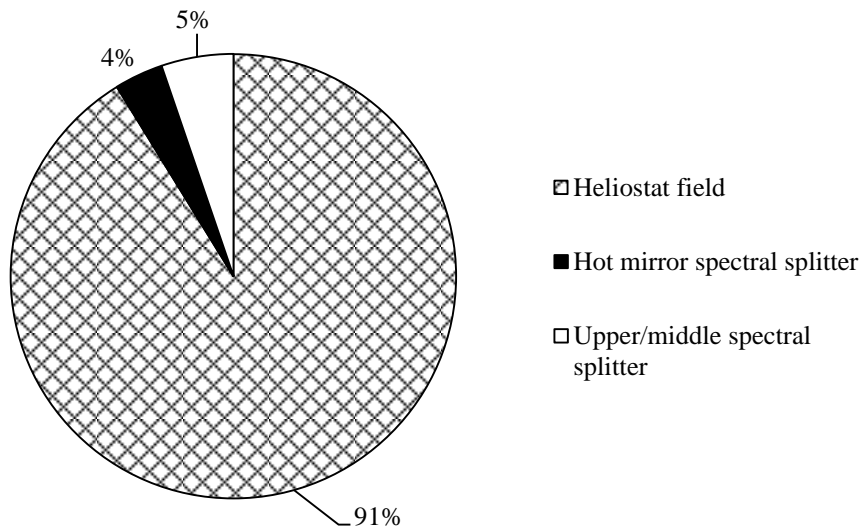


Figure 6.2: Exergy destructions within light processing subsystems.

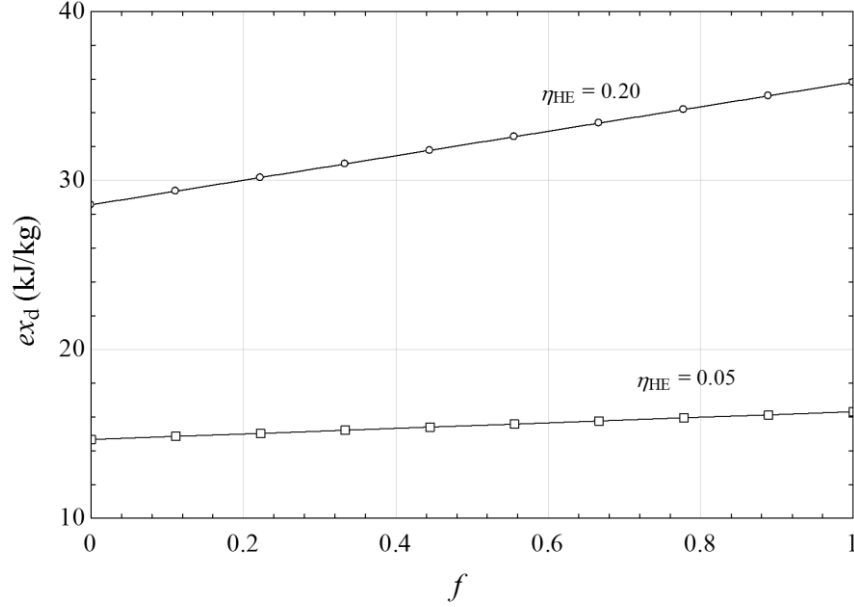


Figure 6.3: Exergy destruction per kg of brine input for the desalination subsystem.

6.2 PEC Chloralkali Electrolysis

Detailed parametric studies are performed for the novel PEC chloralkali process and five different cases are considered where one of the parameters is fixed at a constant value while effect of varying other parameters are documented. Table 6.3 shows the mass flow rates (kg/s), molar concentration, concentration (kg/kg solution), specific enthalpy (kJ/kg), specific entropy (kJ/kgK), standard chemical exergy (kJ/kg), and specific physical exergy (kJ/kg) for all state points in the PEC system.

Table 6.3: Mass flow rate, molar and mass concentrations, specific enthalpy, entropy, and chemical and physical exergies of the PEC system.

State	\dot{m} (kg/s)	M_s (mol/L)	x_s (kg/kg solution)	h (kJ/kg)	s (kJ/kgK)	ex_{ch} (kJ/kg)	ex_{ph} (kJ/kg)
1	0.01	10.39	0.3779	-1939	7.847	80.67	0
2	0.007319	3.02	0.15	-3954	1.089	60	0
3	0.001635			1.18E-07	3.146	1743	0
4	0.01			-13422	10.48	49.96	0
5	0.01094	5	0.1667	-3669	9.436	200.6	0
6	5.36E-05			-1.3E-06	64.82	147486	0

6.2.1 Case Study 1

For the first case study, ambient temperature is kept constant at 25°C and the operating temperature is being varied. Figure 6.4 shows that increasing the operating temperature increases the hydrogen production. The prime reason for this is the fact that increasing the temperature increases the conductivities of the membrane and the electrolyte solutions which implies more H₂ for the same input energy. Higher temperature also means a more derived (high concentration) NaCl. With the steady state assumptions, this means that more Na⁺ and Cl⁻ is produced, hence more OH⁻ are neutralised and more H₂ is produced. Figure 6.4 also suggests that increasing the temperature decreases the input work rate. This is mainly because for higher temperatures the voltage losses decreases (especially voltage drop across catholyte and anolyte solution), which means for the same current, the required cell voltage is less, which decreases the input work rate.

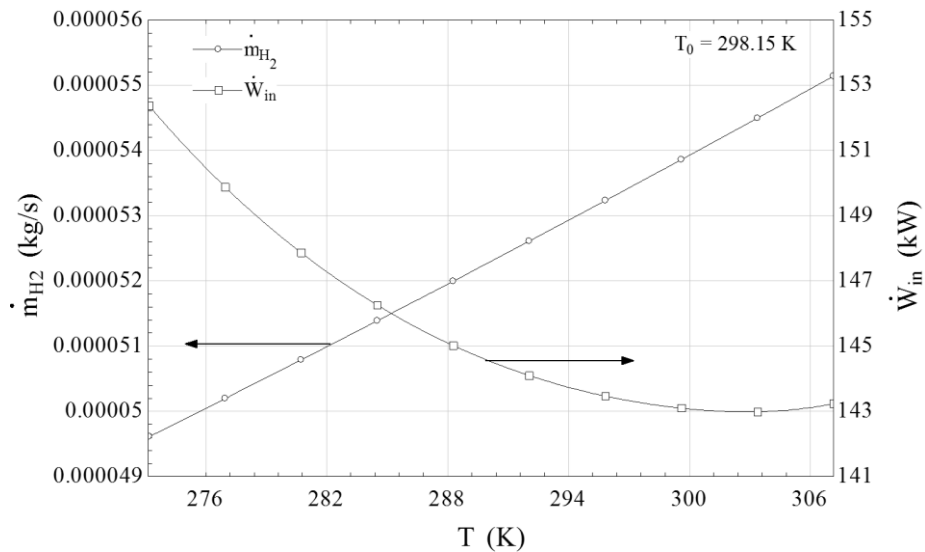


Figure 6.4: Effect of operating temperature on hydrogen production rate and required work input.

Figure 6.5 shows that increasing the operating temperature increases the required current. As mentioned previously, increasing the temperature increases the concentration of NaCl in the input brine solution, which increases the H₂ production. In accordance with Faraday's law, the input current required is directly proportional to the hydrogen produced. Hence higher current is needed to produce the increased H₂. Figure 6.5 also shows that increasing the operating temperature decreases the input voltage. As discussed previously, increasing the temperature decreases the voltage losses. Hence, the input voltage decreases for the same current.

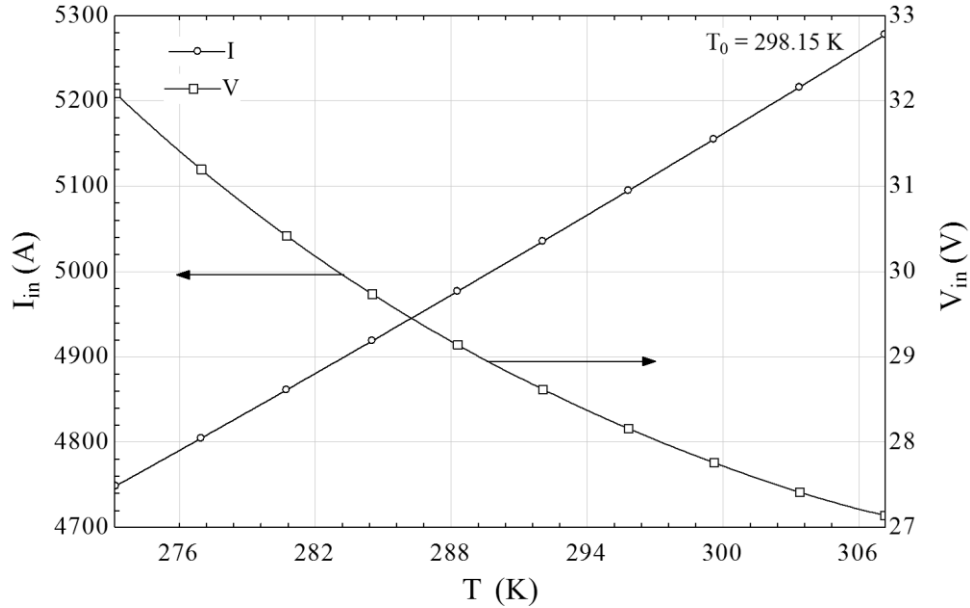


Figure 6.5: Effect of operating temperature on input current and voltage.

Figure 6.6 shows the effect of varying operating temperatures on energy and exergy efficiencies of the PEC system. Note that the two exergy definitions are used as mentioned in Eqs.(5.164) and (5.165). As mentioned earlier, increasing the operating temperature decreases the losses in the PEC system. Hence in general increasing the operating temperatures, the system becomes more efficient both energetically and exergetically. It is important to note that there is a significant increasing in $\eta_{ex,2}$ (around 2%) as opposed to $\eta_{ex,1}$ (around 1%). This is because more exergetic components in Eq. (5.165), hence the effect is more prominent.

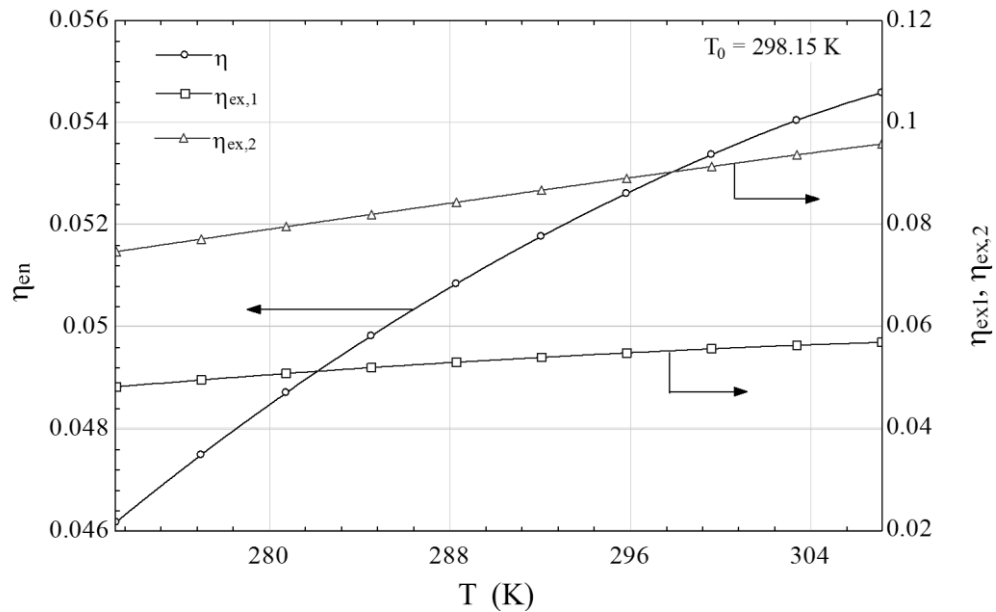


Figure 6.6: Effect of operating temperature on energy and exergy efficiencies.

Figure 6.7 shows that increasing the operating temperatures increases the production yield for both chlorine and hydrogen gas. As mentioned previously, increasing the operating temperature increases the input current. Hence the production yield increases for both the exit gases from the PEC system.

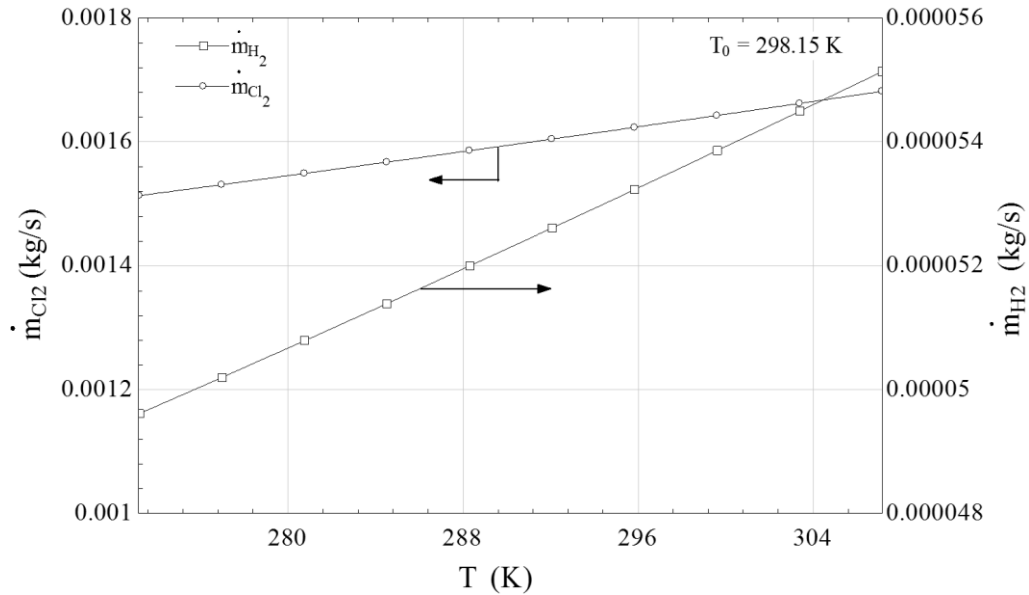


Figure 6.7: Effect of operating temperature on production yield for chlorine and hydrogen gases.

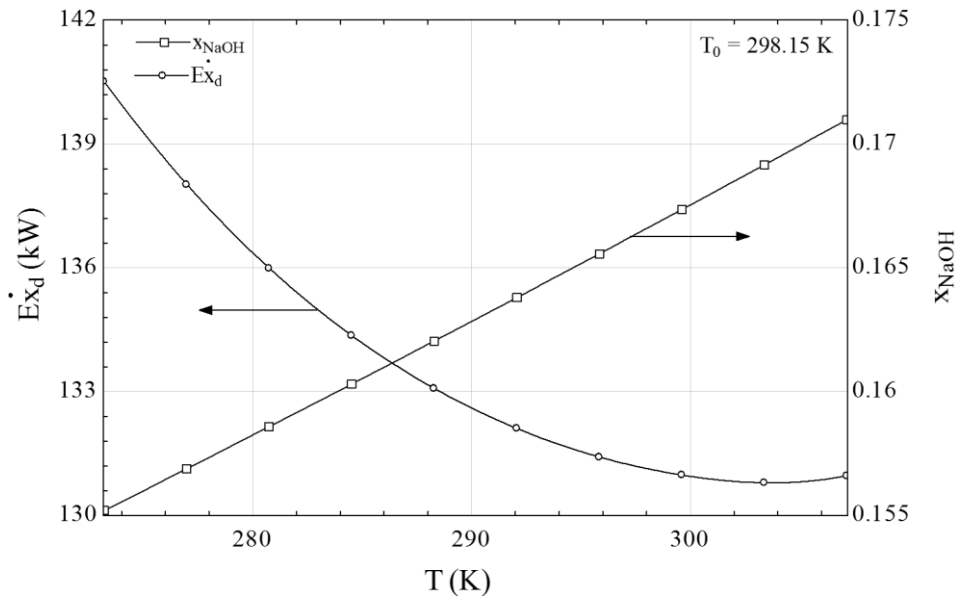


Figure 6.8: Effect of operating temperature on exergy destruction rate and NaOH exit concentration.

Figure 6.8 shows that increasing the operating temperature decreases the rate of exergy destruction. This is mainly due to the decrease in the required work input and voltage losses when temperature increases. Figure 6.8 also shows that increasing the operating temperature increases the exit concentration of sodium hydroxide solution leaving the reactor. As highlighted

previously, at higher temperature, more Na^+ and Cl^- ions are produced and hence more OH^- ions are neutralised. Hence it increases the exit sodium hydroxide concentration.

Hence, from Figures 6.4 – 6.7, it can be said that from both energetic and exergetic point of view, higher operating temperature is preferred to prevent high voltage losses, higher production yield and better efficiencies.

6.2.2 Case Study 2

For the second case study, operating temperature is kept constant at 25°C and ambient temperature is being varied. Figure 6.9 shows the effect of ambient temperature on energy and exergy efficiencies. It can be seen that increasing the ambient temperature has no effect on the energy efficiency. However, exergy efficiency decreases with increase in ambient temperature. This is because no physical exergy exists at ambient temperature. As ambient temperature increases, physical exergy content increases in Eq. (5.165) which decreases the exergy efficiency of the PEC system.

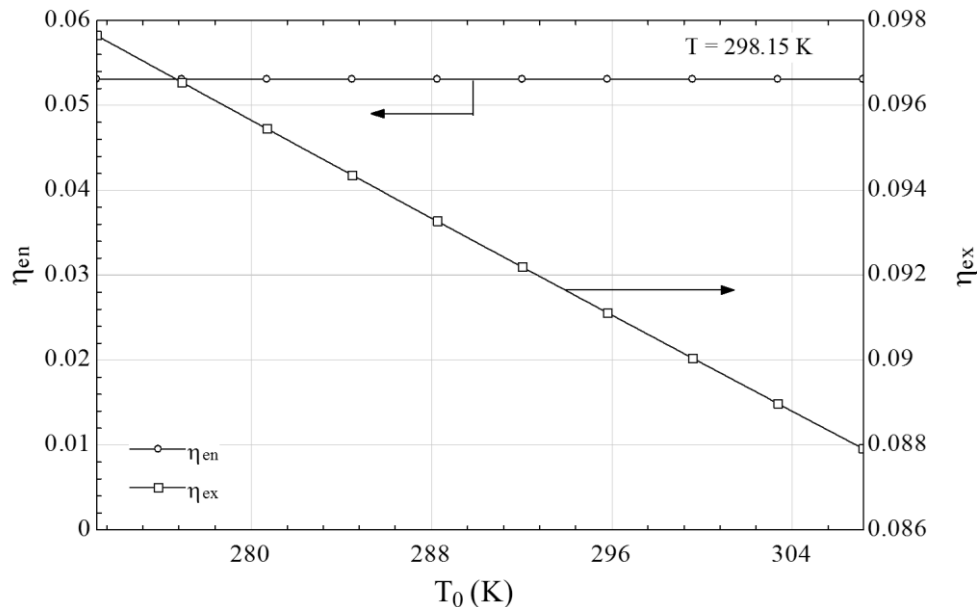


Figure 6.9: Effect of ambient temperature on energy and exergy efficiencies.

Figure 6.10 shows that ambient temperature has no effect on the production yield for hydrogen and chlorine gas. This is obvious since there is no change in the applied current or voltage. Figure 6.11 shows that the ambient temperature has no effect on the input work input. As explained earlier, no change in current or voltage means the input work is not affected.

However, from the figure we can see that increasing the ambient temperature decreases the exergy destruction rate. This is due to the difference in the input and output physical exergy content with increase in ambient temperature. It is important to note that ambient temperature has no effect on the performance of the PEC from energy point of view. However, from an exergy point of view, a lower ambient temperature is preferred for a higher efficiency.

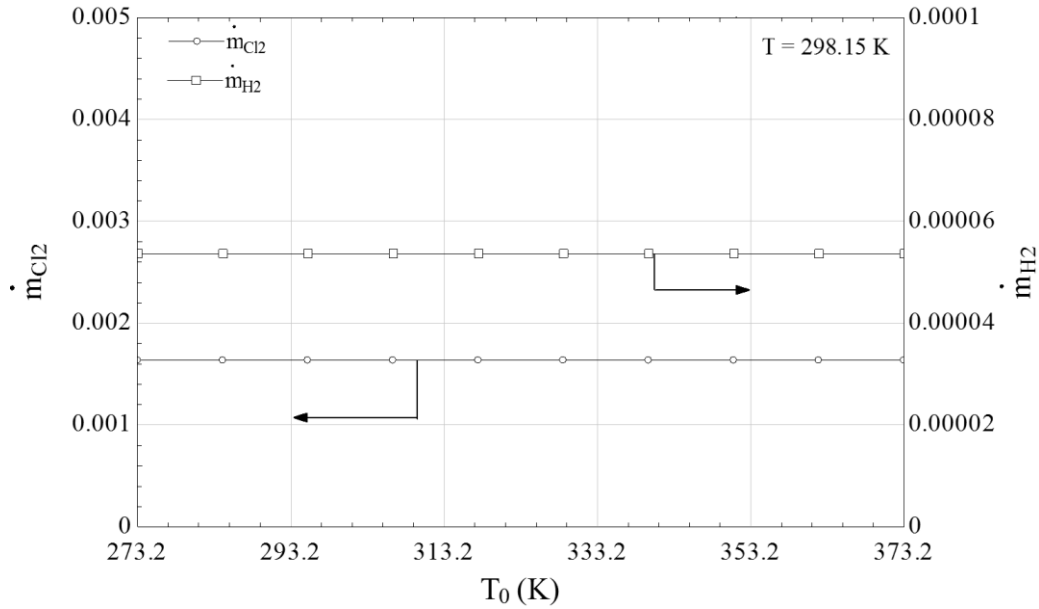


Figure 6.10: Effect of ambient temperature on production yield for hydrogen and chlorine gases.

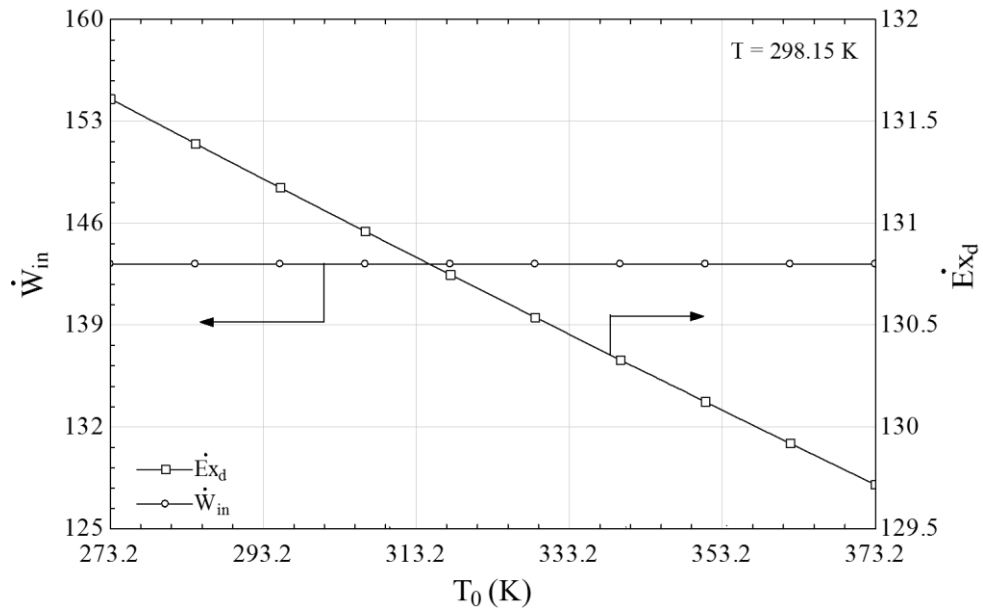


Figure 6.11: Effect of ambient temperature on work input and exergy destruction rates.

6.2.3 Case Study 3

For the third case study, both ambient temperature and operating temperatures are made equal and varied simultaneously. Figure 6.12 shows that increasing the ambient/operating temperature increases the hydrogen production rate. This is expected since we concluded from the previous section that ambient temperature will have little effect on the hydrogen production rate. However, increasing the temperature will increase the conductivities of the membrane and the electrolyte solutions which means more H_2 for the same input energy will be produced. As mentioned previously, higher temperature also means a more derived (high concentration) NaCl. With the steady state assumptions, this means that more Na^+ and Cl^- is produced, hence more OH^- are neutralised and more H_2 is produced. Figure 6.12 also suggests that increasing the temperature decreases the input work rate. This is mainly because at higher temperatures the voltage losses are less (especially voltage drop across catholyte and anolyte solution), which means for the same current, the required cell voltage is less, hence less input work rate.

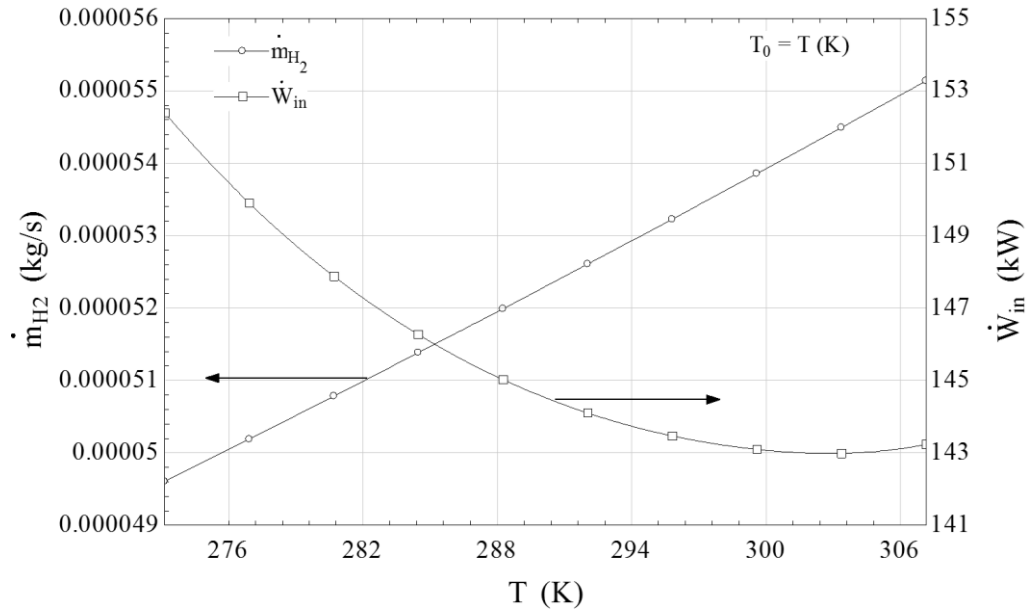


Figure 6.12: Effect of operating and ambient temperatures on hydrogen production and work input.

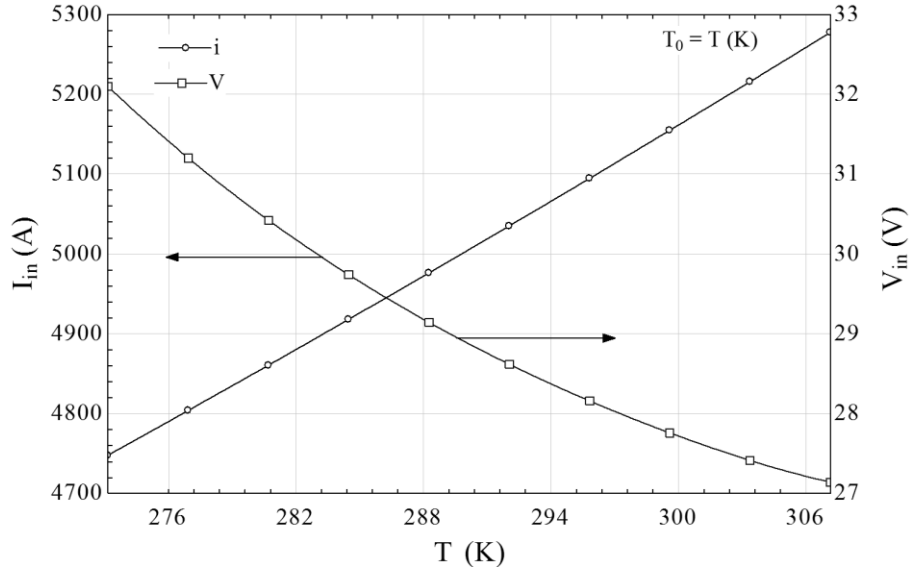


Figure 6.13: Effect of operating and ambient temperatures on input current and voltage.

Figure 6.13 shows that increasing the operating/ambient temperature when both are equal increases the input current while decreases the input voltage to the PEC system. As mentioned previously, increasing the temperature increases the concentration of NaCl in the input brine solution, which increases the H_2 production. In accordance with the Faraday's law, the input current required is directly proportional to the hydrogen produced. Hence higher current is needed to produce the increased H_2 . Figure 6.13 also shows that increasing the operating temperature decreases the input voltage. As discussed previously, increasing the temperature decreases the voltage losses. Hence, the input voltage decreases for the same current.

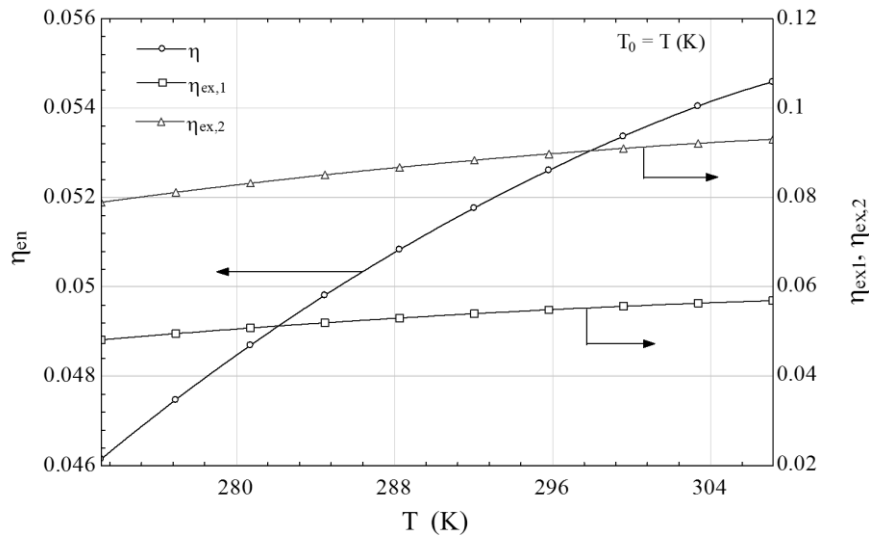


Figure 6.14: Effect of operating and ambient temperatures on energy and exergy efficiencies.

Figure 6.14 shows the effect of operating/ambient temperature on energy and exergy efficiencies when both are equal. It can be seen that increasing the ambient/operating temperature increases both the energy and exergy efficiencies. This figure is very identically to Figure 6.6. It is obvious that the energy efficiency will vary exactly as suggested previously. As mentioned previously, increasing just the ambient temperature decreases the exergy efficiency and increasing just the operating temperature increases the exergy efficiency. Therefore, Figure 6.14 shows the combined effect and it can be seen that overall, the exergy efficiency increases when both ambient and operating temperature are equal and increasing simultaneously.

Figure 6.15 shows that increasing the operating/ ambient temperature increases the production yield for both chlorine and hydrogen gas. This is understandable since increasing the operating temperature increases the input current. Hence the production yield increases for both the exit gases from the PEC system.

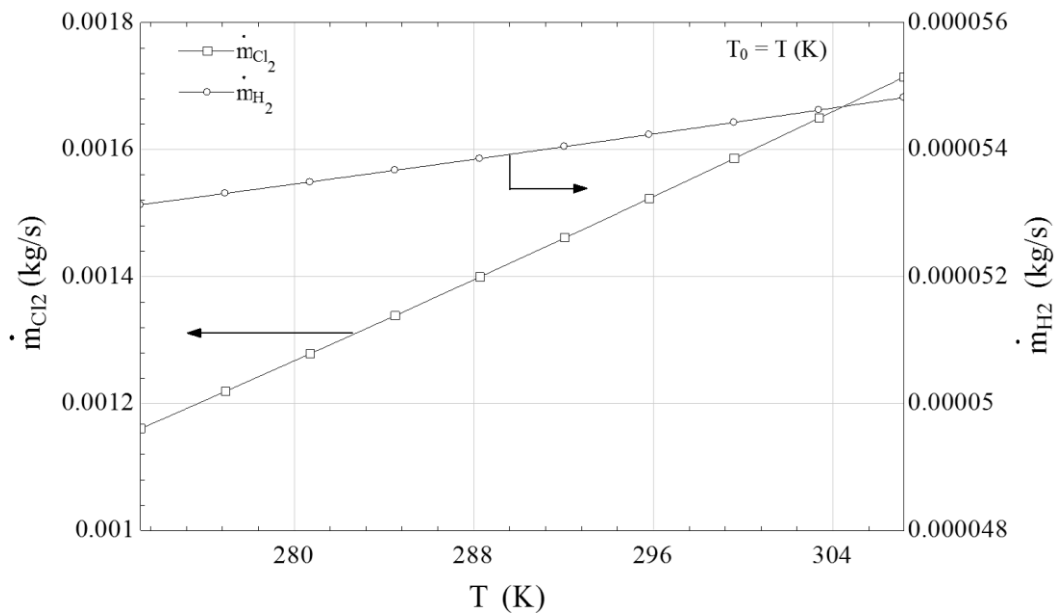


Figure 6.15: Effect of operating and ambient temperatures on production yield for chlorine and hydrogen gases.

6.2.4 Case Study 4

For the fourth case study, the inlet mass flow rate of brine solution (\dot{m}_1) and water (\dot{m}_4) are kept equal and varied simultaneously. Also note that in this case the operating and ambient temperature are kept fixed at 25°C.

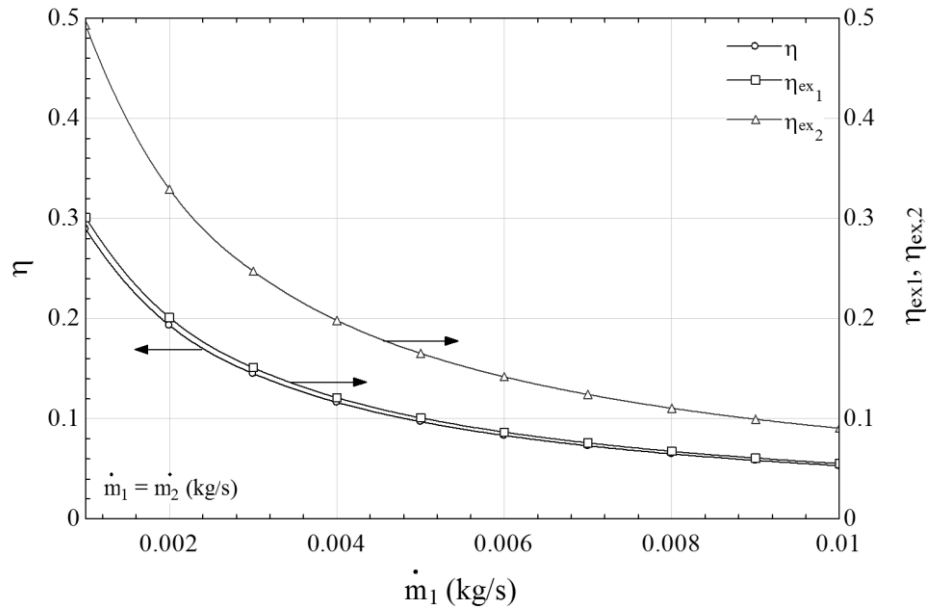


Figure 6.16: Effect of inlet brine mass flow rate on energy and exergy efficiencies.

Figure 6.16 shows that effect of inlet brine mass flow rate on the system efficiencies. It can be seen that increasing the inlet brine solution mass flow rate considerably decreases both energy and exergy efficiencies. The prime reason for this is that with increase in mass flow rate, more Na^+ and Cl^- are produced which will in turn neutralises more OH^- ions. The voltage losses at higher mass flow rate is considerably high which is why both energy and exergy efficiency decreases with increasing inlet mass flow rate.

Figure 6.17 shows that increasing the inlet brine solution mass flow rate increases the rate of hydrogen production and also increases the work input to the PEC system. This is evident since more neutralised OH^- ions will increase the rate of hydrogen production. However, due to the high voltage losses and input current, the required work input is seen to be increasing with increase in inlet mass flow rates.

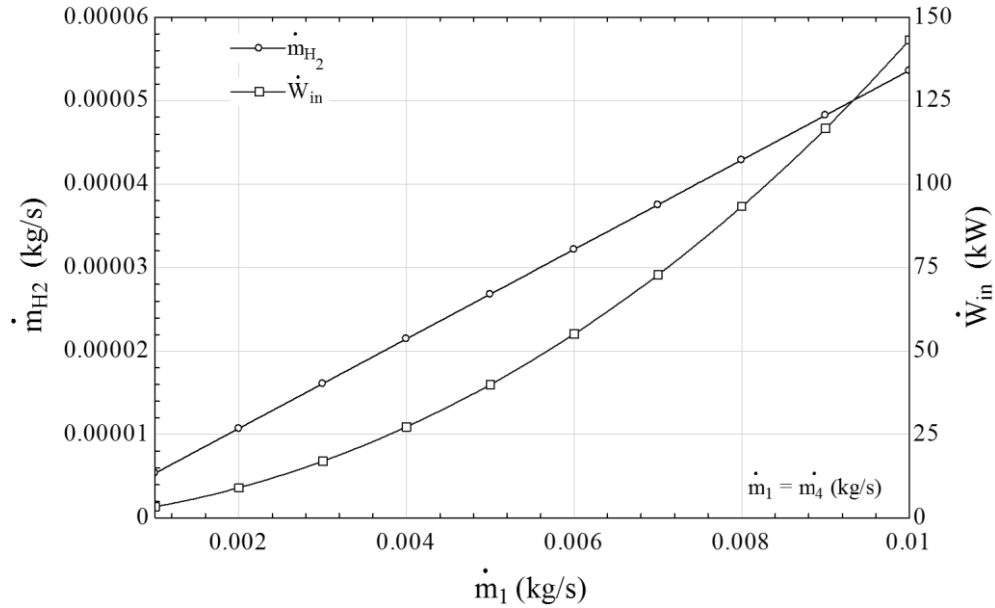


Figure 6.17: Effect of inlet brine mass flow rate on hydrogen production rate and work input.

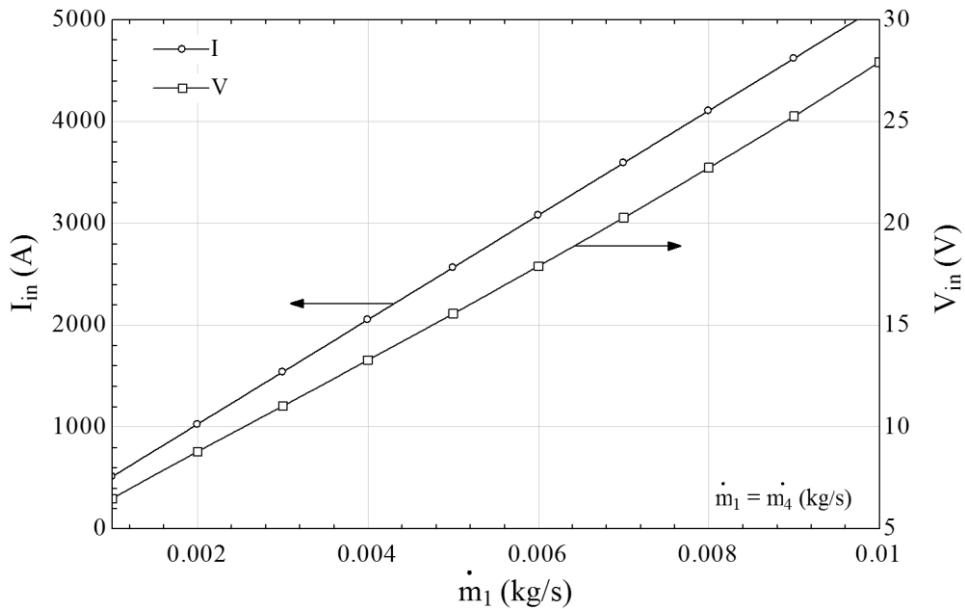


Figure 6.18: Effect of inlet brine mass flow rate on input current and voltage.

Figure 6.18 shows that increasing the inlet brine solution mass flow rate increases both input current and voltage. This is evident from the previous figure since higher mass flow rate increases the hydrogen production rate. Hence in accordance with the Faraday's law, the required current has to increase. Also, due to the increase in required work rate and current, the cell voltage will also increase.

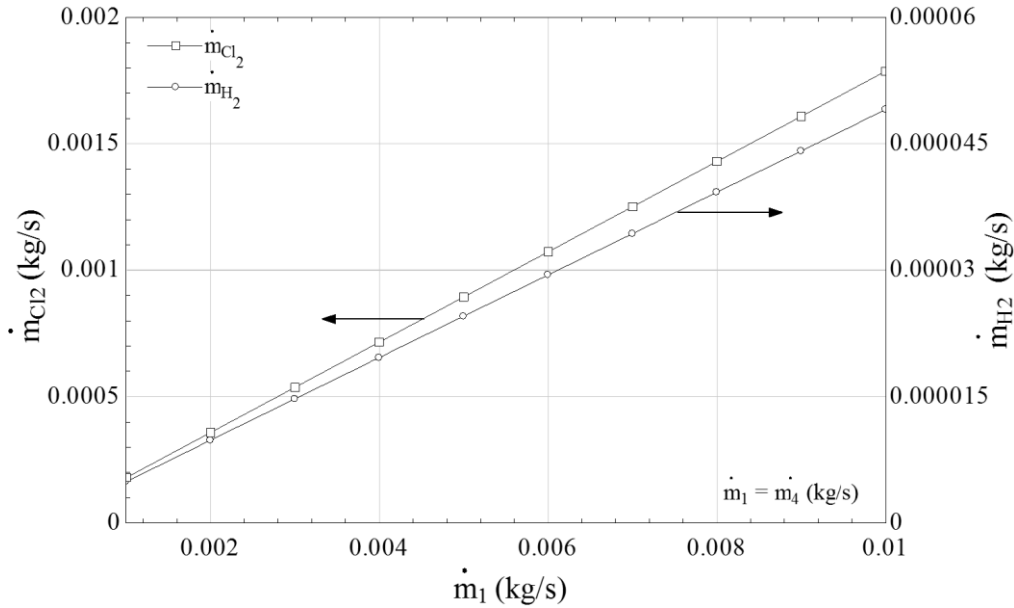


Figure 6.19: Effect of inlet brine mass flow rate on production yield for chlorine and hydrogen gases.

Figure 6.19 shows that increasing the inlet brine solution mass rate increases both the production yield for hydrogen and chlorine gas. It is obvious, as explained previously, that higher current produces more hydrogen and chlorine gas.

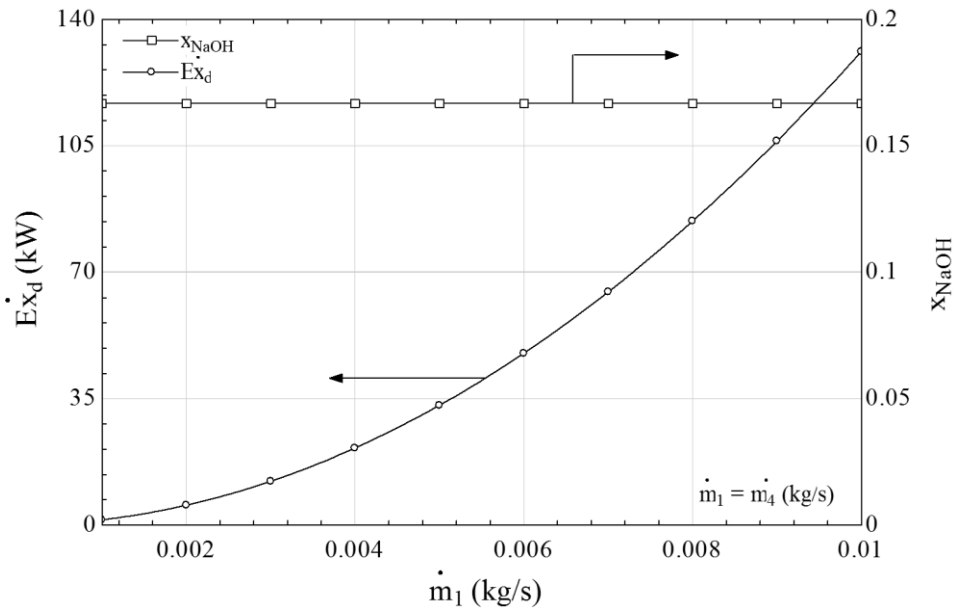


Figure 6.20: Effect of inlet brine mass flow rate on exergy destruction rate and NaOH exit concentration.

Figure 6.20 shows that increasing the inlet brine solution mass flow rate has no effect of the output sodium hydroxide concentration. However, it increases the exergy destruction rate. As mentioned previously, voltage losses are higher at higher mass flow rates. Correspondingly, the exergy losses are also higher at higher mass flow rates.

6.2.5 Case Study 5

In the fifth case study, the exit brine concentration leaving the reactor is varied. Note that the inlet mass flow rates for brine and water are kept constant at 0.01 kg/s. Also note that in this case the operating and ambient temperature are kept fixed at 25°C.

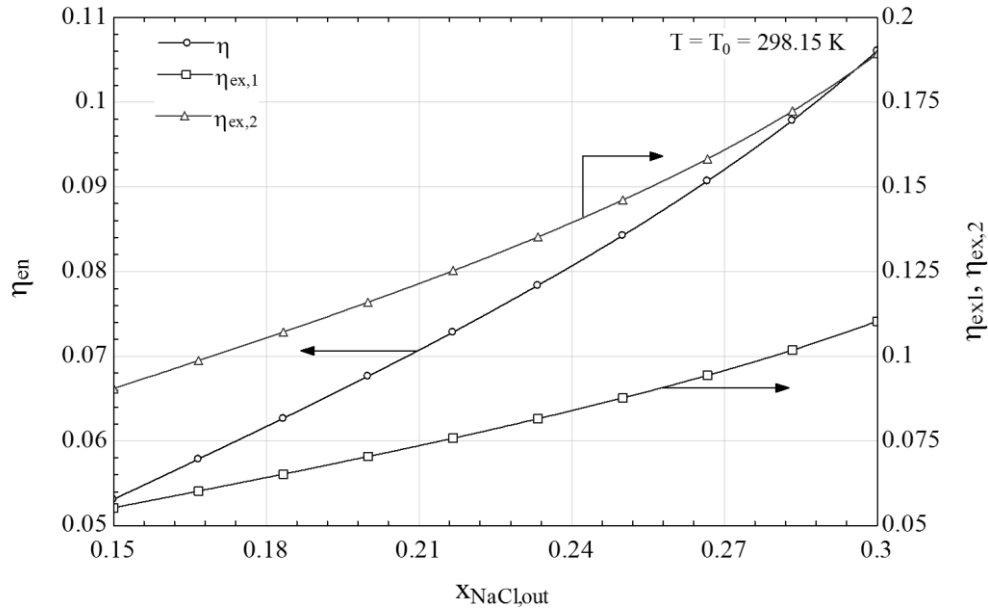


Figure 6.21: Effect of output brine concentration on energy and exergy efficiencies.

Figure 6.21 shows that effect of varying the output concentration of sodium hydroxide solution. It can be seen that higher the output NaOH solution concentration, higher the energy and exergy efficiencies and hence the efficiencies will increase.

Figure 6.22 shows that decreasing the exit concentration decreases the hydrogen production rate and the required work input. This is due to the fact that higher the exit brine concentration, lesser the Na^+ and Cl^- generated. Consequently, less OH^- are neutralised and hence, less H_2 and Cl_2 produced. This is also confirmed in Figure 6.24.

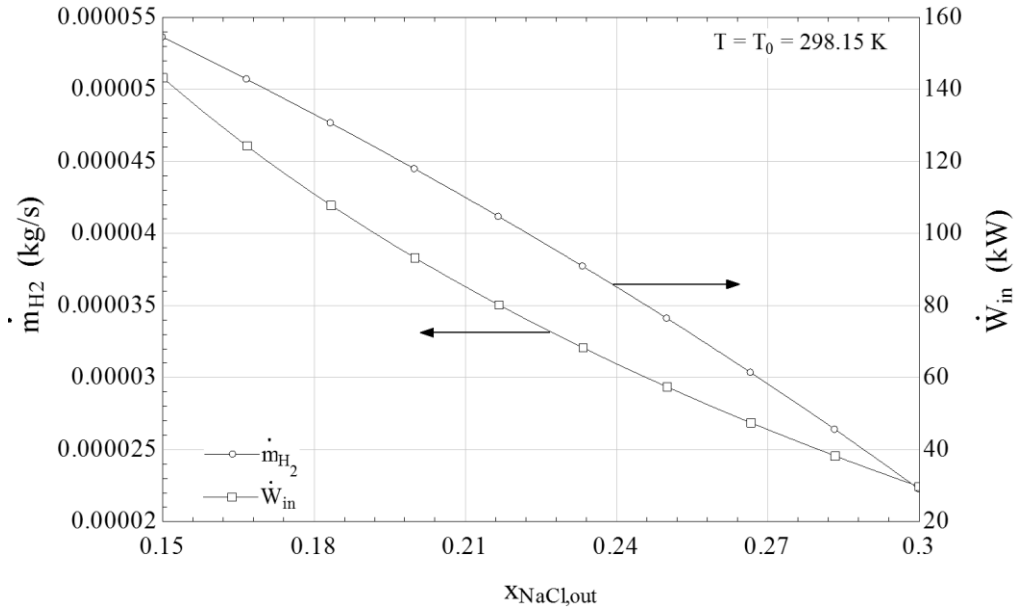


Figure 6.22: Effect of output brine concentration on hydrogen production rate and work input.

As explained previously, in accordance with the Faraday's law, decrease in the hydrogen production rate will decrease the required current input. This will also result in the smaller voltage drop across the anolyte and catholyte solution. Therefore, the required work input will decrease as seen in Figure 6.22 and Figure 6.23 which shows that increasing the exit brine concentration decreases the required current and voltage input.

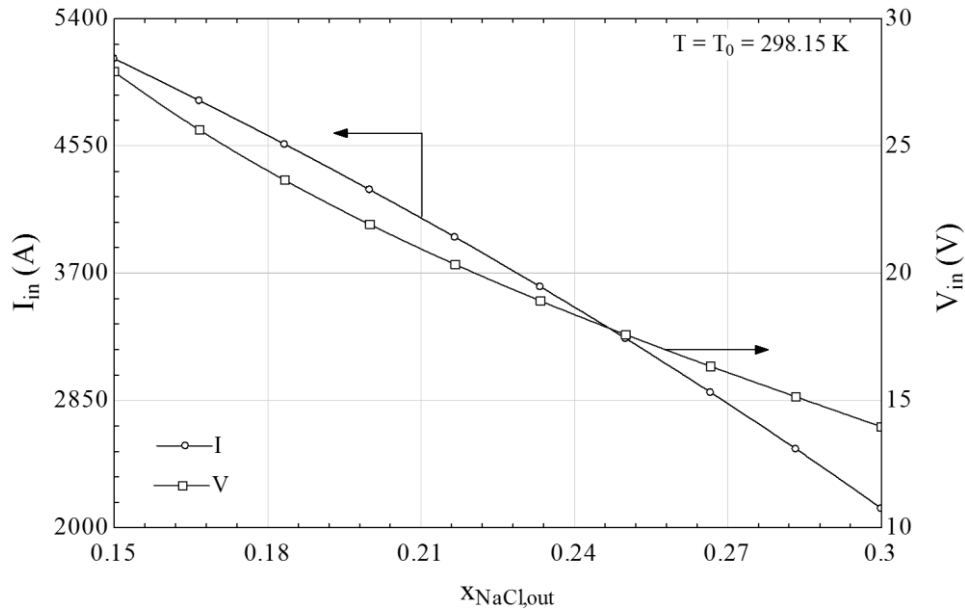


Figure 6.23: Effect of output brine concentration on input current and voltage.

Figure 6.25 shows that increasing the exit brine concentration decreases both the exergy destruction rate and exit sodium hydroxide concentration. As explained previously, with lesser

production yield, less OH^- ions are neutralised, hence the exit sodium hydroxide concentration decreases with increase in exit brine concentration.

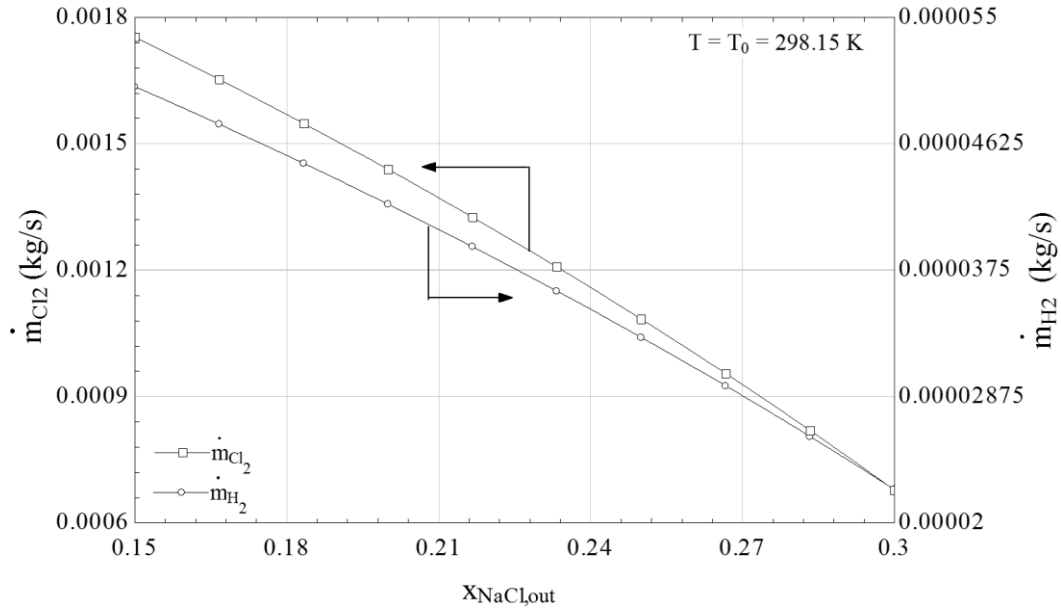


Figure 6.24: Effect of output brine concentration on production yield for chlorine and hydrogen gases.

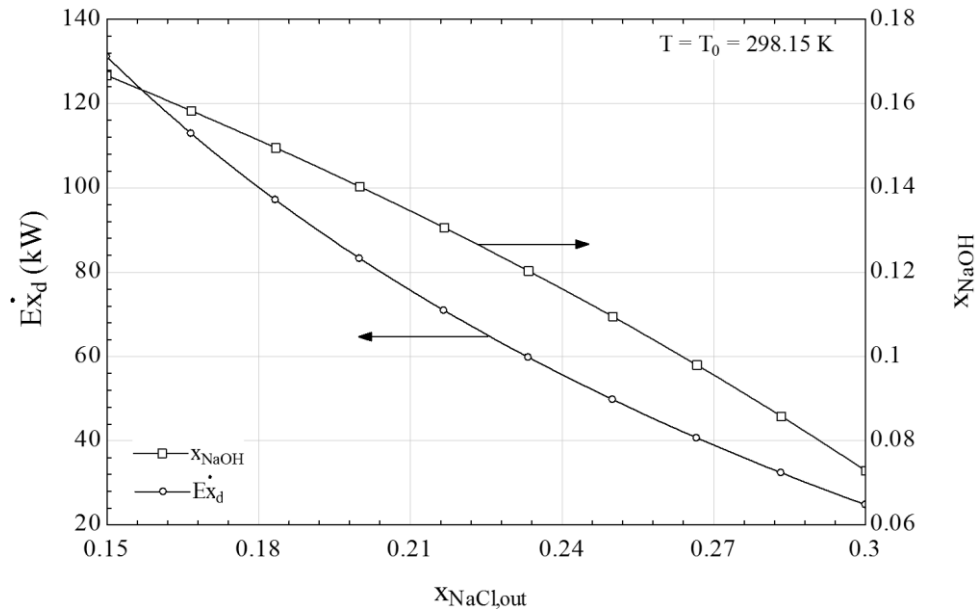


Figure 6.25: Effect of output brine concentration on exergy destruction rate and NaOH exit concentration.

6.2.6 Case Study 6

For the sixth case study, the distance (in m) from the anode to membrane and cathode to membrane is made equal and varied simultaneously. Note that the inlet mass flow rates for brine and water are kept constant at 0.01 kg/s. Also note that in this case the operating and ambient temperature are kept fixed at 25°C.

Figure 6.26 shows that increasing the anode/cathode to membrane distance decreases both the energy and exergy efficiency. The voltage drop across the anolyte and the catholyte solution are directly related to the distance of the anode to membrane. Increase in this distance increases the voltage losses which in turn increases the cell voltage. This is also confirmed in Figure 6.28 which shows increasing the anode/cathode to membrane distance has no effect on the rate of input current while increasing the cell voltage.

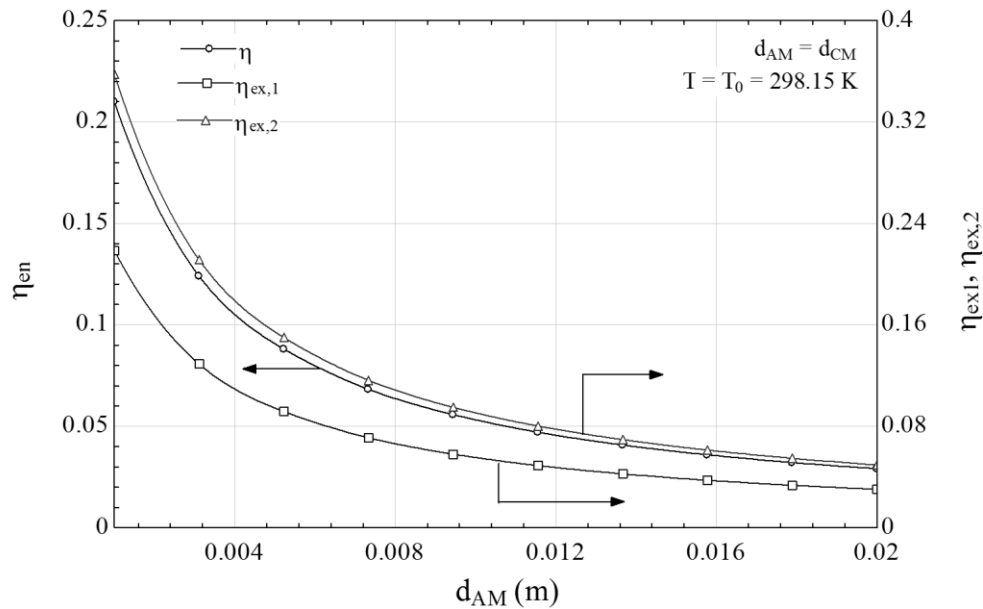


Figure 6.26: Effect of electrode membrane distance on energy and exergy efficiencies.

Figure 6.27 shows that increasing the anode/cathode to membrane distance has no effect on the rate of hydrogen and chlorine production as seen in Figure 6.29 while increasing the input work input. This is true because there is no change in the mass flow rate or the inlet or exit concentrations of the solutions. Hence there is no change in the production yield. However, due to the increase in the voltage losses with increase in the anode/cathode distance to membrane, the input work rate required is also increases.

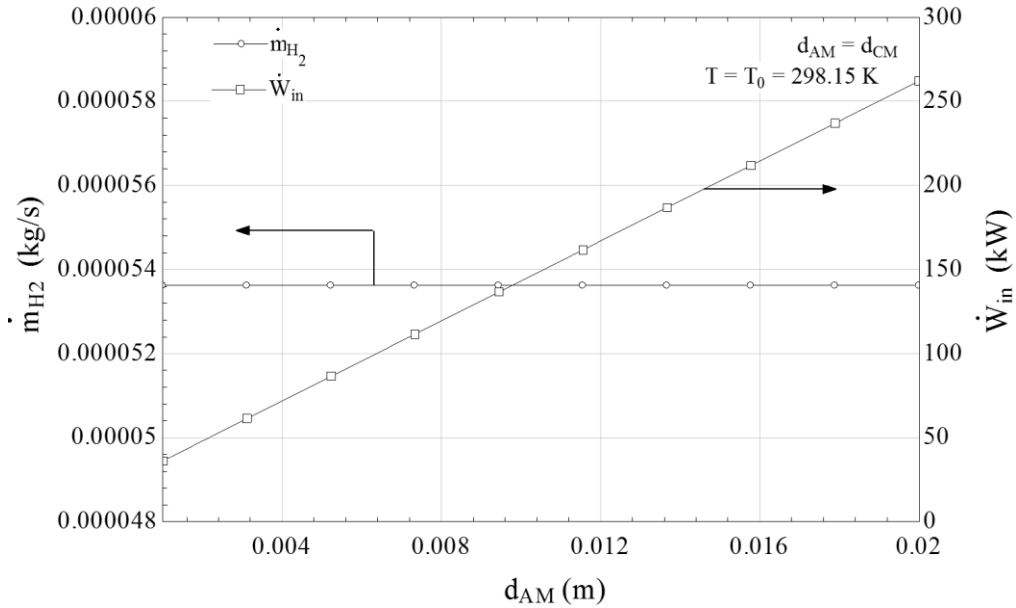


Figure 6.27: Effect of electrode membrane distance on hydrogen production rate and work input.

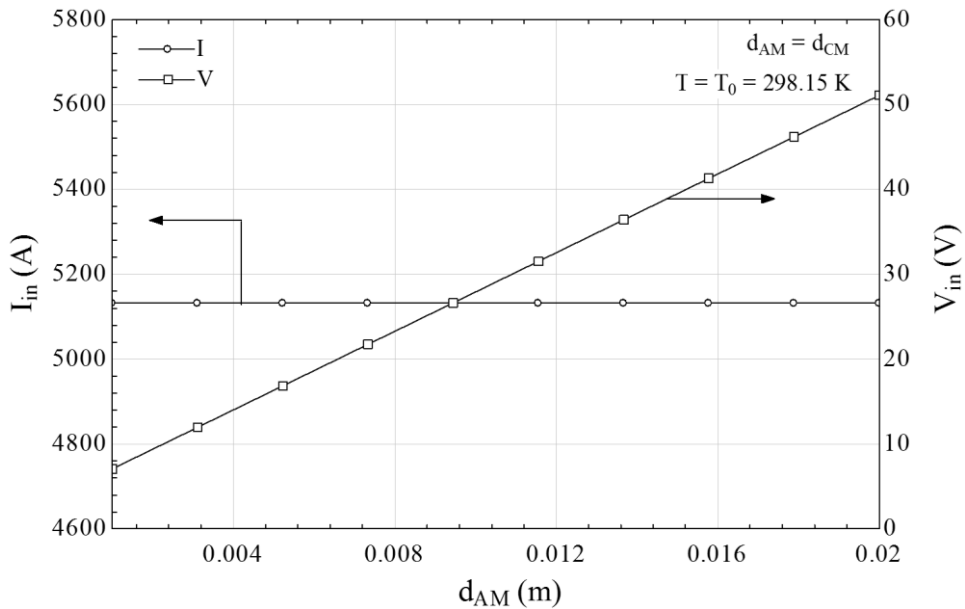


Figure 6.28: Effect of electrode distance on input current and voltage.

Figure 6.30 shows that increasing the anode/cathode to membrane distance has no effect on the exit sodium hydroxide concentration. This is obvious since as mentioned previously, there is no change in the mass flow rates or the concentrations of the solutions. Hence the exit concentration will be unaffected. However, the exergy destruction increases with increase in the distance because of the higher voltage losses and input work rate.

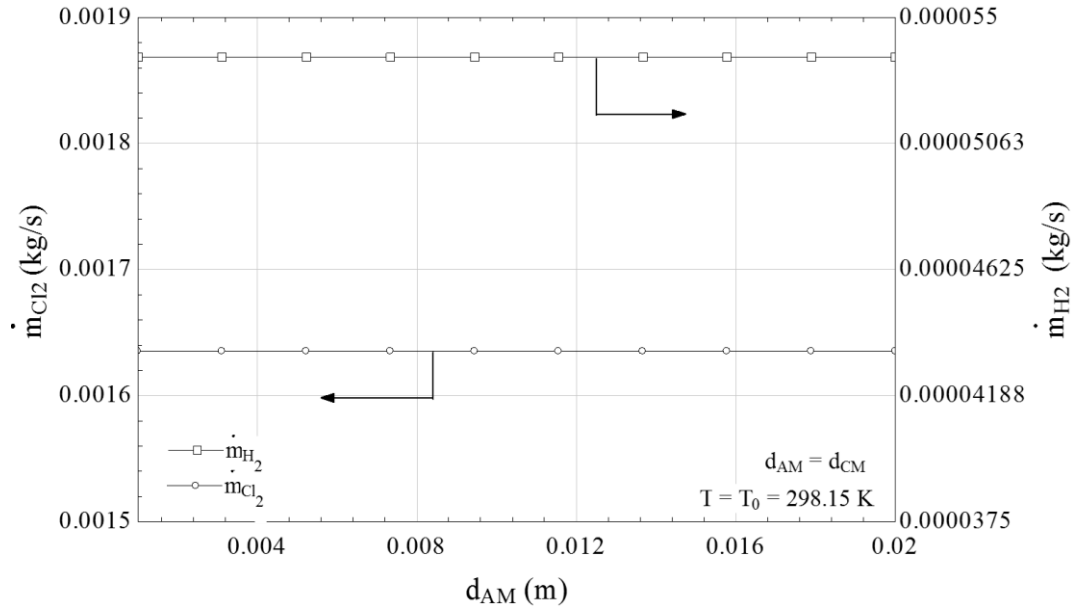


Figure 6.29: Effect of electrode membrane distance on production yield for chlorine and hydrogen gases.

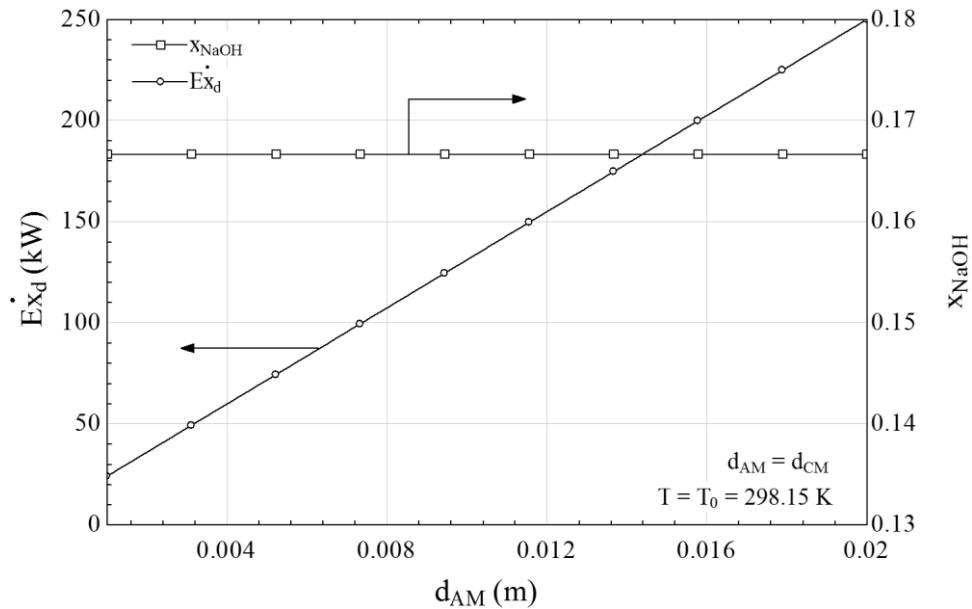


Figure 6.30: Effect of electrode membrane distance on exergy destruction rate and NaOH exit concentration.

6.3 Electrolysis Model

In this section, the PEC system is used just as an electrolyser. Detailed parametric studies are conducted to see the effect of ambient and operating parameters on efficiencies, potential losses, input work rate and exergy destruction rate for the PEC system. Figure 6.31 shows the increasing the reaction temperature increasing the energy and exergy efficiencies of the PEC electrolysis

model. It is important to note that the efficiencies for water electrolysis is much higher than that of when the reactor works as chloralkali configuration.

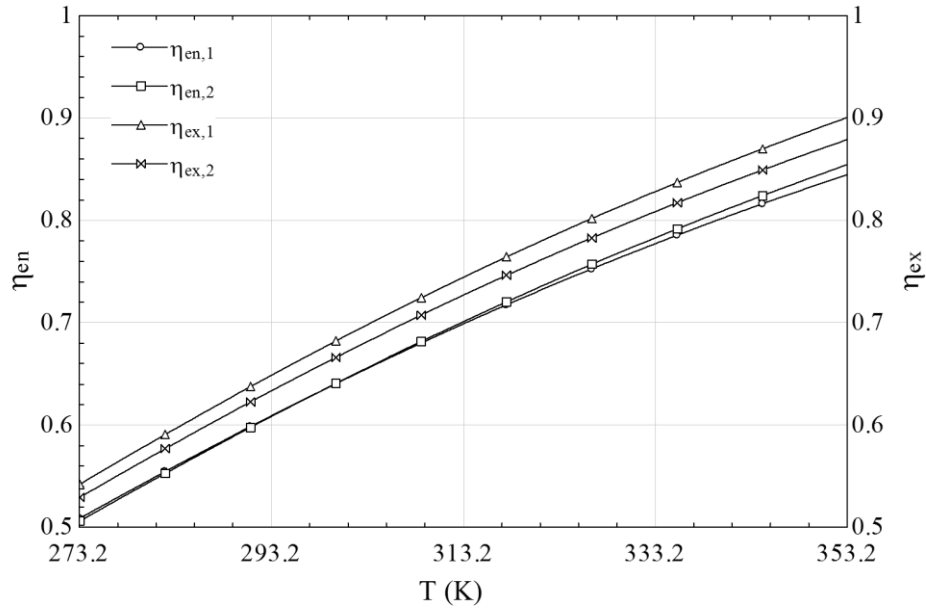


Figure 6.31: Effect of reaction temperature on energy and exergy efficiencies of water electrolyser.

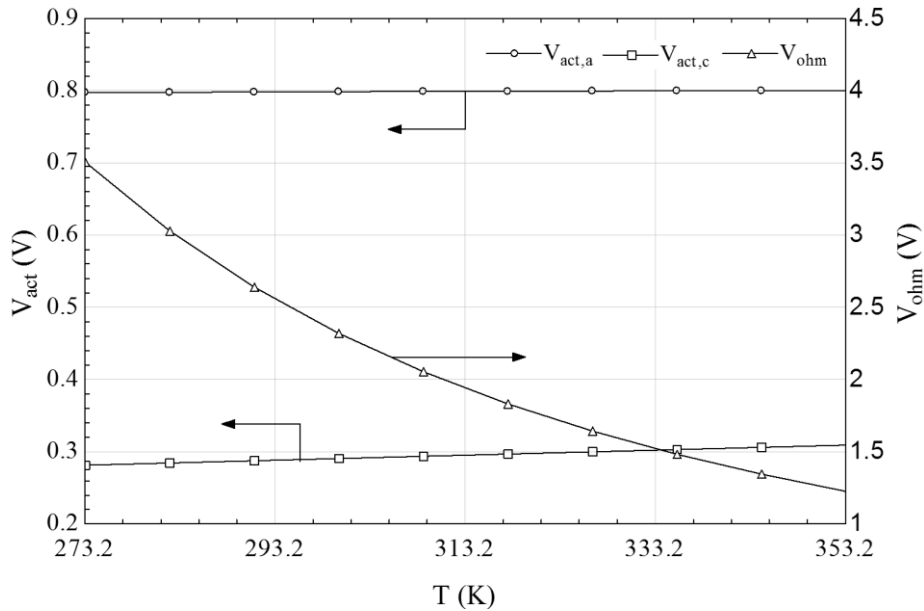


Figure 6.32: Effect of reaction temperature on activation and ohmic potentials.

As mentioned previously, with lower potential losses at higher temperatures, the input work rate also decreases, which in turn decreases the exergy destruction rate as confirmed in Figure 6.35 and hence the energy and exergy efficiencies increases. In general once can say that higher temperatures are preferable for higher efficiencies and lower losses.

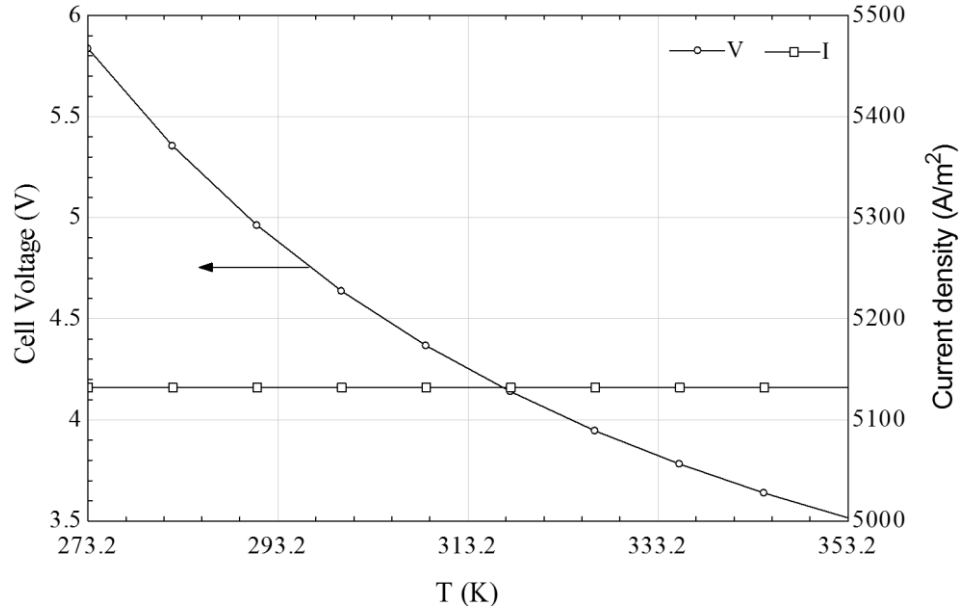


Figure 6.33: Effect on reaction temperature on cell voltage and current density.

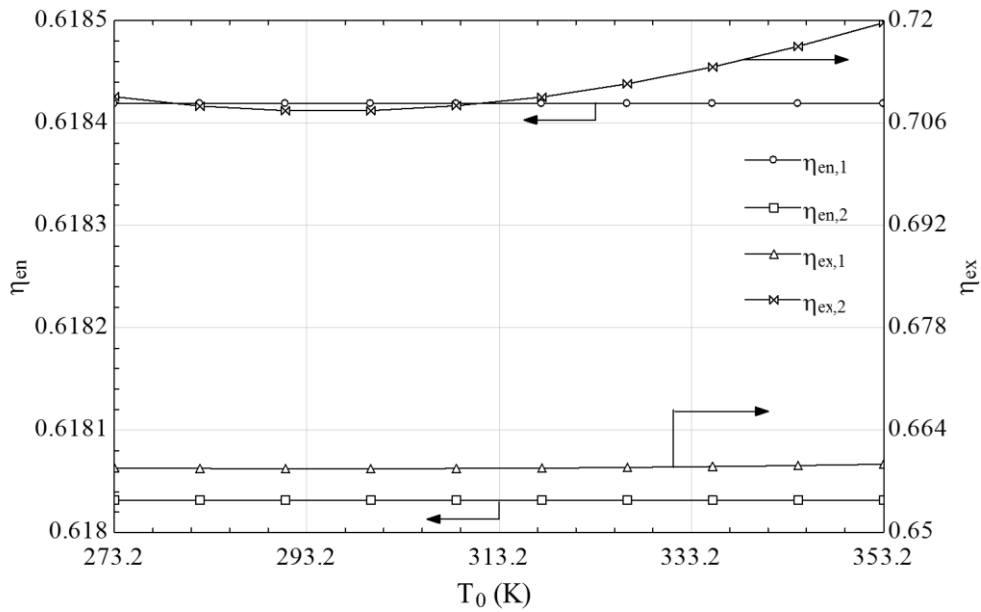


Figure 6.34: Effect of ambient temperature on energy and exergy efficiencies.

Figure 6.32 shows that increasing the reaction temperature has little effect on the activation potentials for anode and cathode. However, increasing the operating temperature decreases the ohmic losses. This results in the low cell voltage at higher operating temperatures as confirmed in Figure 6.33. The principal reason for this is that at higher temperatures, the conductivity of the membrane and the solution increases.

Figure 6.34 shows that the ambient temperature has no effect on the energy efficiencies. In contrast, increasing the ambient temperature increases the exergy efficiency for the PEC water electrolysis. Note that two energy and two exergy efficiencies are used just like in the chloralkali process. With more exergy content in the outputs makes the effect of the ambient temperature more prominent for $\eta_{ex,2}$ and less prominent for $\eta_{ex,1}$.

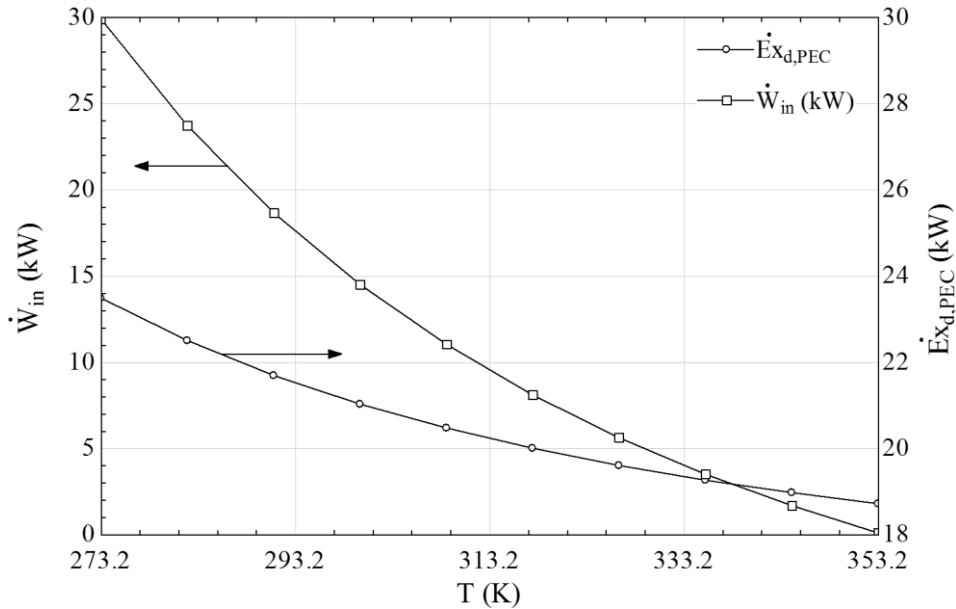


Figure 6.35: Effect of reaction temperature on input work and exergy destruction rates.

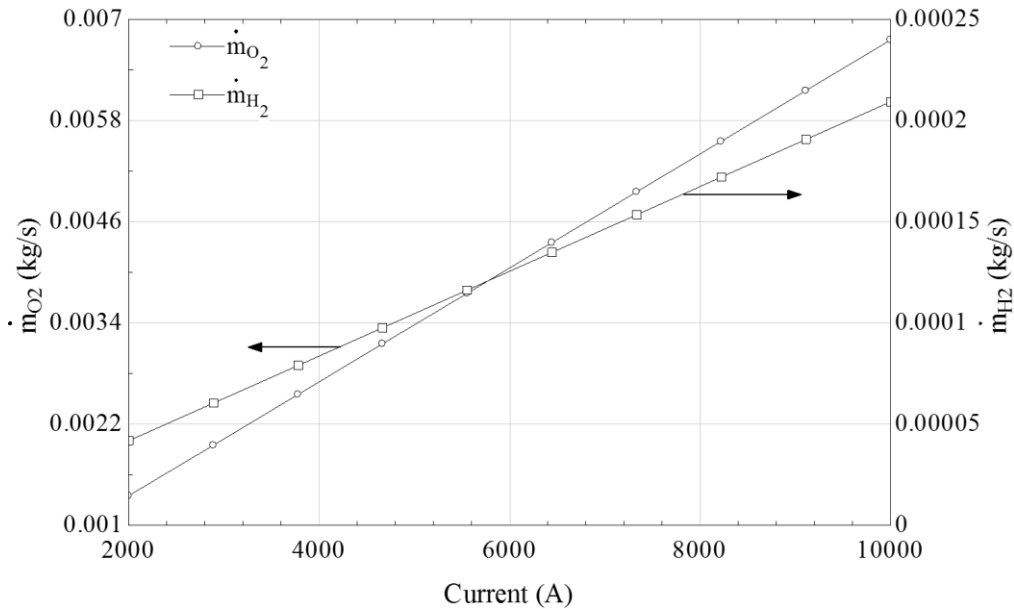


Figure 6.36: Effect of cell current on production yield rate of oxygen and hydrogen gases in water electrolysis.

Figure 6.36 shows that increasing the input increasing the hydrogen and oxygen production yield. As mentioned previously, the rate of hydrogen production is in direct accordance with the Faraday's law. Hence, with increase in input current, the rate of production of hydrogen and oxygen are bound to increase. However, with increase in current, the voltage losses are higher, which increases the required work input and in turn, increases the exergy destruction rate as confirmed by Figure 6.37.

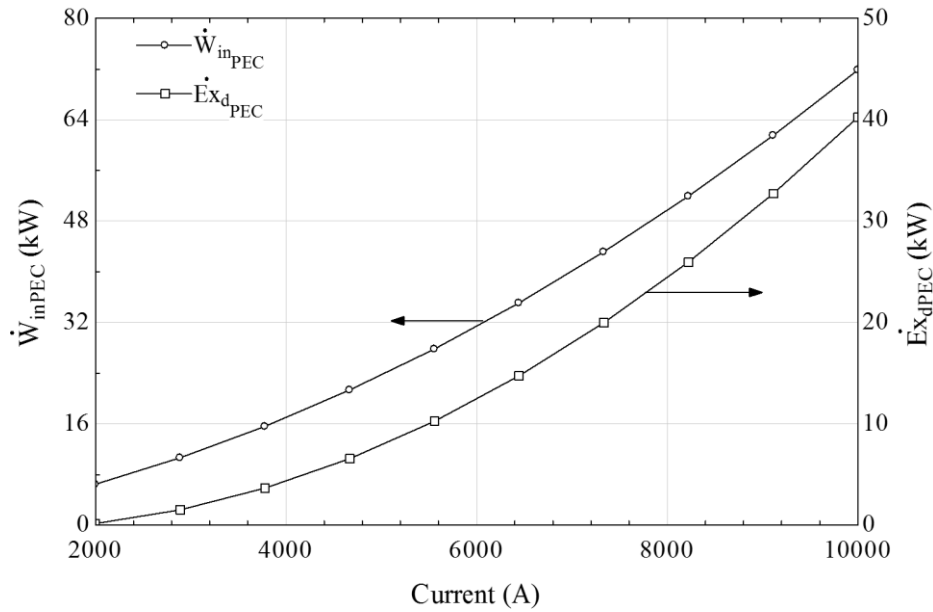


Figure 6.37: Effect of input current on input work rate and exergy destruction for the electrolyser.

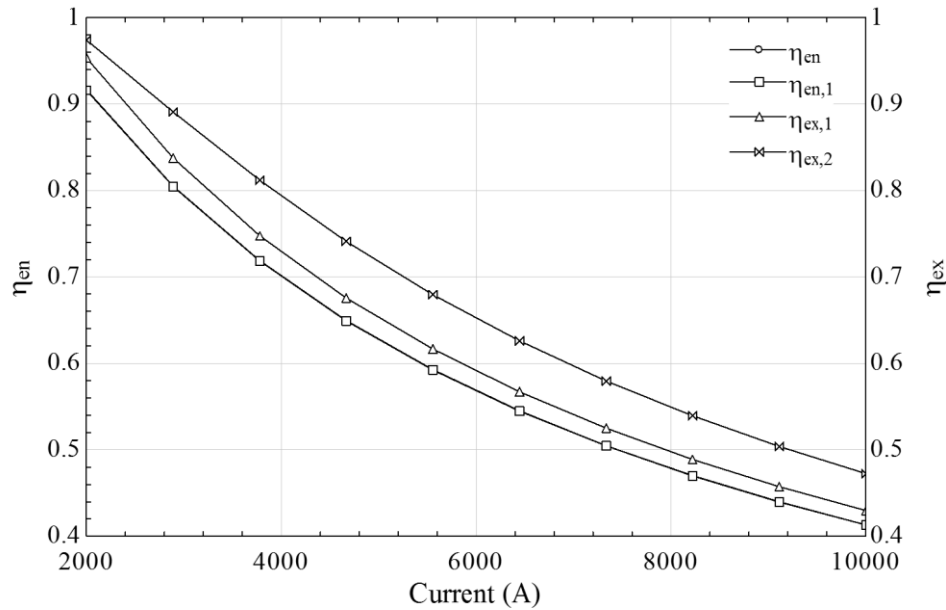


Figure 6.38: Effect of input current on energy and exergy efficiencies for the electrolyser.

Figure 6.38 shows that increasing the input current decreases the energy and exergy efficiencies for the electrolyser. As mentioned previously, increasing the current increases the input work rate and the exergy destruction rate. Hence, the efficiencies decrease.

6.4 Comparison of Model Results with Experimental Data

Figure 6.39 shows the comparison of the theoretical rate of production for hydrogen gas with the experimental model. Two graphs are presented for the experimental results; with light and without light. It is clear from the graph that for the same work input, the rate of hydrogen production is higher in presence of light. In other words, to produce the same amount of hydrogen, less work input is required when the cathode side of the reactor is illuminated to light. The difference in the work input is provided by light. The theoretical rate of hydrogen production is calculated by the Faraday's law. The experimental results in presence of light reaches approximately 87% of the Faraday production rate.

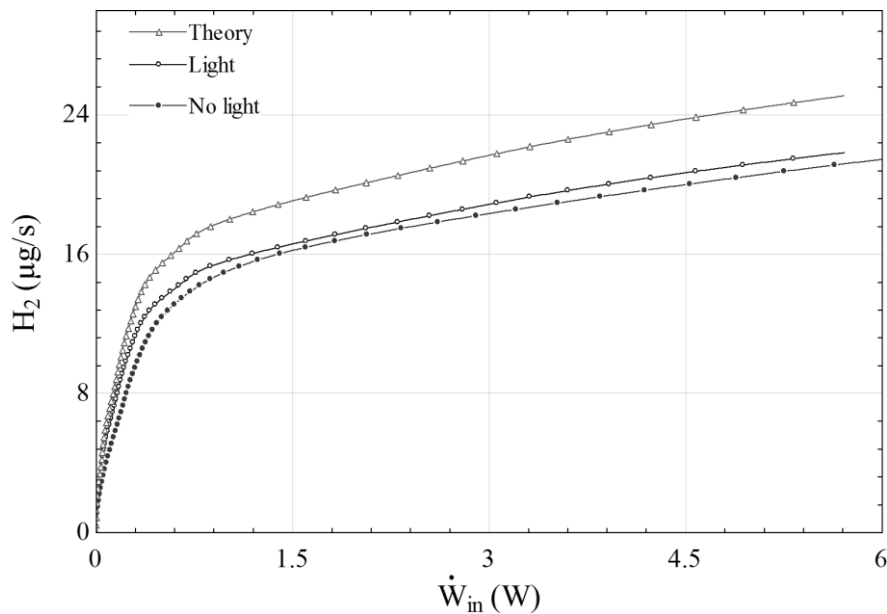


Figure 6.39: Comparison of hydrogen gas production rate.

Figure 6.40 shows the comparison of the I-V curve with the experimental model. Two graphs are presented for the experimental results; with light and without light. It is clear from the graph that as the current increases, the cell voltage increases sharply after which the voltage reaches saturation (approximately 1.8 V theoretically). However, the experimental results don't

reach saturation. This is because of the voltage losses are much higher and the current was only measured up to 2.8 A. The voltage graph is expected to reach saturation at higher input current.

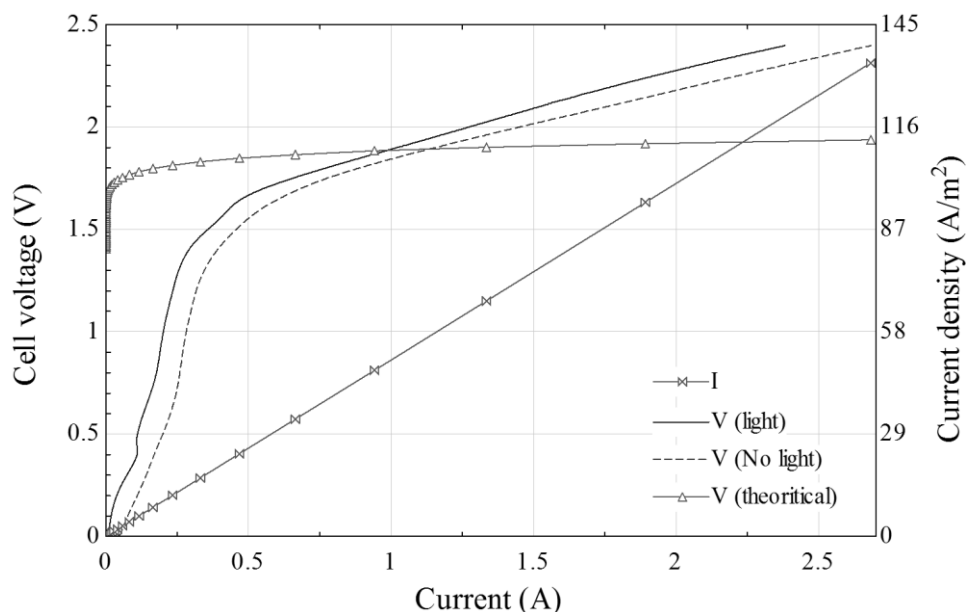


Figure 6.40: Comparison of IV curve for water electrolysis.

It is also important to note that even at an input current of 0 A, theoretically the voltage will be 1.23 V (equal to the open cell voltage). However, experimentally, at 0 A the cell voltage is 0 V. As the current increases and the cell activation potential is broken, the voltage then takes a sharp increase.

The theoretical rates of hydrogen and oxygen production can be found assuming that all the electric power goes to producing the gases by using the current density, area, and amount of time. These values were compared with the experimental data acquired at three different current densities. The figure shows that the efficiency of the electrolysis in the cell is constant at various current densities and is also the same for hydrogen and oxygen.

The current is less when light is being shined through the reactor. The change or saved current is shown on the right axis. The power input is compared with light and no light. The percentage of power used when light is present over when it is not present is shown in the right axis. Assuming the production rate is similar, the difference is the useful energy provided by the light for the reaction.

6.5 Scale-up Studies and Results

Finally the exergy destructions for the integrated hydrogen production system are determined and reported as shown in Figure 6.41. The total exergy destruction is 462.75 W per square metre of heliostat area. It is clear that the light processing system accounts for the maximum of the exergy destructions (40%), followed by the volumetric receiver (23%) while the desalination system, PV subsystem and the PEC account for equal amount of exergy destructions.

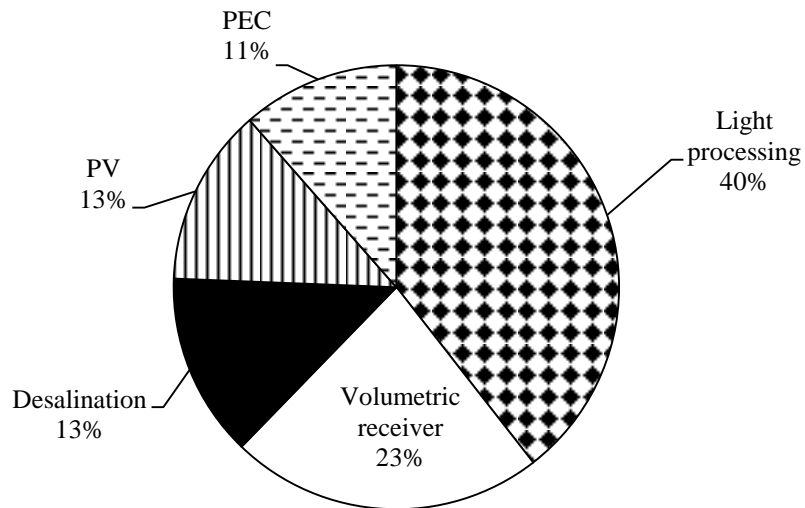


Figure 6.41: Exergy destructions of the integrated system in solar hydrogen production system.

The energy and exergy efficiencies for each subsystem are listed in Table 6.4. The comparison between these two are also done in Figure 6.41, respectively.

Table 6.4: Energy and exergy efficiencies of all subsystems in solar hydrogen production system.

<i>Subsystem</i>	<i>Exergy efficiency (%)</i>	<i>Energy efficiency (%)</i>
Heliostat field	64.93	64.98
Hot mirror spectral splitter	97.91	97.95
Upper/middle spectral splitter	93.42	93.71
Volumetric receiver	32.88	83
Photo-voltaic subsystem	25.95	25
Desalination subsystem	1.42	1.42

Table 6.5: Energy losses and exergy destruction values for all subsystems in solar hydrogen production system.

<i>Subsystem</i>	<i>Energy loss (W/m²)</i>	<i>Exergy destruction (W/m²)</i>
Heliostat field	175.1	166.7
Hot mirror spectral splitter	6.663	6.45
Upper/middle spectral splitter	9.446	9.558
Volumetric receiver	28.58	105.3
Photo-voltaic subsystem	62.92	59.85
Desalination subsystem	61.13	139.5

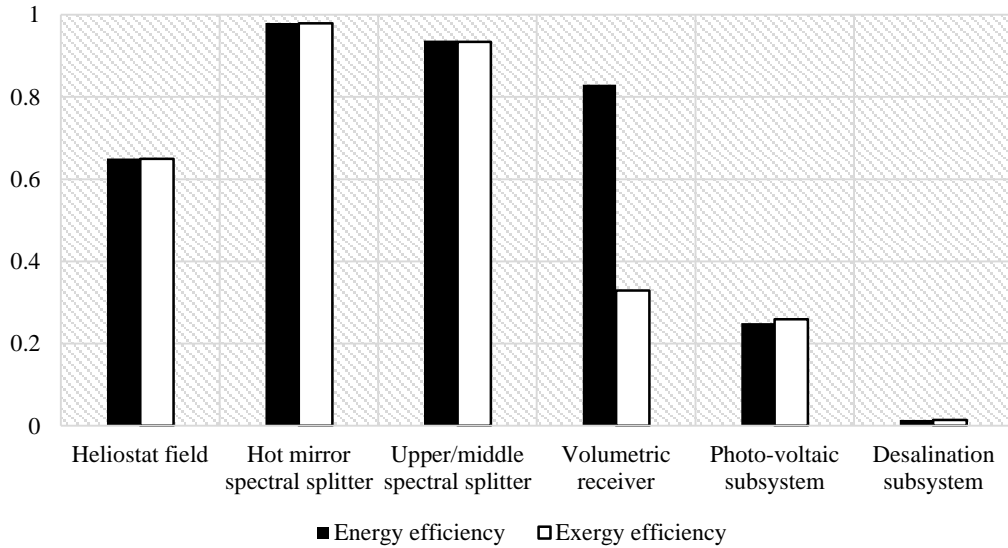


Figure 6.42: Energy and exergy efficiencies of all subsystems in solar hydrogen production system.

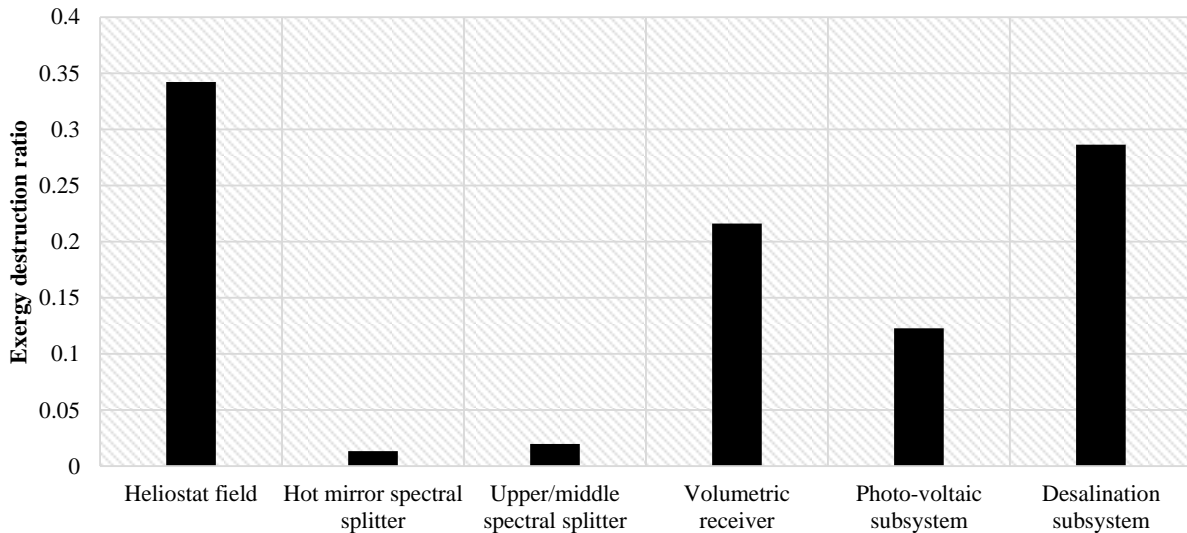


Figure 6.43: Exergy destruction ratios for all subsystems.

Correlations of seawater thermodynamic properties namely specific volume, specific enthalpy, specific entropy, chemical potentials, and osmotic pressure to be used in exergy analysis calculations are given. These correlations are provided by Sharqawy et al. (2011) which fit the data extracted from the seawater Gibbs energy function of IAPWS. They are polynomial equations given as functions of temperature and salinity at atmospheric pressure (or saturation pressure for temperatures over normal boiling temperature). For other correlations of seawater thermophysical properties, the equations recommended by Sharqawy et al. (2011) are used.

6.6 CFD Simulation Results

After applying the appropriate boundary conditions and defining the input and outputs of the system, the model is setup and simulated in ANSYS Fluent. Solutions and results including the contours of Pressure, velocity magnitude and temperatures are plotted. Figure 6.44 shows the vectors of velocity at all the points from the inlet to outlet for an inlet mass flow rate of 10 g/s of water. It is seen that the velocity is maximum of 1.07 m/s at the first exit while minimum at the bottom left corner and the top right corner of the reactor chamber. Although most of the flow makes a smooth transition from inlet to outlet, some of the flow comes back down to form a wake region at the left and right centre of the chamber.

The contours of velocity magnitude in m/s for different mass flow rates are shown in Figure 6.45a, Figure 6.45b, Figure 6.45c, and Figure 6.45d for 10 g/s, 25 g/s, 50 g/s, and 100 g/s, respectively. It is seen that for 10 g/s (low mass flow rate), the flow from the inlet 1 reaches about halfway into the chamber after which the flow separates. For the same flow rate, the flow from inlet 2 hardly manages to travel even a quarter of the chamber before separating. For the mass flow rate of 25 g/s (Figure 6.45b) the flow follows a similar pattern with the flow separating about halfway of the reactor chamber to create a low pressure (wake) region. When the flow rate is increased to 50 g/s (Figure 6.45c) it is seen that the flow from inlet 1 reaches much closer to the outlets and the flow separation occurs much later than that for lower flow rates. Finally for the maximum flow rate of 100 g/s (Figure 6.45d) it is seen that the flow from both outlets does not separate and a smooth transition from the two inlets to outlets takes place.

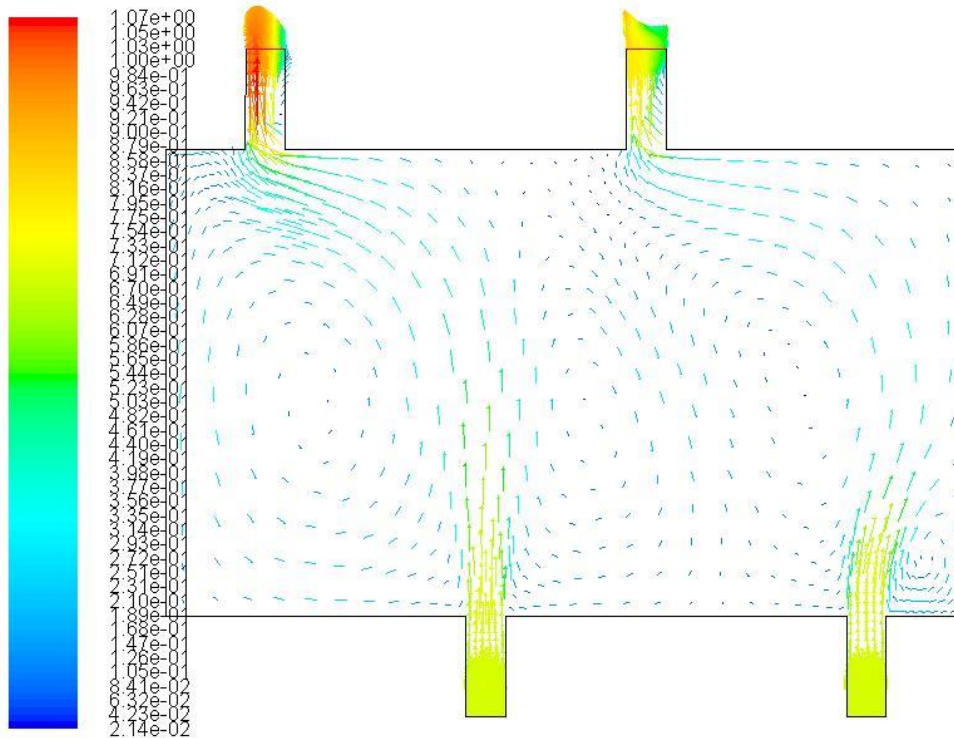


Figure 6.44: Velocity vectors coloured by velocity magnitude (m/s).

The visualisation of the velocity magnitude helps us to optimise the inlet mass flow rate and to determine which flow will brush the surface of the membrane the most that's present inside the reactor. The reason for the flow separation for a low mass flow rate is because of the lack of kinetic energy in the flow due to low velocity. A low mass flow rate directly affects the velocity of the flow which also affects the Reynolds number directly. A low Reynolds number in the pipe makes the flow laminar which means the fluid does not have enough kinetic energy to travel to the pressure exit and hence the flow separation occurs. From Figure 6.45 it is clear that for a high mass flow rate and high velocity gives the flow the extra kinetic energy to prevent the separation. This is seen for the 100 g/s flow where the Reynolds number is high making the flow turbulent to prevent the flow separation which in effect will brush through the surface of the membrane nicely compared to the other flow.

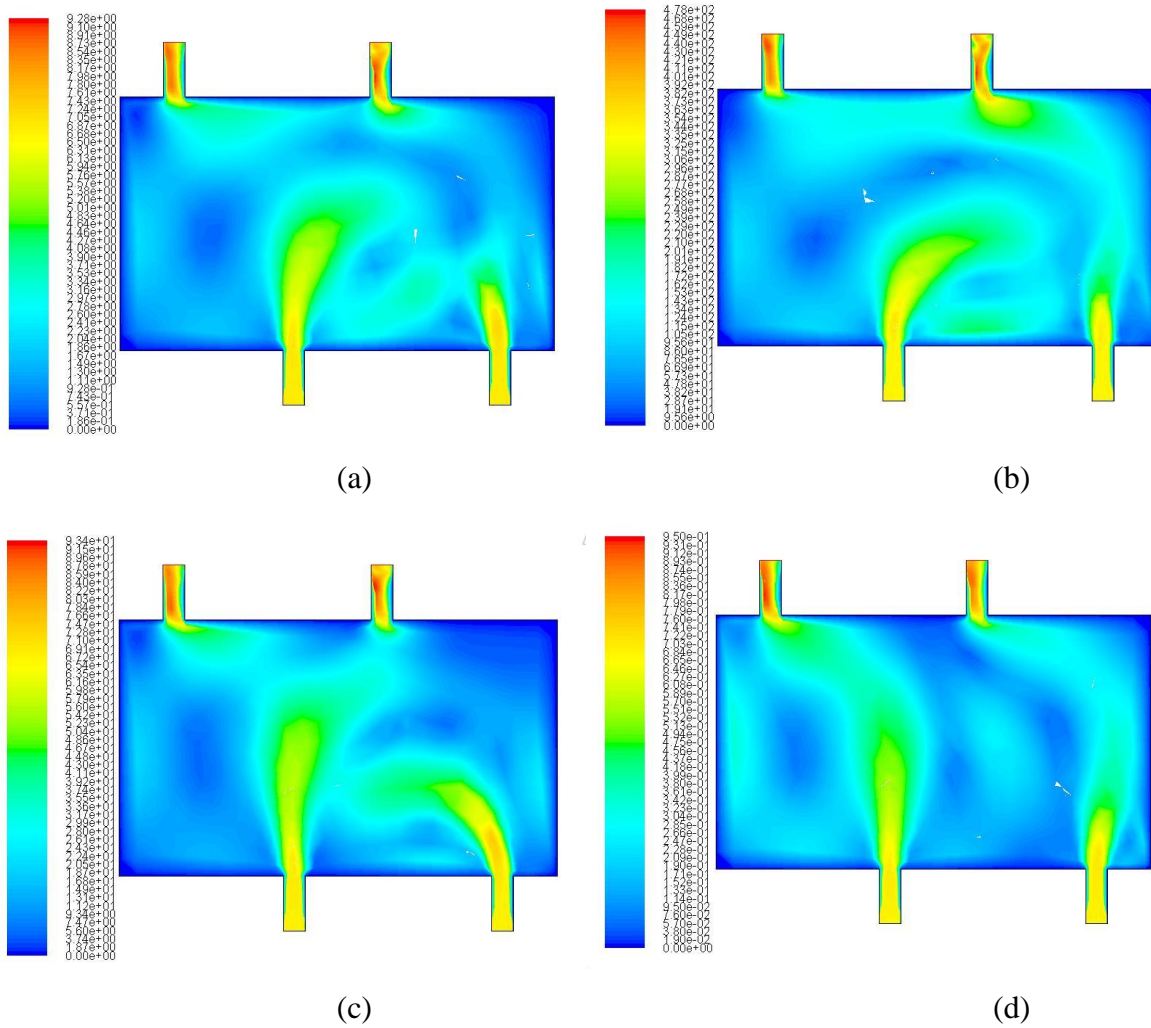


Figure 6.45: Velocity contours for (a) 10 g/s, (b) 25 g/s, (c) 50 g/s, (d) 100 g/s inlet mass flow rate

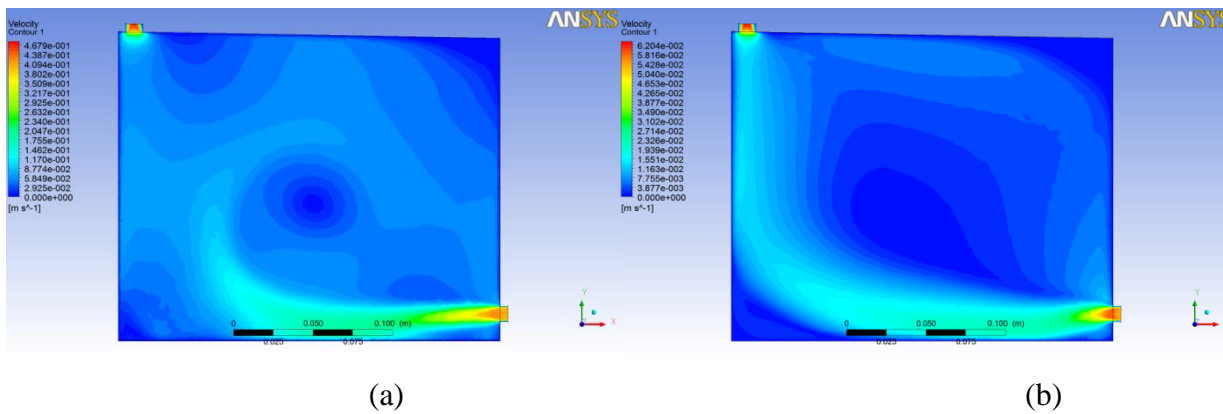


Figure 6.46: (a) One inlet and one outlet laminar flow, (b) one inlet and one outlet turbulent flow.

Figure 6.46a show the velocity contour coloured by velocity magnitude for the reactor that was previously designed. One can see why this design is not as effective as the one described in Figure 6.46b. With the previous design, it is realized that the flow does not brush the surface of the membrane smoothly and flows through the sides avoiding the surface area of the membrane. This directly affects the rate of the reaction and the efficiency of the system. This is why the modified design of the reactor will provide better results for water electrolysis.

6.7 Cost Assessment Results

In order to comparatively assess the system proposed herein, the cost analysis is performed according to the method described in the previous section. Table 6.7 shows the assumed parameters for the cost assessment. The annual production for the square metre of heliostat is of 2.8 kg of hydrogen, 47.59 kg of chlorine, 112 kg of caustic soda, and 50 kg of water. Assuming that the market price of products are \$1/kg for hydrogen, \$1/kg for chlorine, \$0.5/kg for caustic soda, and \$0.1/kg of water. Then the total income is \$61 with respect to 1 square metre of heliostat. In order to account for operation and maintenance (see OMCF in Table 6.7), we actually assumed that the levelised price of products is given as \$66 for square metre and year. In these conditions the capital productivity factor has been determined for three time spans, namely 10 years, 25 years, and 40 years. As shown in Figure 6.47, the investment is profitable for a specific invested capital (*SIC* in \$/m² of heliostat) of up to 400 \$/m² provided that the business time span is equal or superior to 25 years.

For 10 year time span the business becomes non-profitable if the specific invested capital is superior to \$290/m². More importantly, the selling price of hydrogen can be kept as low as \$1/kg because the revenue from the additional products makes the business favourable. This is really relevant in the context of producing sustainable hydrogen, because the product price becomes competitive with conventional technologies.

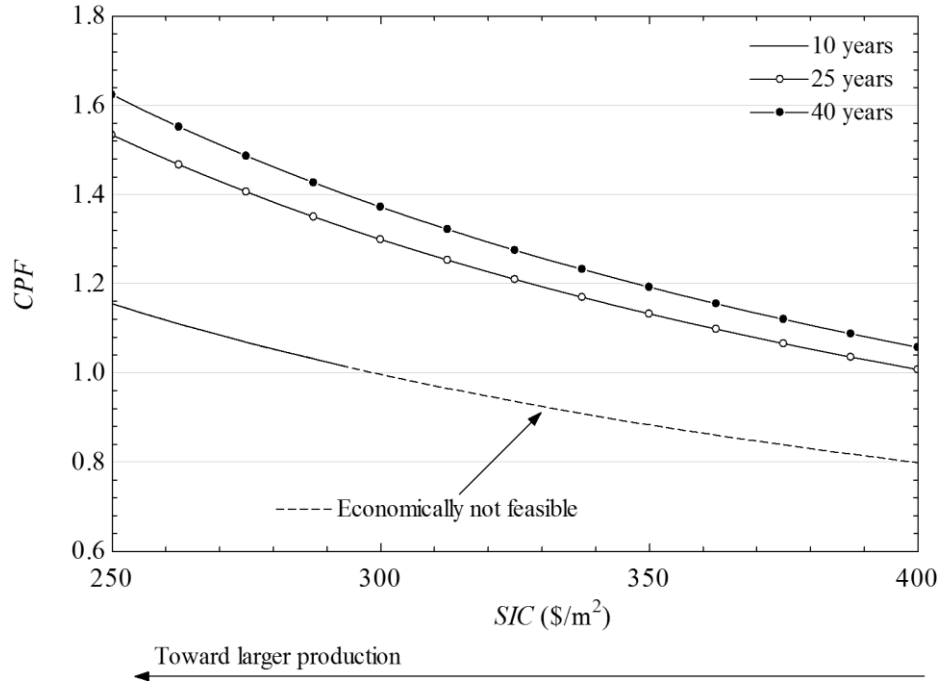


Figure 6.47: Capital productivity factor in function of the specific invested capital (\$/m² of heliostat field).

Table 6.6: Cost analysis equations.

Parameter	Equation
Market discount rate	$r_m = (r + 1)(i - 1) - 1$
Present value factor	$PVF = (1 + r)^{-N}$
Capital recovery factor	$CRF = \frac{r}{1 - (1 + r)^{-N}}$
Present worth factor	$PWF = CRF^{-1}$
Present worth income	$PWI = LPC AP PWF$
Net income	$NI = PWI (1 - OMCF)$
Tax credit deduction	$TCD = t_c IC$
Taxable income	$TI = NI - TCD$
Tax on income	$TOI = t_i TI$
Tax on property	$TOP = t_p C (1 - t_i)$
Salvage value	$SV = CSF C PVF (1 - t_s)$
Generated capital	$GC = NI + SV - IC - TOI - TOP$
Capital productivity factor	$CPF = (IC + GC)/IC$

Table 6.7: Assumed parameters for cost calculations.

Parameter	Symbol	Value
Real discount rate	r	0.1
Inflation rate	i	0.01
Tax on credit due to renewable energy	t_c	0.4
Tax on income	t_i	0.35
Tax on property	t_p	0.05
Tax on salvage	t_s	0.15
Capital salvage factor	CSF	0.2
Levelised product cost	LPC	66 \$/m ² .yr
Operation and maintenance cost factor	$OMCF$	0.1

The proposed system does not emit any harmful chemicals or GHG during operation. By converting potential waste into commercially viable products, the system not only eliminates emissions, but also increases the energy and exergy efficiencies and lowering production costs. As the Photoelectrochemical cell technologies evolve, the efficiency of the proposed system will only go higher and become more competitive to already mature technologies.

6.8 Optimisation Results

Two types of optimisation are calculated. In the first case, the objective function is to maximise the exergy efficiency of the PEC system. In the second case, the objective function is to maximise the energy efficiency of the PEC system.

6.8.1 Maximisation of Energy Efficiency

The optimised performance of the PEC system can be seen in Figure 6.48. The energy efficiency of the PEC system can ideally reach about 12%. It can be seen that the genetic algorithm solution converge towards 12% exergy efficiency after 1500 function calls.

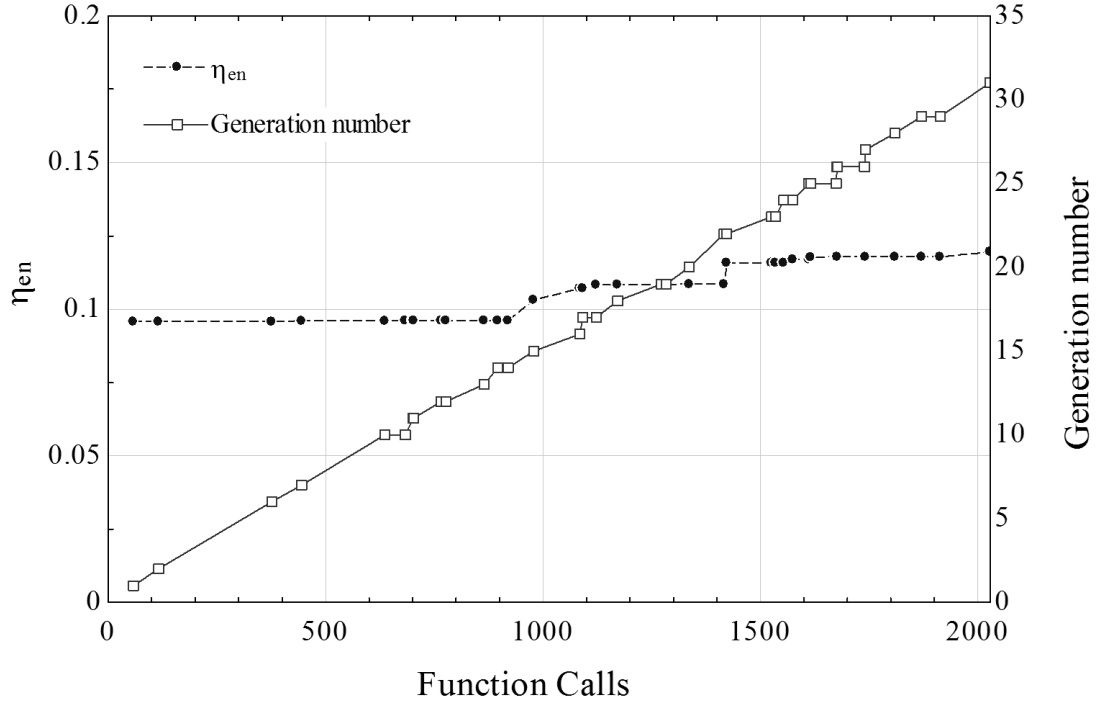


Figure 6.48: Maximisation of energy efficiency: genetic algorithm optimisation method (16692 iterations).

Table 6.8: Best values for the independent variables selected for genetic algorithm optimisation ($\eta_{en} = 11.96\%$).

<i>Independent variable</i>	<i>Best value</i>
Inlet brine \dot{m}_{in}	0.01 kg/s
Outlet brine \dot{m}_{out}	0.01 kg/s
Operation temperature, T	298.2 K
Ambient temperature, T_0	308.4 K
Outlet sodium hydroxide solution concentration $x_{s,2}$	0.322 kg/kg solution
Generation number	31

The best parameter values for the optimised PEC system can be seen in Table 6.8. From the best parameters, it is clear that the system will operation more efficiently energetically at operating temperature (298 K) and high ambient temperature (308.4 K). Low mass flow rates are also favourable for best efficiency results.

Table 6.9: State point parameters for maximum energy efficiency.

State	$\dot{m}(\text{kg/s})$	M_s (mol/L)	x_s (kg/kg solution)	h (kJ/kg)	s (kJ/kgK)	ex_{ch} (kJ/kg)	ex_{ph} (kJ/kg)
1	0.01	10.4	0.3779	-1221	9.429	84.57	179.1
2	0.009175	8.125	0.322	-3485	2.834	68.58	-38.01
3	0.0005035			21.89	3.214	1743	0.7935
4	0.01			-13337	10.74	49.96	3.058
5	0.01856	10.4	-1.19E+12	-5249	4.357	150.7	-48.68
6	0.0001604			650	66.85	147486	23.49

The mass flow rates (kg/s), molar concentration, concentration (kg/kg solution), specific enthalpy (kJ/kg), specific entropy (kJ/kgK), standard chemical exergy (kJ/kg), specific physical exergy (kJ/kg) for all state points for the optimised (maximum energy efficiency) PEC system are shown in Table 6.9.

Table 6.10: Performance parameters of the energy efficiency optimised system.

<i>Parameter</i>	<i>Value</i>
Hydrogen production rate, \dot{m}_{H_2}	0.00001604 kg/s
Current, I	15351 A
Operation temperature, T	298.15 K
Ambient temperature, T_0	308.4 K
Voltage, V	70.9 V
Work input, $\dot{W}_{in,PEC}$	1317 kW
Entropy generation, $\dot{S}_{gen,PEC}$	4.144 kW/K
Exergy destruction, $\dot{E}x_{d,PEC}$	1287 kW

These parameters optimised along with their values are listed in Table 6.10. It can be seen that the maximum work input required is 1317 kW, the maximum entropy generation is 4.114 kW/K and maximum exergy destruction is 1287 kW.

6.8.2 Maximisation of Exergy Efficiency

The optimised performance of the PEC system can be seen in Figure 6.49. The exergy efficiency of the PEC system can ideally reach about 49%. It can be seen that the genetic algorithm solution converge towards 50% exergy efficiency after 1000 function calls.

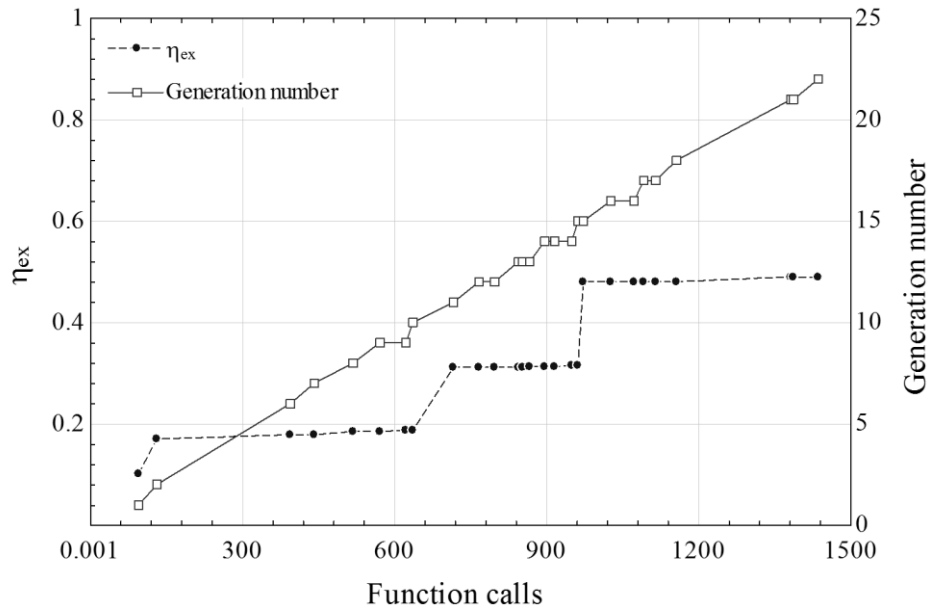


Figure 6.49: Maximisation of exergy efficiency: genetic algorithm optimisation method (4212 iterations).

The best parameter values for the optimised PEC system can be seen in Table 6.11. From the best parameters, it is clear that the system will operation more efficiently exergetically at high operating temperature (322 K) and low ambient temperature (273 K). Low mass flow rates are also favourable for best efficiency results.

The mass flow rates (kg/s), molar concentration, concentration (kg/kg solution), specific enthalpy (kJ/kg), specific entropy (kJ/kgK), standard chemical exergy (kJ/kg), specific physical exergy (kJ/kg) for all state points for the optimised (maximum exergy efficiency) PEC system are shown in Table 6.12.

Five parameters are optimised in this study within their respective ranges. These parameters along with their values are listed in Table 6.13. It can be seen that the maximum work input required is 244.3 kW, the maximum entropy generation is 0.73 kW/K and maximum exergy destruction is 226.8 kW.

Table 6.11: Best values for the independent variables selected for genetic algorithm optimisation ($\eta_{ex} = 49.01\%$).

<i>Independent variable</i>	<i>Best value</i>
Inlet brine \dot{m}_{in}	0.01 kg/s
Outlet brine \dot{m}_{out}	0.009465 kg/s
Operation temperature, T	273.5 K
Ambient temperature, T_0	322.1 K
Outlet sodium hydroxide solution concentration $x_{s,2}$	0.3249 kg/kg solution
Generation Number	22

Table 6.12: State point parameters for maximum exergy efficiency.

<i>State</i>	$\dot{m}(\text{kg/s})$	M_s (mol/L)	x_s (kg/kg solution)	h (kJ/kg)	s (kJ/kgK)	ex_{ch} (kJ/kg)	ex_{ph} (kJ/kg)
1	0.01	9.668	0.361	-2055	7.57	79.98	-72.44
2	0.009465	8.235	0.3249	-3398	2.923	69.53	20.14
3	0.0003265			-4.33	3.131	1743	0.321
4	0.01			-13439	10.42	49.96	1.251
5	0.01619	4.339	-1.70E+12	-4287	7.415	182.1	-33.6
6	0.00007043		0.361	-129.5	64.38	147486	9.596

Table 6.13: Performance parameters of the exergy efficiency optimised system.

<i>Parameter</i>	<i>Value</i>
Hydrogen production rate, \dot{m}_{H_2}	0.00007043 kg/s
Current, I	6741 A
Operation temperature, T	273.5 K
Ambient temperature, T_0	322.1 K
Voltage, V	36.24 V
Work input, $\dot{W}_{in,PEC}$	244.3 kW
Entropy generation, $\dot{S}_{gen,PEC}$	0.7341 kW/K
Exergy destruction, $\dot{E}x_{d,PEC}$	226.8 kW

The results of the two-objective optimisation are shown in Figure 6.50 which illustrates the Pareto frontiers. Observe that when the exergy efficiency is high, then the cell voltage must be low, therefore the investment cost in building the reactor is high. However, for such cases the revenues from the generated products are higher because more power is produced with a more efficient system. The exit concentration of sodium hydroxide cannot be reduced more than approx. 0.15 because it means that hardly any OH⁻ ions were neutralised and hardly any hydrogen gas was produced, which becomes unpractical.

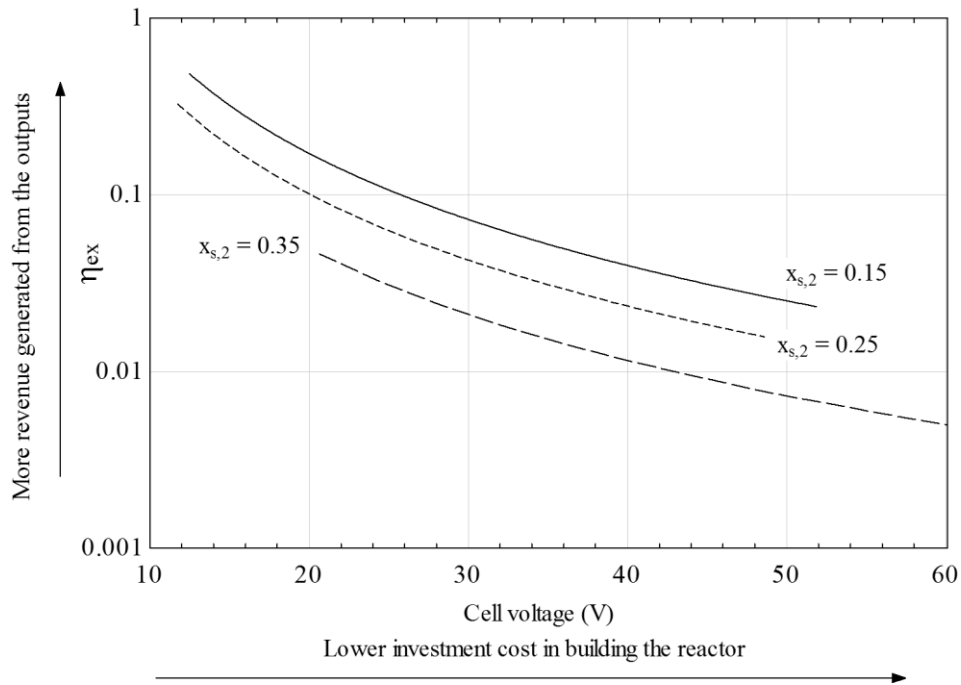


Figure 6.50: Pareto frontiers of two-objective optimisation for the PEC system when cost minimisation for building the reactor and revenue generated from the outputs are functions to be maximised.

Chapter 7: Conclusions and Recommendations

7.1 Conclusions

The proposed system modelling results show that the prototype under development reaches 150 g/h which is above the amounts obtained from the existing solar options. The present design is also suitable for scale up, which would increase the yield even further. It is applicable for residential purposes, on roof tops etc. The calculated solar-to-hydrogen efficiency is around 4%. With upcoming tests and verification, and MPEA electrodeposition methods, a novel hybrid hydrogen reactor can be developed suitable for residential and mid-scale purposes.

General-purpose CFD software is used as a framework for analysing the gas-liquid flow characteristics (pressure, gas and liquid velocities, gas and liquid volume fractions). The analysis is based on solving the coupled two-fluid conservation equations under typical and alternative operating conditions with appropriate boundary conditions, turbulence models and constitutive inter-phase correlations. It can be concluded that the most effective results were seen for 100 g/s mass flow rate in terms of smooth transition from inlet to outlet. Considering ideal reactions on the membrane it is imperative that the flow is fully turbulent in order to achieve high rate of reactions on the surface and higher hydrogen production and efficiency of the cycle.

Here are the main advantages for the new system, which can be denoted as “hybrid photoelectrochemical cell and balance of plant for hydrogen and multiple by-products generation (chlorine, sodium hydroxide, sulphur, fresh water)”:

- Using a polymeric membrane electrode assembly as photoelectrode (photocathode, photoanode or both).
- Possibility of enhancing the productivity by using particulate photocatalysts in addition to photoelectrodes.
- Three configurations are possible with the same cell: i) chloralkali, water splitting, hydrogen-sulphur.
- Integration with desalination.
- Original optics with light concentration and spectral splitting and integration with PV array.

The efficiency of the integrated system is calculated as 4% with annual production of 2.8 kg of hydrogen per square metre of heliostat. If the co-produced hydrogen, chlorine, caustic soda and fresh water are sold at 66 \$/m² for 25 years business timeframe, then the productivity of capital is 1.533, 1.299, 1.132 and 1.007 for equity investments of 250\$, \$300, \$350 and \$400 per metre square respectively which are plausible range for the integrated system capital cost. The total exergy destruction for the integrated system is calculated to be 462.75 W per square metre of heliostat area with the light processing system accounting for the highest (40%) and the PEC accounting for the lowest (11%) of the exergy destructions.

The advantages of the proposed system compared to other selected hydrogen production systems are the promisingly low hydrogen production cost and zero GHG emissions during operation. The hybrid system has a potential to further lower production costs and increase energy and exergy efficiencies as photoelectrochemical cell technologies evolve. Another promising advantage of the proposed system is that the system eliminates any potential waste by converting them to commercially viable goods.

7.2 Recommendations

The proposed system in this study shows promising initial results in terms of direct solar – hydrogen conversion by minimising the use of potentially harmful chemicals and converting the by-products into commercially viable commodities. With the introduction of novel engineered coating materials to support photonic hydrogen generation and improvement of photocatalytic properties of existing materials, it is possible to make the system more efficient and environmentally benign. Advanced investigation techniques along with detailed modeling studies have a potential to present more insight to managing and improving system performance. In this regard, the following recommendations are submitted:

- Different photoactive materials should be coated on MPEA to enhance PEC activity.
- Scale up studies should be conducted experimentally for large scale applications.
- Pressure effect on system performance should be investigated to see if it is feasible to operate above/below P_{atm} .
- The operation above ambient temperatures should be studied experimentally.

References

Abbasi, T. and Abbasi, S. A. (2011). "'Renewable' hydrogen: Prospects and challenges." Renewable and Sustainable Energy Reviews **15**(6): 3034-3040.

Acar, C. and Dincer, I. (2014). "Comparative assessment of hydrogen production methods from renewable and non-renewable sources." International Journal of Hydrogen Energy **39**(1): 1-12.

Acar, C., Dincer, I. and Zamfirescu, C. (2014). "A review on selected heterogeneous photocatalysts for hydrogen production." International Journal of Energy Research **38**(15): 1903-1920.

Almeida Filho, E., Vilar, E. and Feitoza, A. (2011). "Physical–chemical characterization and statistical modeling applied in a chlor-alkali diaphragm-cell process." Chemical Engineering Research and Design **89**(4): 491-498.

Andersson, M., Yuan, J. and Sundén, B. (2012). "SOFC modeling considering electrochemical reactions at the active three phase boundaries." International journal of heat and mass transfer **55**(4): 773-788.

ANSYS (2011). ANSYS FLUENT Theory Guide.

ASTM, G. (2013). 173-03 (2012) Standard tables for reference solar spectral irradiances: direct normal and hemispherical on 37 tilted surface.

Awad, A. H. and Veziroğlu, T. N. (1984). "Hydrogen versus synthetic fossil fuels." International Journal of Hydrogen Energy **9**(5): 355-366.

Bolton, J. R. (1978). "Solar Fuels." Science **202**(4369): 705-711.

Cesar, I., Kay, A., Gonzalez Martinez, J. A. and Grätzel, M. (2006). "Translucent Thin Film Fe₂O₃ Photoanodes for Efficient Water Splitting by Sunlight: Nanostructure-Directing Effect of Si-Doping." Journal of the American Chemical Society **128**(14): 4582-4583.

Chandran, R. R. and Chin, D. T. (1986). "Reactor analysis of a chlor—alkali membrane cell." Electrochimica Acta **31**(1): 39-50.

Chen, J., Genio, A. D. D., Carlson, B. E. and Bosilovich, M. G. (2008). "The Spatiotemporal Structure of Twentieth-Century Climate Variations in Observations and Reanalyses Part I: Long-Term Trend." Journal of Climate **21**(11): 2611-2617,2619-2621,2623-2629,2631-2633.

Chikhi, M., Rakib, M., Viers, P., Laborie, S., Hita, A. and Durand, G. (2002). "Current distribution in a chlor-alkali membrane cell: experimental study and modeling." Desalination **149**(1): 375-381.

Chlistunoff, J. (2005). Advanced chlor-alkali technology, Final Technical Report, LAUR 05-2444. Los Alamos, NM, USA.

Connolly, J. (2012). Photochemical Conversion and Storage of Solar Energy, Elsevier Science.

Dias, A. C. d. B. V. (2005). "Chlor-Alkali Membrane Cell Process."

Dincer, I. (2002). "Technical, environmental and exergetic aspects of hydrogen energy systems." International Journal of Hydrogen Energy **27**(3): 265-285.

Dincer, I. (2007). "Environmental and sustainability aspects of hydrogen and fuel cell systems." International Journal of Energy Research **31**(1): 29-55.

Dincer, I. (2012). "Green methods for hydrogen production." International Journal of Hydrogen Energy **37**(2): 1954-1971.

Dincer, I. and Rosen, M. A. (2012). Exergy: Energy, Environment and Sustainable Development, Elsevier Science.

Dincer, I. and Zamfirescu, C. (2014). Advanced Power Generation Systems, Elsevier Science.

Endoh, E., Otouma, H. and Morimoto, T. (1988). "Advanced low hydrogen overvoltage cathode for chlor-alkali electrolysis cells." International Journal of Hydrogen Energy **13**(4): 207-213.

Ewan, B. C. R. and Allen, R. W. K. (2005). "A figure of merit assessment of the routes to hydrogen." International Journal of Hydrogen Energy **30**(8): 809-819.

Ezzell, B. R., Carl, W. P. and Mod, W. A. (1984). Electrolytic cell having an improved ion exchange membrane and process for operating, US Patent 4242185A.

Fujishima, A. and Honda, K. (1972). "Electrochemical Photolysis of Water at a Semiconductor Electrode." Nature **238**(5358): 37-38.

Furuya, N. and Aikawa, H. (2000). "Comparative study of oxygen cathodes loaded with Ag and Pt catalysts in chlor-alkali membrane cells." Electrochimica Acta **45**(25-26): 4251-4256.

Georgiadou, M. (2003). "Modeling current density distribution in electrochemical systems." Electrochimica acta **48**(27): 4089-4095.

Ghosh, S. and Dincer, I. (2014). "Development and analysis of a new integrated solar-wind-geothermal energy system." Solar Energy **107**: 728-745.

Gibson, T. L. and Kelly, N. A. (2010). "Predicting efficiency of solar powered hydrogen generation using photovoltaic-electrolysis devices." International Journal of Hydrogen Energy **35**(3): 900-911.

Goldemberg, J. (2006). "The promise of clean energy." Energy Policy **34**(15): 2185-2190.

Gratzel, M. (2001). "Photoelectrochemical cells." Nature **414**(6861): 338-344.

Gupta, R. B. (2008). Hydrogen Fuel: Production, Transport, and Storage, Taylor & Francis.

Hamann, C. H., Hamnett, A. and Vielstich, W. (2007). "Electrochemistry. 2nd." Completely Revised and Updated Edition, New York.

IEA (2014). Key World Energy Statistics 2014, OECD Publishing.

Jalali, A. A., Mohammadi, F. and Ashrafizadeh, S. N. (2009). "Effects of process conditions on cell voltage, current efficiency and voltage balance of a chlor-alkali membrane cell." Desalination **237**(1-3): 126-139.

Joshi, A. S., Dincer, I. and Reddy, B. V. (2010). "Exergetic assessment of solar hydrogen production methods." International Journal of Hydrogen Energy **35**(10): 4901-4908.

Joshi, A. S., Dincer, I. and Reddy, B. V. (2011). "Solar hydrogen production: A comparative performance assessment." International Journal of Hydrogen Energy **36**(17): 11246-11257.

Kainthla, R. C., Khan, S. U. M. and Bockris, J. O. M. (1987). "The theory of electrode matching in photoelectrochemical cells for the production of hydrogen." International Journal of Hydrogen Energy **12**(6): 381-392.

Kato, T. (2009). "Present Status of Hydrogen Production by Electrolysis (Advances in CO₂-Free Hydrogen Production Technologies)." Journal of the Japan Institute of Energy **88**(5): 371-377.

Khaselev, O., Bansal, A. and Turner, J. A. (2001). "High-efficiency integrated multijunction photovoltaic/electrolysis systems for hydrogen production." International Journal of Hydrogen Energy **26**(2): 127-132.

Kocha, S. S., Montgomery, D., Peterson, M. W. and Turner, J. A. (1998). "Photoelectrochemical decomposition of water utilizing monolithic tandem cells." Solar Energy Materials and Solar Cells **52**(3-4): 389-397.

Kolb, G. J., Davenport, R., Gorman, D., Lumia, R., Thomas, R. and Donnelly, M. (2007). Heliostat cost reduction. ASME 2007 Energy Sustainability Conference, American Society of Mechanical Engineers.

Kotas, T. J. (1995). The exergy method of thermal plant analysis, Krieger Melbourne, FL.

Kreuter, W. and Hofmann, H. (1998). "Electrolysis: The important energy transformer in a world of sustainable energy." International Journal of Hydrogen Energy **23**(8): 661-666.

Kudo, A. (2007). "Photocatalysis and solar hydrogen production." Pure and Applied Chemistry **79**(11): 1917-1927.

Kurt, C. and Bittner, J. (2000). Sodium Hydroxide. Ullmann's Encyclopedia of Industrial Chemistry, Wiley-VCH Verlag GmbH & Co. KGaA.

Levin, D. B. and Chahine, R. (2010). "Challenges for renewable hydrogen production from biomass." International Journal of Hydrogen Energy **35**(10): 4962-4969.

Lewis, N. S. and Nocera, D. G. (2006). "Powering the planet: Chemical challenges in solar energy utilization." Proceedings of the National Academy of Sciences **103**(43): 15729-15735.

Licht, S., Wang, B., Mukerji, S., Soga, T., Umeno, M. and Tributsch, H. (2001). "Over 18% solar energy conversion to generation of hydrogen fuel; theory and experiment for efficient solar water splitting." International Journal of Hydrogen Energy **26**(7): 653-659.

Lima, P. R., Mirapalheta, A., Henrique dos Santos Andrade, M., Vilar, E. O. and Tonholo, J. (2010). "Energy loss in electrochemical diaphragm process of chlorine and alkali industry—A collateral effect of the undesirable generation of chlorate." Energy **35**(5): 2174-2178.

MacDonnell, F. (2008). Molecular Approaches to Photochemical Splitting of Water. Solar Hydrogen Generation. K. Rajeshwar, R. McConnell and S. Licht, Springer New York: 123-165.

MacMullin, R. B., Burney, H. S., Electrolysis, E. S. I., Division, E. E. and Meeting, E. S. (1999). Chlor-alkali and Chlorate Technology: R.B. MacMullin Memorial Symposium : Proceedings of the Symposium, Electrochemical Society.

Mandin, P., Wüthrich, R. and Roustan, H. (2009). "Electrochemical engineering modelling of the electrodes kinetic properties during two-phase sustainable electrolysis." Computer Aided Chemical Engineering **27**: 435-440.

McEvoy, A., Markvart, T., Castañer, L., Markvart, T. and Castaner, L. (2003). Practical handbook of photovoltaics: fundamentals and applications, Elsevier.

McRae, W. A. (1980). Process and apparatus for controlling impurities and pollution from membrane chlor-alkali cells, US Patent 4242185A.

Mulder, M. (1996). Basic Principles of Membrane Technology, Springer.

Muradov, N. Z. and Veziroğlu, T. N. (2005). "From hydrocarbon to hydrogen—carbon to hydrogen economy." International Journal of Hydrogen Energy **30**(3): 225-237.

Ni, M., Leung, M. K. H., Leung, D. Y. C. and Sumathy, K. (2007). "A review and recent developments in photocatalytic water-splitting using for hydrogen production." Renewable and Sustainable Energy Reviews **11**(3): 401-425.

Nowotny, J., Sorrell, C. C., Sheppard, L. R. and Bak, T. (2005). "Solar-hydrogen: Environmentally safe fuel for the future." International Journal of Hydrogen Energy **30**(5): 521-544.

O'Brien, T. F. (1986). Control of sulfates in membrane cell chlor-alkali process, US Patent 4586993A.

O'Brien, T. F., Bommaraju, T. V. and Hine, F. (2007). Handbook of Chlor-Alkali Technology: Volume I: Fundamentals, Volume II: Brine Treatment and Cell Operation, Volume III: Facility Design and Product Handling, Volume IV: Operations, Volume V: Corrosion, Environmental Issues, and Future Developments, Springer.

O'Hayre, R. P., Cha, S.-W., Colella, W. and Prinz, F. B. (2006). Fuel cell fundamentals, John Wiley and Sons.

Palik, E. D. (1998). Handbook of Optical Constants of Solids, Academic Press.

Park, J., Li, P. and Bae, J. (2012). "Analysis of chemical, electrochemical reactions and thermo-fluid flow in methane-feed internal reforming SOFCs: Part I—Modeling and effect of gas concentrations." International Journal of Hydrogen Energy **37**(10): 8512-8531.

Pushpavanam, S., Pushpavanam, M., Natarajan, S. R., Narasimham, K. C. and Chinnasamy, S. (1993). "High surface area nickel cathodes from electrocomposites." International Journal of Hydrogen Energy **18**(4): 277-281.

Rabbani, M., Dincer, I. and Naterer, G. F. (2014). "Electrochemical analysis of a photoelectrochemical chloralkali reactor." Chemical Engineering & Processing: Process Intensification **82**(Complete): 42-53.

Rutherford, J. and Ver, H. R. W. (1994). Purification of chlor-alkali membrane cell brine, EP Patent 0427972B1.

Sato, N. (2004). Chemical energy and exergy: an introduction to chemical thermodynamics for engineers, Elsevier.

Sato, S. and White, J. M. (1980). "Photodecomposition of water over Pt/TiO₂ catalysts." Chemical Physics Letters **72**(1): 83-86.

Schmittinger, P. (2008). Chlorine: Principles & Industrial Practice, John Wiley & Sons.

Scott, D. S. (2008). Smelling Land: The Hydrogen Defense Against Climate Catastrophe, QP Publication Services.

Sharqawy, M. H., Zubair, S. M. and Lienhard, J. H. (2011). "Second law analysis of reverse osmosis desalination plants: An alternative design using pressure retarded osmosis." Energy **36**(11): 6617-6626.

Sobrino, F. H., Monroy, C. R. and Pérez, J. L. H. (2010). "Critical analysis on hydrogen as an alternative to fossil fuels and biofuels for vehicles in Europe." Renewable and Sustainable Energy Reviews **14**(2): 772-780.

Southworth, G. R., Lindberg, S. E., Zhang, H. and Anscombe, F. R. (2004). "Fugitive mercury emissions from a chlor-alkali factory: sources and fluxes to the atmosphere." Atmospheric Environment **38**(4): 597-611.

Strathmann, H. (2004). Ion-Exchange Membrane Separation Processes, Elsevier Science.

Szargut, J., Morris, D. R. and Steward, F. R. (1987). "Exergy analysis of thermal, chemical, and metallurgical processes."

Szargut, J. and Styrylska, T. (1964). "Approximate evaluation of the exergy of fuels." Brennst. Wärme Kraft **16**(12): 589-596.

Taylor, P. B., Agrawal, A. and Joshi, S. S. (2013). "Evolution of electrochemical finishing processes through cross innovations and modeling." International Journal of Machine Tools and Manufacture **66**(Complete): 15-36.

Tarique, M. A. (2011). Experimental investigation of scroll based organic Rankine systems, University of Ontario Institute of Technology.

Ulleberg, Ø. (2003). "Modeling of advanced alkaline electrolyzers: a system simulation approach." International Journal of Hydrogen Energy **28**(1): 21-33.

Van de Krol, R. and Grätzel, M. (2011). Photoelectrochemical hydrogen production, Springer.

Vermeiren, P., Moreels, J. P., Claes, A. and Beckers, H. (2009). "Electrode diaphragm electrode assembly for alkaline water electrolyzers." International Journal of Hydrogen Energy **34**(23): 9305-9315.

Vijh, A., Belanger, G. and Jacques, R. (1992). Hydrogen energy progress IX. Proceedings of the Ninth World Hydrogen Energy Conference. Paris (France).

Vogel, W. and Kalb, H. (2010). Large-Scale Solar Thermal Power: Technologies, Costs and Development, Wiley.

Volgin, V. M. and Lyubimov, V. V. (2001). "Mathematical modelling of three-dimensional electrochemical forming of complicated surfaces." Journal of Materials Processing Technology **109**(3): 314-319.

WEC (2013). World Energy Resources: 2013 Survey. Survey of Energy Resources. London, World Energy Council: 468.

Yoshida, N., Yoshitake, M., Endoh, E. and Morimoto, T. (1989). "Development of highly durable low hydrogen overvoltage cathode in chlor-alkali cells." International Journal of Hydrogen Energy **14**(2): 137-140.

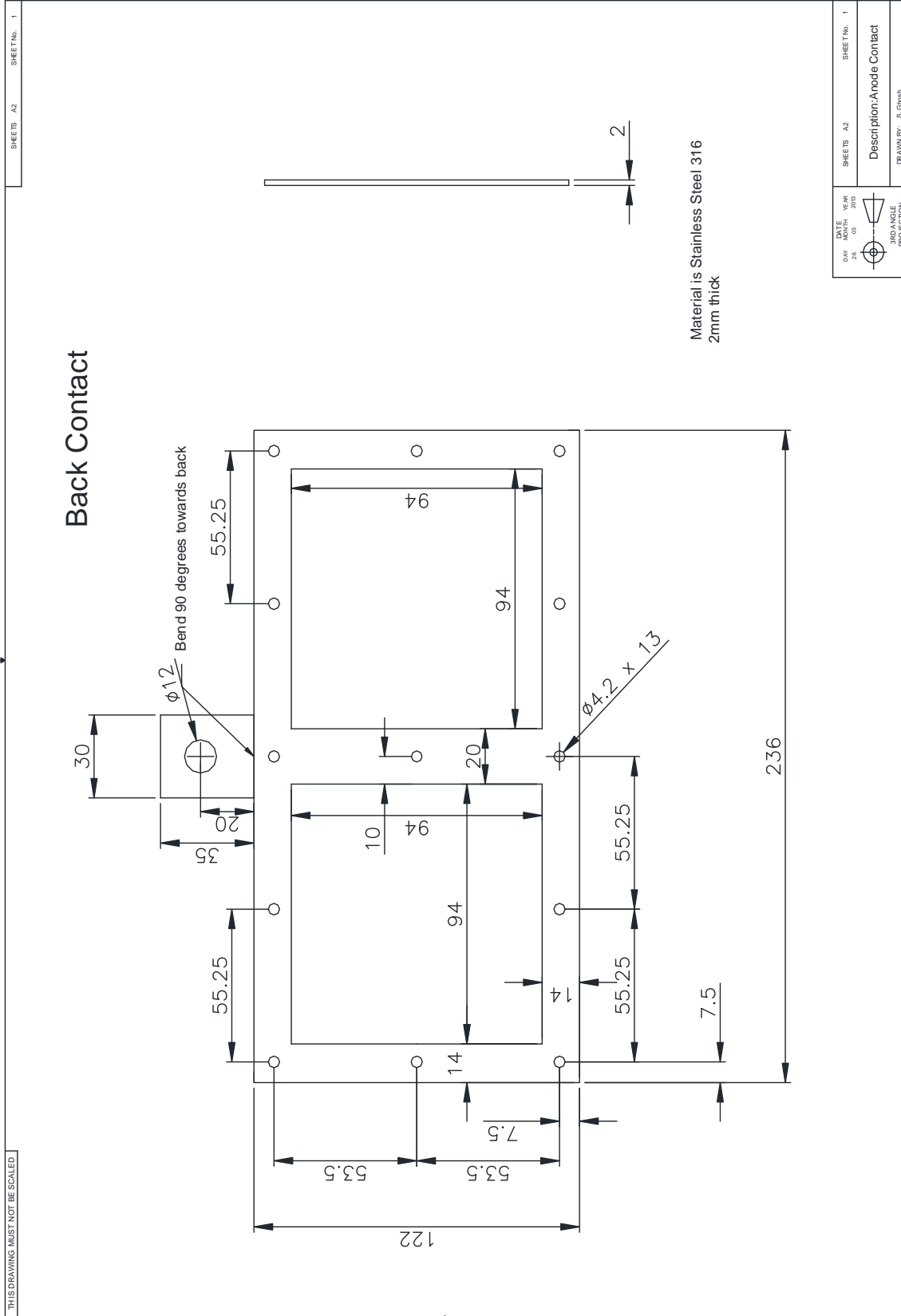
Zamfirescu, C. and Dincer, I. (2014). "Assessment of a new integrated solar energy system for hydrogen production." Solar Energy **107**: 700-713.

Zamfirescu, C., Dincer, I. and Naterer, G. F. (2011). "Analysis of a photochemical water splitting reactor with supramolecular catalysts and a proton exchange membrane." International Journal of Hydrogen Energy **36**(17): 11273-11281.

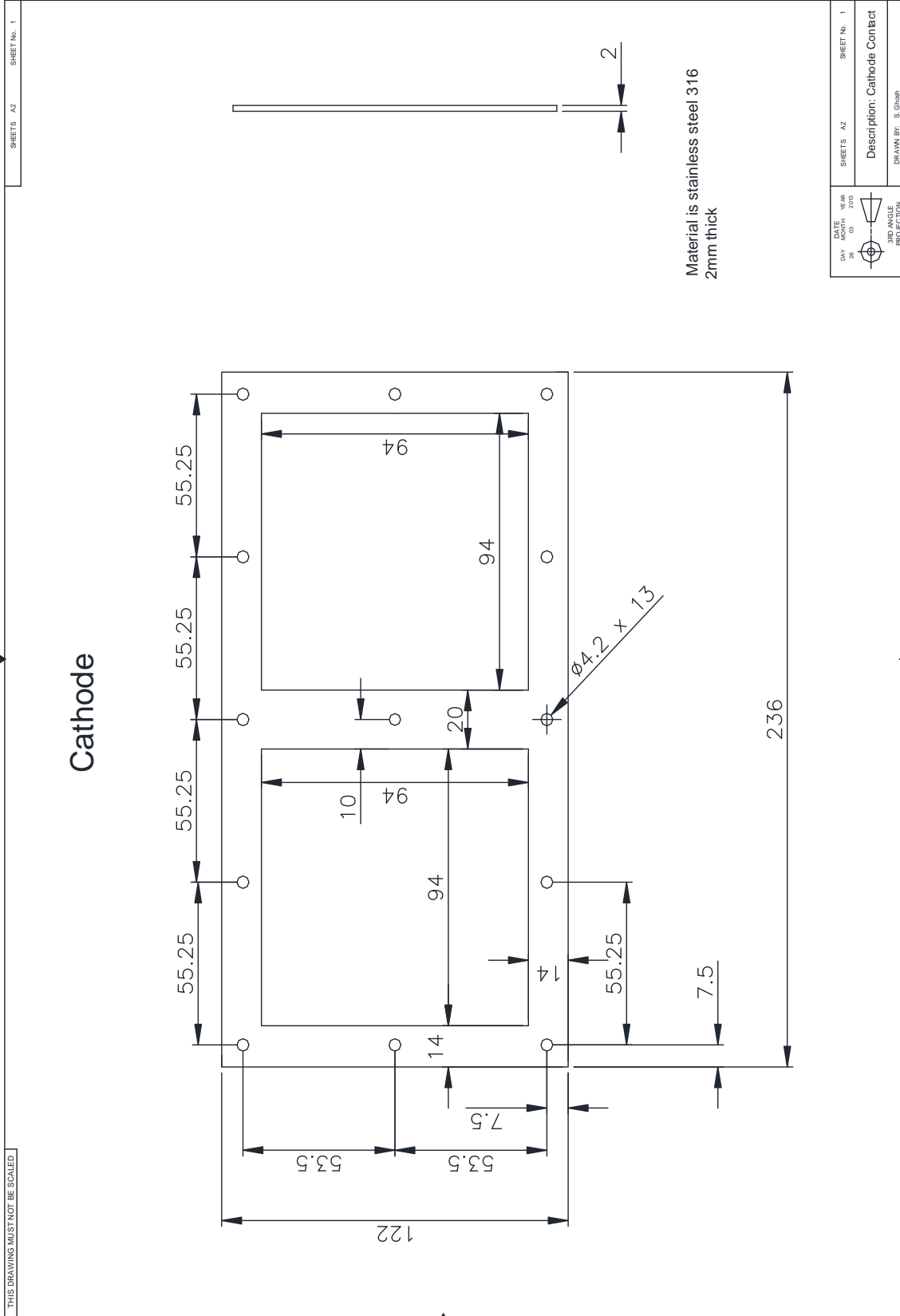
Zamfirescu, C., Dincer, I., Naterer, G. F. and Banica, R. (2013). "Quantum efficiency modeling and system scaling-up analysis of water splitting with Cd_{1-x}Zn_xS solid-solution photocatalyst." Chemical Engineering Science **97**(0): 235-255.

Zamfirescu, C., Naterer, G. F. and Dincer, I. (2008). Solar Light Based Hydrogen Production Systems. Encyclopedia of Energy Engineering and Technology, Taylor & Francis: 1-22.

A.2 Back Contact



A.3 Cathode Contact



A.4 Side Contact

